

Modelling of Ultrasonic Array Signals in Anisotropic Media

Anand, C.

DOI

[10.4233/uuid:afa3dcd6-1dc7-41c7-ab10-775c3f04222e](https://doi.org/10.4233/uuid:afa3dcd6-1dc7-41c7-ab10-775c3f04222e)

Publication date

2021

Document Version

Final published version

Citation (APA)

Anand, C. (2021). *Modelling of Ultrasonic Array Signals in Anisotropic Media*. [Dissertation (TU Delft), Delft University of Technology]. <https://doi.org/10.4233/uuid:afa3dcd6-1dc7-41c7-ab10-775c3f04222e>

Important note

To cite this publication, please use the final published version (if applicable).
Please check the document version above.

Copyright

Other than for strictly personal use, it is not permitted to download, forward or distribute the text or part of it, without the consent of the author(s) and/or copyright holder(s), unless the work is under an open content license such as Creative Commons.

Takedown policy

Please contact us and provide details if you believe this document breaches copyrights.
We will remove access to the work immediately and investigate your claim.

Propositions

Accompanying the dissertation

MODELLING OF ULTRASONIC ARRAY SIGNALS IN ANISOTROPIC MEDIA

By

Chirag Anand

1. A unitary system of symbols and terms should be established to encompass various fields of science.

[This proposition pertains to this dissertation]

2. Indiscriminate use of the term 'Green's function' has led to more confusion than assistance

[This proposition pertains to this dissertation]

3. Computational prowess has ruined the field of research in analytical and approximate solutions

[This proposition pertains to this dissertation]

4. Current lack of research on quantifying the quality of FMC images for composites is a boon for researchers

[This proposition pertains to this dissertation]

5. A PhD is not so much about intelligence as it is about perseverance

6. Primary driver of research should be inquisitiveness

7. The wheels of a welfare state run smoothly as long as the humanity of its cogs is preserved

8. It is unjustified to hold developing nations to the same standards of developed nations

9. The Covid pandemic brought to forth the advantages of an authoritarian government

10. A society should aspire to be an accepting society rather than a tolerant society

These propositions are regarded as opposable and defensible, and have been approved as such by the promoters Prof. dr. ir. R. Benedictus and Dr. R. M. Groves

Stellingen

behorende bij het proefschrift

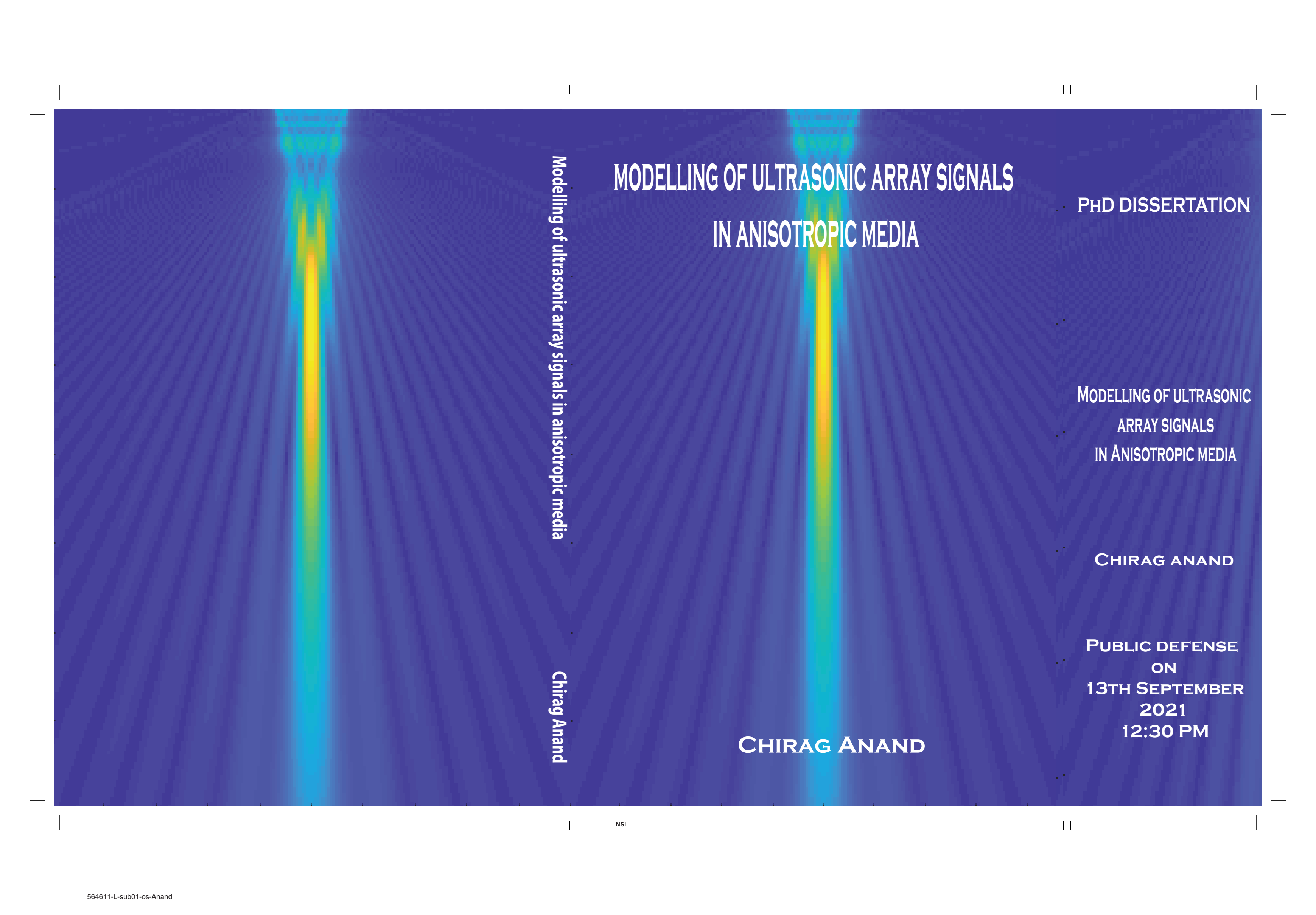
MODELLING OF ULTRASONIC ARRAY SIGNALS IN ANISOTROPIC MEDIA

door

Chirag Anand

1. Er zou een eenheidssysteem van symbolen en termen moeten worden opgericht om verschillende wetenschapsgebieden te omvatten.
[Deze stelling heeft betrekking op dit proefschrift.]
2. Onzorgvuldig gebruik van de term ‘greense functie’ heeft geleid tot meer verwarring dan hulp.
[Deze stelling heeft betrekking op dit proefschrift.]
3. Rekenkundige bekwaamheid heeft het onderzoeksgebied in de analytische en benaderende oplossingen geruïneerd.
[Deze stelling heeft betrekking op dit proefschrift.]
4. Het huidige gebrek aan onderzoek naar het kwantificeren van de kwaliteit van FMC-beelden voor composieten is een zegen voor onderzoekers.
[Deze stelling heeft betrekking op dit proefschrift.]
5. Een doctoraat gaat niet zozeer om intelligentie als wel over doorzettingsvermogen.
6. De belangrijkste drijfveer voor onderzoek zou nieuwsgierigheid moeten zijn.
7. De wielen van een verzorgingsstaat draaien soepel zolang de menselijkheid van zijn radertjes behouden blijft.
8. Het is ongerechtvaardigd om ontwikkelingslanden aan dezelfde normen te houden als ontwikkelde landen.
9. De coronapandemie bracht de voordelen van een autoritaire regering naar voren.
10. Een samenleving zou ernaar moeten streven om een accepterende samenleving te zijn in plaats van een tolerante samenleving.

Deze stellingen worden oponeerbaar enverdedigbaar geacht en zijn als zodanig goedgekeurd door de promotors Prof. dr. ir. R. Benedictus en Dr. R. M. Groves



**MODELLING OF ULTRASONIC ARRAY SIGNALS
IN ANISOTROPIC MEDIA**

PHD DISSERTATION

**MODELLING OF ULTRASONIC
ARRAY SIGNALS
IN ANISOTROPIC MEDIA**

CHIRAG ANAND

**PUBLIC DEFENSE
ON
13TH SEPTEMBER
2021
12:30 PM**

Modelling of ultrasonic array signals in anisotropic media

Chirag Anand

CHIRAG ANAND

Modelling of Ultrasonic Array Signals in Anisotropic Media

Dissertation

for the purpose of obtaining the degree of doctor
at Delft University of Technology
by the authority of the Rector Magnificus Prof.dr.ir. T.H.J.J. van der Hagen
chair of the Board for Doctorates
to be defended publicly on
Monday, 13th September 2021 at 12:30 hrs

by

Chirag ANAND

Master of Engineering in Aeronautical Engineering
Anna University, India
born in Mumbai, India

I

This dissertation has been approved by the promotor.

Composition of the doctoral committee:

Rector Magnificus,
Prof.dr.ir. R. Benedictus
Dr. R.M. Groves

Chairperson
Delft University of Technology, promotor
Delft University of Technology, promotor

Independent members:

Prof.dr. M. Snellen
Prof.dr. W. Osctachowicz
Prof.dr. A. Lhémy
Prof.dr. U. Staufer
Dr.ir. S. Shroff
Prof. C.A. Dransfeld

Delft University of Technology
IMP PAN, Poland
University of Paris-Saclay/ List CEA Tech
Delft University of Technology
Clean Sky Joint Undertaking
Delft University of Technology, reserve
member



Keywords:

Ultrasonic modelling, Gaussian beams,
CFRP, Full matrix capture, Total Focusing
method, Anisotropic, Stiffness matrix,
Phased array

Printed by:

Ipskamp printing (www.proefschriften.net)

Front cover:

Ultrasonic phased array beam through
austenitic steel

ISBN

978-94-6421-445-1

An electronic version of this dissertation is available at

<http://repository.tudelft.nl/>.

II

Dedicated to Dadaji, Dadima, Mom, Dad, Anurag, Laxmi and Vihaan

“If I have the belief that I can do it, I shall surely acquire the capacity to do it even if I may not have it at the beginning.”

Mahatma Gandhi

III

Summary

There has been a steady increase of composites and anisotropic materials in primary aircraft structures over the years. This increase is driven by the high strength to weight ratio of such materials leading to lighter and more efficient aircraft. As the uptake of such materials keeps increasing so does the complexity in geometry and manufacture of the parts which use these materials. As in the case of any structural component, these structures suffer from defects during manufacture and from damage inservice and have to be tested using non-destructive methods regularly.

A plethora of NDT techniques exist for testing aircraft structures with ultrasonic NDT being a staple in the industry. Testing using single element transducers is being replaced by phased arrays as phased arrays can be used in different testing configurations such as beam steering or using phased arrays to capture the signals and then post process the data to form an image. Phased array testing of isotropic materials has been carried out for a number of years with a lot of research being devoted to the testing of such materials. The testing of isotropic materials is relatively less complicated than for anisotropic materials due to the constant material properties throughout the material, the types of defects or failures which such structures suffer and the effect of the material properties on the ultrasonic beam propagating through it or on the output signals. This leads to a simpler interpretation and easier understanding of results when such structures are tested. On the other hand testing of anisotropic materials is complicated by the fact that the material properties are not the same in every direction. The anisotropic nature of such materials has an effect on the ultrasonic beam propagation and output signals which makes the interpretation and understanding of the output more difficult. The layered structure of the composite materials also leads to multiple reflections and reverberations of the layers during inspection which are properties of the laminate, array parameters etc. leading to noise in the output signals and noise in the image. Due to this ultrasonic NDT remains a bottleneck in the further implementation of composites in aircraft structures.

Understanding the effect of these various parameters experimentally would require dozens of experiments with different isolated parameters. To overcome the need for this enormous experimental campaign, modelling and simulations can be carried out to help understand these effects. There has been progress in the NDT community on the adoption of modelling methodologies to simulate the predict the response of the inspected material to the wave passing through it and the output signals which are generated. The numerical models

I

already developed have been applied to a variety of scenarios and to different complex geometries but become quite computationally expensive as the material and inspection procedure complexity increases and take hours of runtime when run on personal computers. Some analytical and semi-analytical models which have been applied are restricted either in geometry, require the numerical evaluation of multiple integrals, are computationally expensive or do not take into consideration the array parameters or are singular when interacting with different geometries.

The research presented in this thesis attempts provide a modelling methodology which is computationally inexpensive, does not require the evaluation of numerous integrals, takes the effects of the entire NDT setup into account and is accurate when compared to real-world inspection results. Two different scenarios are considered in this thesis. In the first scenario the ultrasonic beam from a phased array is used to inspect homogeneous anisotropic materials in which beam steering takes place. A model based on Gaussian beams is developed to simulate the steering, the effects that the material anisotropy and array parameters have on the beam propagating through the material. The model is validated against a numerical model for accuracy and a comparison of the models shows the developed model to be more computationally efficient.

In the second scenario, a model is developed to simulate the Full Matrix Capture (FMC) signals while inspecting a layered anisotropic material such as a Carbon Fibre Reinforce Plastic (CFRP) laminate. The model is developed based on multi Gaussian beams, stiffness matrix method and the angular spectrum of plane waves to simulate the received FMC signals from inspection of a CFRP laminate surrounded by a semi-infinite fluid medium. The simulated signals are compared with the experimentally obtained signals and show good agreement. Naturally the next step in the process would be the simulation of scattering from a defect embedded in the laminate. Side drilled holes (SDH) is the defect of choice due to its use as reference and calibration defects. The analytical scattering of the SDH is combined with the previously developed model by modifying the bounding medium to be a generally anisotropic solid. FMC signals for the scattering from a SDH are simulated and imaged using the Total focusing method taking the direction dependent velocity into account. The proposed model was then validated with the image generated from experimental FMC signals and is in good agreement qualitatively and quantitatively.

In conclusion the work in this thesis leads to two main results. The first is the development of a beam model for beam propagation from a phased array into an anisotropic material which leads to a better understanding of the influence of various material and array parameters and properties on the propagation of a beam through it. Second is the development of a model to simulate the full matrix capture

II

signals generated when inspecting layered anisotropic materials such as a CFRP laminate with or without a defect and the influence of the number of layers, layer thickness, manufacturing parameters and array parameters on the quality of the output signal and the image which is generated by post processing these signals.

Samenvatting

Er is in de loop der jaren een gestage toename geweest van composieten en anisotrope materialen in primaire vliegtuigconstructies. Deze toename wordt veroorzaakt door de hoge sterkte-gewichtsverhouding van dergelijke materialen, wat leidt tot lichtere en efficiëntere vliegtuigen. Naarmate de toepassing van dergelijke materialen blijft toenemen, neemt ook de complexiteit in geometrie en fabricage van de onderdelen die deze materialen gebruiken toe. Zoals bij elk structureel onderdeel, hebben deze constructies te maken met defecten tijdens de fabricage en schade tijdens het gebruik en moeten ze regelmatig worden getest met behulp van niet-destructieve methoden.

Er bestaat een overvloed aan NDT-technieken voor het testen van vliegtuigconstructies, waarbij ultrasone NDT in de industrie de voornaamste is. Testen met transducers met één element is vervangen door phased arrays, aangezien phased arrays kunnen worden gebruikt in verschillende testconfiguraties zoals bundelsturing of het gebruik van phased arrays om de signalen op te vangen en de gegevens vervolgens te verwerken tot een afbeelding. Het testen van isotrope materialen door middel van phased array wordt al een aantal jaren uitgevoerd en er wordt veel onderzoek gedaan naar het testen van dergelijke materialen. Het testen van isotrope materialen is relatief minder gecompliceerd dan het testen van anisotrope materialen vanwege de constante materiaaleigenschappen, de soorten defecten of het faalgedrag van dergelijke structuren en het effect van de materiaaleigenschappen op de ultrasone bundel die zich door het materiaal voortplant of op de uitgangssignalen. Dit leidt tot een eenvoudiger interpretatie en beter begrip van de resultaten wanneer dergelijke structuren worden getest. Aan de andere kant wordt het testen van anisotrope materialen bemoeilijkt door het feit dat de materiaaleigenschappen niet in alle richtingen hetzelfde zijn. De anisotrope aard van dergelijke materialen heeft een effect op de voortplanting van de ultrasone bundel en de uitgangssignalen, wat de interpretatie en het begrip ervan bemoeilijkt. De gelaagde structuur van de composietmaterialen leidt ook tot meerdere reflecties en weerkaatsingen van de lagen tijdens inspectie. Dit zijn eigenschappen van het laminaat en arrayparameters enzovoorts die leiden tot ruis in de uitgangssignalen en ruis in het beeld. Hierdoor blijft ultrasone NDT een bottleneck bij de verdere implementatie van composieten in vliegtuigconstructies.

Om het effect van deze verschillende parameters experimenteel te begrijpen, zou een groot aantal experimenten met verschillende afzonderlijke parameters nodig zijn. Om de noodzaak van deze enorme experimentele campagne te ondervangen, kunnen modelleringen en simulaties worden uitgevoerd om deze effecten beter te begrijpen. Er is vooruitgang geboekt in de NDT-gemeenschap met

V

het toepassen van modelleringsmethodologieën om de voorspelling van de respons van het geïnspecteerde materiaal op de golf die er doorheen gaat en de uitgangssignalen die worden gegenereerd, te simuleren. De reeds ontwikkelde numerieke modellen zijn toegepast op een verscheidenheid aan scenario's en op verschillende complexe geometrieën, maar worden behoorlijk rekenkundig intensief naarmate de complexiteit van het materiaal en de inspectieprocedures toeneemt. Hetgeen uren aan doorlooptijd kost wanneer ze op pc's worden uitgevoerd. Sommige analytische en semi-analytische modellen die zijn toegepast, zijn ofwel beperkt in geometrie, vereisen de numerieke evaluatie van meerdere integralen, zijn rekenkundig intensief of houden geen rekening met de arrayparameters of zijn singulier bij interactie met verschillende geometrieën.

Het onderzoek dat in dit proefschrift wordt gepresenteerd, biedt een modelleringsmethodologie die niet rekenkundig intensief is, geen evaluatie van talrijke integralen vereist, rekening houdt met de effecten van de gehele NDT-opstelling en nauwkeurig is in vergelijking met echte inspectieresultaten. In dit proefschrift worden twee verschillende scenario's beschouwd. In het eerste scenario wordt de ultrasone bundel van een phased array gebruikt om homogene anisotrope materialen te inspecteren waarin bundelsturing plaatsvindt. Er is een model ontwikkeld op basis van Gauss-bundels om de sturing en de effecten die de anisotropie van het materiaal en de array-parameters hebben op de bundel die zich door het materiaal voortplant, te simuleren. Het model is voor nauwkeurigheid gevalideerd met een numeriek model en een vergelijking van de modellen toont aan dat het ontwikkelde model rekenkundig efficiënter is.

In het tweede scenario wordt een model ontwikkeld om de Full matrix capture-signalen te simuleren tijdens het inspecteren van een gelaagd anisotroop materiaal zoals een Carbon Fiber Reinforced Plastic (CFRP) laminaat. Het model is ontwikkeld op basis van multi Gauss-bundels, de stijfheidsmatrixmethode en het hoekspectrum van vlakke golven om de ontvangen FMC-signalen van de inspectie van een CFRP-laminaat omgeven door een semi-oneindig vloeibaar medium te simuleren. De gesimuleerde signalen zijn vergeleken met de experimenteel verkregen signalen en vertonen een goede overeenkomst. Vanzelfsprekend zou de volgende stap in het proces de simulatie zijn van de verstrooiing door een defect in het laminaat. Aan de zijkant geboorde gaten (ZGH) zijn gebruikt als defect vanwege het gebruik als referentie en kalibratiedefecten. De analytische verstrooiing van de ZGH is gecombineerd met het eerder ontwikkelde model door het begrenzend medium te wijzigen in een in het algemeen anisotroop massief materiaal. FMC-signalen voor de verstrooiing van een ZGH worden gesimuleerd en afgebeeld met behulp van de totale focusseringsmethode, waarbij rekening wordt gehouden met de richtingsafhankelijke snelheid. Het voorgestelde model

VI

werd vervolgens gevalideerd met het beeld dat werd gegenereerd op basis van experimentele FMC-signalen en komt kwalitatief en kwantitatief goed overeen.

Concluderend leidt het werk in dit proefschrift tot twee hoofdresultaten. Het eerste hoofdresultaat is de ontwikkeling van een bundelmodel voor bundelvoortplanting van een phased array in een anisotroop materiaal. Hetgeen leidt tot een beter begrip van de invloed van verschillende materiaal- en arrayparameters en eigenschappen op de voortplanting van een bundel door dit materiaal heen. Het tweede hoofresultaat is de ontwikkeling van een model om de full matrix capture-signalen te simuleren die worden gegenereerd bij het inspecteren van gelaagde anisotrope materialen zoals een CFRP-laminaat met of zonder defect en de invloed van het aantal lagen, laagdikte, fabricageparameters en arrayparameters op de kwaliteit van het uitgangssignaal en het beeld dat wordt gegenereerd door nabewerking van deze signalen.

List of Symbols

p	Pressure of the wave	N/m^2
t	Time	s
c_f	Velocity of wave in fluid	m/s
∇	Laplacian operator	
ρ	Density of the medium	kg/m^3
v_0	Initial velocity on the face of the transducer	m/s
ω	Angular frequency of the wave	rad/s
s	Surface area of the transducer	m^2
$\{k\}$	Wavenumber vector of the wave	m^{-1}
r	Distance between transducer and point in medium	m
x_1, x_2, x_3	Coordinates of point in medium	m
a_1	Width of an element in an array	m
a_2	Length of an element in an array	m
$[c_{ijkl}]$	Elastic Stiffness matrix	N/m^2
$\{n_{j,k}\}$	Unit vector in the direction of propagation of wave where $k=1,2,3$	
k_i	Wavenumber component in $i=1,2,3$ direction	m^{-1}
c_p	Phase velocity of wave in the medium	m/s
δ	Kronecker Delta	
v	Velocity amplitude of wave in medium at a point	m/s
$[X]$	Coordinate vector	m
$\{d\}$	Polarization vector	
$[M]$	Matrix of phase of Gaussian beam	s/rad.m
$[S_p]$	Matrix of slowness curvatures	s/m
u_p	Group Velocity	m/s
C	Slowness surface curvature in the x_1 direction	m/s
E	Slowness surface curvature in the x_3 direction	m/s
D	Slowness surface curvature in the x_2 direction	m/s

IX

s_0	Slowness vector	s/m
s_{x1}	Slowness in x_1 direction	s/m
s_{x2}	Slowness in x_2 direction	s/m
s_{x3}	Slowness in x_3 direction	s/m
A_n	Wen and breazeale coefficient ($n=1$ to 10)	
B_n	Wen and Breazeale coefficient ($n=1$ to 10)	
A_m	Wen and breazeale coefficient ($m=1$ to 10)	
B_m	Wen and Breazeale coefficient ($m=1$ to 10)	
F	Focus distance	m
e	Pitch of the element	m
θ_j	Steering angle of element j	
N	Number of elements in the array	
D_r	Directivity of the element	
v_j'	Corrected velocity at a point from element j	m/s
[C]	Elastic stiffness matrix in Voigt notation	N/m ²
{u}	Plane wave displacement vector in medium	m
$a^{m,p\pm}$	Amplitude of the propagating wave of mode p in layer m in the upward (-) or downward (+) direction	
n	Number of layers in the laminate	
h	Thickness of layer of laminate	m
{ σ }	Stress vector	N/m ²
[S]	Recursive stiffness matrix	
[S _m]	Stiffness matrix of layer m	
[F ^{+/-}]	Matrix of force vectors of three modes of wave in upward (-) or downward (+) direction	
[D ^{+/-}]	Matrix of polarization vectors of three modes of wave in upward (-) or (+) direction	

X

$[\mathbf{H}^{+/-}]$	Diagonal matrix of propagation vectors of three modes of wave in upward (-) or downward (+) direction	
f	Acoustic wavefield on the face of transducer in wavenumber domain	
F	Acoustic wavefield on the face of the transducer spatial domain	
β	System function	
R	Total Reflection Coefficient	
T	Total transmission Coefficient	
$[\bar{C}]$	Equivalent homogeneous anisotropic elastic stiffness matrix	N/m ²
A_{scatt}	Nondimensional Scattering amplitude	
b	Radius of Side drilled hole	m
H	Hankel function	
$V(x_t, x_r, \omega)$	Nondimensional output signal in frequency Domain between a pair of elements	
$V_t(x_t, x_r, \omega)$	Frequency domain velocity on the surface of transmitting element	
$V_r(x_t, x_r, \omega)$	Frequency domain velocity on the surface of receiving element	
I	Intensity at the point x_1, x_3 in the medium	
σ_{RMS}	RMS value of the noise in laminate in region containing the scatterer	

List of Abbreviations

MGB	Multi Gaussian Beam
OMGB	Ordinary Multi Gaussian beam
LMGB	Linearly phased multi Gaussian beam
CFRP	Carbon Fibre Reinforced Polymer

XI

GFRP	Glass Fibre Reinforced Polymer
SDH	Side drilled hole
AF	Anisotropy Factor
FMC	Full matrix capture
TFM	Total Focusing method
SAFT	Synthetic Aperture Focusing Technique
FRP	Fibre Reinforced Polymer
NDE	Nondestructive Evaluation
NDT	Nondestructive Testing
FEM	Finite Element Method
PML	Perfectly matched layer
DPSM	Distributed point source method
SEM	Spectral Element method
FDTD	Finite Difference Time Domain
GTD	Geometrical Theory of Diffraction
PWI	Plane Wave Imaging
BEM	Boundary Element method
SNR	Signal to Noise Ratio
SH	Shear horizontal
SV	Shear Vertical
BWE	Backwall echo
BWA	Backwall echo analytical

List of Figures

Figure 2.1	Particle oscillations in a longitudinal wave.....	8
Figure 2.2	Particle Oscillations in Transverse wave.....	9
Figure 2.3	Transducer radiating into a medium.....	11
Figure 2.4	DPSM modelling of transducer.....	12
Figure 2.5	Elements in a phased array transducer.....	15
Figure 2.6	Cross section of an elliptical Gaussian beam.....	19
Figure 2.7	An ultrasonic testing setup.....	21
Figure 2.8	Phased array testing.....	22
Figure 4.1	Transducer radiating a Gaussian beam at an angle θ (group velocity direction).....	37
Figure 4.2	Shows the now rotated coordinates in the steering direction.....	41
Figure 4.3	(a) Beam field with quasi longitudinal and quasi shear waves (b) Wave numbers corresponding to quasi longitudinal and quasi shear waves (c) Beam field consisting of only quasi longitudinal wave	44
Figure 4.4	Setup considered for simulation.....	45
Figure 4.5	(a) Slowness surface (b) Slowness surface curvature (c) Beam Skew	47
Figure 4.6	(a) Beam field $C=E=0$ (b) Beam field $C=E=-2.5$ mm/ μ s (c) Beam field $C=E=-4.9$ mm/ μ s.....	48
Figure 4.7	(a) Beam field at a steering angle of 0° using OMGB (b) Beam field at a steering angle of 0° using LMGB (c) Beam field at a steering angle of 0° onaxis magnitude	50
Figure 4.8	(a) Beam field at a steering angle of 10° using OMGB (b) Beam field at a steering angle of 10° using LMGB (c) Beam field at a steering angle of 10° onaxis magnitude	51
Figure 4.9	(a) Beam field using COMSOL at steering angle of 30° (b) Beam field at a steering angle of 30° using LMGB (c) Beam field at a steering angle of 30° using OMGB	52
Figure 4.10	(a) On axis beam fields calculated using the analytical and numerical model for steering angle of (a) 20° (b) 30° (c) 45° ...	53
Figure 4.11	(a) On axis beam fields calculated using the analytical and numerical model for steering angle (a) 20° (b) 30° (c) 45° in dB scale.....	54
Figure 4.12	Difference in on-axis amplitudes (dB) for different steering angles between the LMGB and OMGB model	55

XIII

Figure 5.1	CFRP laminas specifying the local axis	61
Figure 5.2	Elements of an array transducer	68
Figure 5.3	Total Reflection coefficient for (a) Aluminum (b) CFRP laminate.....	69
Figure 5.4	System function of pair of elements with centre frequency of 2.25 MHz used for testing (a) Aluminium (b) CFRP laminate.....	70
Figure 5.5	System function of pair of elements with centre frequency of 5 MHz used for testing (a) Aluminium (b) CFRP laminate.....	70
Figure 5.6	FMC signals obtained for Aluminium with 2.25 MHz 64 element array (a) Experimental (b) Simulated.....	72
Figure 5.7	FMC signals obtained for Aluminium with 5 MHz 16 element array (a) Experimental (b) Simulated.....	73
Figure 5.8	FMC signals obtained for CFRP with 2.25 MHz 64 element array (a) Experimental (b) Simulated.....	75
Figure 5.9	FMC signals obtained for CFRP with 5 MHz 16 element array (a) Experimental (b) Simulated.....	76
Figure 5.10	FMC signals obtained for CFRP with 5 MHz 128 element array (a) Experimental (b) Simulated.....	77
Figure 6.1	Schematic diagram of laminate of N layers bounded by semi- infinite medium	85
Figure 6.2	Picture of (a) aluminium block (b) CFRP laminate with SDH used to verify the simulation results	94
Figure 6.3	Non-dimensional scattering magnitude of 1.5 diameter hole in aluminium at (a) 2.25 (b) 5 MHz frequency.....	96
Figure 6.4	TFM image of SDH FMC signals in aluminium using 2.25 MHz array (a) Simulated (b) Experimental	97
Figure 6.5	TFM image of SDH FMC signals in aluminium using 5 MHz array (a) Simulated (b) Experimental.....	98
Figure 6.6	A scaled comparison showing the simulated defect when inspected By (a) 2.25 MHz (b) 5 MHz array.....	100
Figure 6.7	Scattering amplitude as a function of angle of incidence for 0° (blue), 30° (orange) and 60 ° (yellow) for 1.5 mm diameter embedded in homogenized CFRP at (a) 2.25 MHz (b) 5 MHz.....	101

Figure 6.8	TFM image of simulated FMC signals in CFRP laminate (a) without SDH (b) with SDH using 2.25 MHz array.....	102
Figure 6.9	(a) Overlay image of simulated SDH signals with simulated composite laminate without SDH (b) TFM image of experimentally obtained signals when inspected by 2.25 MHz array.....	103
Figure 6.10	TFM image of simulated FMC signals in CFRP laminate (a) without SDH (b) with SDH using 2.25 MHz array.....	104
Figure 6.11	(a) Overlay image of simulated SDH signals with simulated composite laminate without SDH (b) TFM image of experimentally obtained signals when inspected by 5 MHz array.....	105
Figure 6.12	Group velocity of the longitudinal wave for different angles of propagation	107

List of Tables

Table 4.1	Material Properties of Austenitic Steel	45
Table 5.1	Transducer Array Specifications	68
Table 5.2	Material Properties	68
Table 5.3	Comparison of backwall amplitude reduction	78
Table 5.4	Comparison of backwall echo difference between experimental and Simulated results	78
Table 6.1	Transducer Array Specifications	94
Table 6.2	Equivalent Homogeneous Anisotropic Properties	95
Table 6.3	Comparison of SDH dimensions in Aluminium.....	99
Table 6.4	SNR of SDH in Aluminium.....	99
Table 6.5	Comparison of SDH dimensions in CFRP.....	106
Table 6.6	SNR of SDH in CFRP	106

Table of Contents

Summary	I
Samenvatting	V
Nomenclature	IX
List of Figures	XIII
List of Tables	XV
1. Introduction	1
1.1 General Introduction	2
1.2 Thesis Structure	3
1.3 References	4
2. Theory and Literature Review	7
2.1 Basic Theory of acoustic and elastic waves	8
2.2 Modelling of ultrasonic beam propagation	10
2.3 Scattering from defects	14
2.4 Phased array ultrasonic testing	14
2.5 Modelling a beam from phased array transducers	16
2.6 Wave propagation in anisotropic media	16
2.7 Modelling wave propagation in layered anisotropic media	18
2.8 Gaussian Beams	18
2.9 Imaging of Composite structures	19
2.10 Effective properties of laminated media	20
2.11 Data acquisition	20
2.12 Research Question	22
2.13 References	24
3. Methodology	31
3.1 Methodology followed for each sub question	32
3.2 References	34
4. Modelling of phased array radiation through anisotropic media using multi Gaussian beams	35
4.1 Introduction	36
4.2 Background theory of the paraxial MGB model for beam propagation in anisotropic media	36
4.3 Development of Ordinary and linearly phased MGB models for phased array beam propagation in anisotropic media	38
4.3.1 Development of the Ordinary MGB (OMGB) model for phased array	38
4.3.2 Development of Linearly phased MGB (LMGB) from an array into anisotropic media	40

XVII

4.3.3 Development of the FEM model using COMSOL	42
4.4 Simulation Results	44
4.4.1 Effect of slowness surface curvatures on the beam	46
4.4.2 Comparison of the OMGB and LMGB models below the paraxial limit	49
4.4.3 Comparison of OMGB, LMGB and FEM models above the paraxial limit	51
4.5 Discussions	56
4.6 Conclusions	57
4.7 References	57
5. A Gaussian beam based recursive stiffness matrix model to simulate ultrasonic array signals from composite laminates	59
5.1 Introduction	60
5.2 Theory	61
5.2.1 Stiffness matrix method for multilayer propagation	61
5.2.2 Modelling of the transducer Gaussian beams	64
5.2.3 Angular Spectrum of plane waves	65
5.3 Development of model to simulate the FMC signals	66
5.4 Simulation and Experimental Results	67
5.4.1 Total Reflection Coefficient of the materials under inspection	69
5.4.2 System Functions of the transducer arrays	70
5.4.3 Comparison of experimental and Simulated FMC signals	71
5.4.3.1 Experimental and Simulated FMC signals in Aluminum	71
5.4.3.2 Experimental and Simulated Signals in CFRP	74
5.5 Discussions	78
5.6 Conclusions	79
5.7 References	80
6. Modelling the scattering from a side drilled hole embedded in a layered anisotropic medium	83
6.1 Introduction	84
6.2 Background Theory	84
6.2.1 Transfer Matrix method	84
6.2.2 Equivalent homogeneous anisotropic properties of a thick laminate	86
6.2.3 Scattering coefficient of side drilled hole	88
6.3 Development of model to facilitate scattering of SDH in an layered anisotropic medium	89

6.3.1 Reflection and Transmission coefficients of layered structure bounded by anisotropic media	89
6.3.2 Calculation of the scattering from SDH embedded in the medium	91
6.3.3 TFM Imaging	92
6.3.4 Quantitative comparison of the images	92
6.4 Simulation Results	93
6.4.1 Calculation of equivalent homogeneous properties	95
6.4.2 SDH embedded in Aluminum inspected by a 2.25 and 5 MHz array	96
6.4.3 SDH embedded in CFRP inspected by arrays of center frequencies 2.25 and 5 MHz	100
6.5 Discussions	107
6.6 Conclusions	108
6.7 References	109
7. Conclusions and Future Work	111
7.1 Linearly phased Multi Gaussian beam model for beam propagation for phased array into an anisotropic media	112
7.2 A Gaussian beam based recursive stiffness matrix model to simulate the ultrasonic array signals from composite laminate	113
7.3 Modelling the scattering from a side drilled hole embedded in a layered anisotropic medium	113
7.4 Recommendations for future work	115
7.5 References	116
Appendix	117
Acknowledgements	121
List Of Publications	123
Curriculum Vitae	124

XX

1

Introduction

1.1 General Introduction

Modern aircraft are constructed of various materials in complex shapes and structural configurations. Aluminium alloys constitute a significant amount of the airframe. Steel and Nickel alloys are used in landing gear components, horizontal stabilizer spindles, engines, etc [1]. In recent years also fibre reinforced plastics (FRP) such as carbon fibre reinforced plastics (CFRP), Honey comb sandwiched panels and fibre metal laminates (FML) are being used in aircraft constructions due to their light weight and high strength to weight ratio. Driven by the need to reduce fuel consumption costs more complex shaped structures have found their applications in recent aircrafts such as the Boeing 787 and the Airbus A350 [2]. Damages and defects may occur during the lifecycle of an aircraft which includes the design, production and inservice phases. These defects and damages may vary in sizes, severity and location[3]. It is imperative to carry out nondestructive testing to detect, locate, measure and identify these defects or damages so as to decide on a further course of action which could involve taking no corrective action, repairing or scrapping the part based on the allowable limits [4].

There are a plethora of Nondestructive testing (NDT) techniques which are being used in the industry to test aircraft structures made from isotropic and anisotropic materials such as visual inspection, ultrasonic testing, eddy current testing, X- ray techniques, Thermography etc [4]–[9]. Out of all these techniques ultrasonic testing is most widely used due to the flaw detection [10] coupled with cost, safety and ease of use. Currently ultrasonic testing of composite structures is carried out using a single normal incidence transducer where the attenuation and the location of defects is estimated by the magnitude and location of the backwall echo. This technique works well for simple isotropic structures but while testing anisotropic structures with complex geometry such as curved composite structures this method has poor defect detectability and characterization.

Ultrasonic phased arrays are being used increasingly in the industry due to their ability for greater depth penetration, rapid inspection, defect characterization and providing more information to the user about the structure being inspected. Phased arrays can be used to steer the ultrasonic beam so as to facilitate inspection of larger areas. The advantages of using ultrasonic arrays have led to more research in advanced NDT methods using such arrays[11]. Conventionally in order to generate an image using an imaging algorithm, different transducers/ receivers in the array are used with preprogrammed delay and sum rules to generate the image. Another approach has been suggested by Holmes et al [12] which uses the full matrix capture in which the full matrix data of transmit and receive element

combinations are captured experimentally and any imaging algorithm can then be applied to this data. Some of the widely used algorithms are the Total Focusing Method (TFM) and the Synthetic Aperture Focusing Technique (SAFT) [13], [14]

There are many challenges encountered during testing of anisotropic layered or homogeneous media owing to the anisotropic properties of the material being inspected. The anisotropic nature of the material influences the velocity of the ultrasonic wave traveling through it which affects the location and sizing of the defects [15], [16]. The layer interfaces present in the FRP give rise to multiple reflections which interfere with the output signals and might cause misinterpretation of the received signal [17], [18].

Advanced methods can be developed using both experimental and empirical methods to test such anisotropic structures and to study the structural influence on the output signal. However using experimental methods has its economical limitations as it is difficult to make a lot of samples to be statistically valid conclusions. Hence it is required to develop forward models which help in understanding how the ultrasonic signals interact with homogeneous anisotropic or layered anisotropic materials, carry out qualitative and quantitative analysis of signals in such structures and ultimately lead to the development of advanced NDE methods for these materials. These forward models can also be used to test imaging algorithms and to study the different parameters which affect the imaging algorithms.

1.2 Thesis structure

The thesis is divided into seven chapters and consists of four main chapters, introduction and conclusion.

Chapter 2: Theory and Literature review

This chapter will deal with the theory and literature present on beam modelling for isotropic /anisotropic structures, wave propagation in anisotropic, layered structures, imaging, data acquisition, phased array testing. The chapter concludes with identifying the gaps in the literature leading up to the research question addressed in Chapter 3.

Chapter 3: Methodology

This chapter states the research questions and explores the methodology adopted to investigate these questions.

Chapter 4: Modelling of beam propagation from phased arrays in anisotropic media

This chapter will deal with the development of the nonparaxial multi Gaussian beam model. It includes the development of a nonparaxial beam model for isotropic structures which is then modified to simulate the beam propagation in homogeneous anisotropic structures. This general purpose beam model is verified using Finite element models and details the effects of anisotropy on the beam and beam steering.

Chapter 5: A Gaussian Beam Based Recursive Stiffness Matrix Model to Simulate Ultrasonic Array Signals from Multi-Layered Media

In this chapter a model is described to test multilayered FRP laminate. The model consists of Gaussian beam coupled with the recursive stiffness matrix of the structure under inspection. The model outputs full matrix capture signals and a comparison between experimental and simulated signals is presented.

Chapter 6: Simulating the scattering from Side drilled holes in multi layered media

In this chapter the model developed in Chapter 5 is modified so as to accommodate isotropic/anisotropic bonding layers and is coupled to the scattering from side drilled holes to simulate the testing of such reference defects. The simulated and experimentally obtained signals are compared. A modified TFM algorithm and the results are presented

Chapter 7: Conclusions and Future Work

This chapter presents the conclusions of the thesis and suggestions on the future work which can be carried out.

1.3 References

- [1] J. C. Williams and E. A. Starke, "Progress in structural materials for aerospace systems," *Acta Mater.*, vol. 51, no. 19, pp. 5775–5799, 2003, doi: 10.1016/j.actamat.2003.08.023.
- [2] C. Kassapoglou, *Design and Analysis of Composite Structures*. Oxford, UK: John Wiley & Sons Ltd, 2013.
- [3] A. Fahr, "Aeronautical Applications of Non-destructive Testing," *DEStech Publications*, 2014. .

- [4] R. H. Bossi and V. Giurgiutiu, "Nondestructive testing of damage in aerospace composites," in *Polymer Composites in the Aerospace Industry*, Elsevier, 2015, pp. 413–448.
- [5] M. Namkung, B. Wincheski, and N. Padmapriya, "NDT in the Aircraft and Space Industries," in *Reference Module in Materials Science and Materials Engineering*, 2016.
- [6] W. Steinchen, L. Yang, G. Kupfer, and P. Mäckel, "Non-destructive testing of aerospace composite materials using digital shearography," *Proc. Inst. Mech. Eng. Part G J. Aerosp. Eng.*, 1998, doi: 10.1243/0954410981532108.
- [7] J. H. Heida, J. P. Derk, "Evaluation of non-destructive inspection methods for composite aerospace structures," *6th NDT Prog. 2011*, pp. 1–12, 2011, [Online]. Available: http://www.ndt.net/article/ndtp2011/papers/1_Heida.pdf.
- [8] U. Schnars and R. Henrich, "Applications of NDT Methods on Composite Structures in Aerospace Industry," *Conference on Damage in Composite Materials*, pp. 1–8, 2006, [Online]. Available: http://marinecompositesnde.com/images/Schnars_2006.pdf.
- [9] R. A. Smith, S. Mukhopadhyay, A. Lawrie, and S. R. Hallett, "Applications of ultrasonic NDT to aerospace composites," *5th Int. Symp. NDT Aerosp.*, 2013.
- [10] ASTM International, "ASTM E2533-09 Standard Guide for Nondestructive Testing of Polymer Matrix Composites Used in Aerospace Applications," *Annu. B. ASTM Stand.*, 2009, doi: 10.1520/E2533-09.part.
- [11] P. D. Wilcox, "Ultrasonic arrays in NDE: Beyond the B-scan," *Rev. Prog. Quant. Nondestruct. Eval. Vol. 32*, vol. 1511, no. 1, pp. 33–50, 2013, doi: 10.1063/1.4789029.
- [12] C. Holmes, B. Drinkwater, and P. Wilcox, "The post-processing of ultrasonic array data using the total focusing method," *Insight Non-Destructive Test. Cond. Monit.*, vol. 46, no. 11, pp. 677–680, 2004, doi: 10.1784/insi.46.11.677.52285.
- [13] C. Holmes, B. W. Drinkwater, and P. D. Wilcox, "Advanced post-processing for scanned ultrasonic arrays: Application to defect detection and classification in non-destructive evaluation," *Ultrasonics*, vol. 48, no. 6–7, pp. 636–642, 2008, doi: 10.1016/j.ultras.2008.07.019.
- [14] M. H. Skjelvareid, T. Olofsson, Y. Birkelund, and Y. Larsen, "Synthetic aperture focusing of ultrasonic data from multilayered media using an omega-K algorithm," *IEEE Trans. Ultrason. Ferroelectr. Freq. Control*, vol. 58, no. 5, pp. 1037–1048, 2011, doi: 10.1109/TUFFC.2011.1904.
- [15] M. Spies, "Modeling of transducer fields in inhomogeneous anisotropic materials using Gaussian beam superposition," *NDT E Int.*, vol. 33, no. 3, pp. 155–162, 2000, doi: 10.1016/S0963-8695(99)00036-5.
- [16] R. Long, J. Russell, P. Cawley, N. Habgood, D. O. Thompson, and D. E. Chimenti, "Ultrasonic Phased Array Inspection of Flaws on Weld Fusion Faces Using Full Matrix Capture," *AIP Conf. Proc.*, vol. 848, no. 2009, pp. 848–855, 2009, doi: 10.1063/1.3114345.
- [17] S. Mahaut, S. Legoupil, F. Grassin, and H. Walaszek, "Ultrasonic Inspection of Composites : Challenges and Solutions for."
- [18] P. Cawley, M. Engineering, and I. College, "Inspection of Composites – Current Status and Challenges," *Ecndt 2006*, pp. 1–10, 2006.

2

Theory and Literature Review

Chapter 2 provide the relevant theory and literature review required for this thesis. This theory and literature review address general theory about waves, modelling of ultrasonic beams, wave propagation in anisotropic homogeneous and layered structures, scattering from defects in materials, ultrasonic phased arrays, data acquisition, imaging algorithms and equivalent homogeneous anisotropic properties. This then leads to recognize gaps in the research and the formulate the research question and sub questions which this thesis attempts to answer. In the next section a brief theory of elastic waves is provided.

2.1 Basic theory of acoustic and elastic waves

An acoustic wave is composed of oscillations of discrete particles of material. In fluids the propagation of a wave is governed by Eq. (2.1)

$$\nabla^2 p - \frac{1}{c_f^2} \frac{\partial^2 p}{\partial t^2} = 0 \quad (2.1)$$

Where ∇^2 is the laplacian operator, c_f is the speed of sound in a fluid, p is the pressure in the fluid, t is the time.

Elastic wave is the wave which propagates in solids and is dependent on the properties of the solids. The elastic wave propagation is given by Eq. (2.2)

$$\mu \nabla^2 \mathbf{u} + (\lambda + \mu) \nabla (\nabla \cdot \mathbf{u}) - \rho \frac{\partial^2 \mathbf{u}}{\partial t^2} = 0 \quad (2.2)$$

Where \mathbf{u} is the particle displacement vector, μ and λ are Lamé's constants.

When the particles oscillate in the direction of the propagation of the wave, the wave is called a longitudinal wave. The direction of oscillation of particles is called the polarization of the wave. Since compressional and dilatational forces are active in the wave, it is also called as a compression wave or a pressure wave. This is the real sound wave because it can transmit the oscillations of a source of acoustic energy through the air to our ears. The same wave also transmits sound through liquid or solid bodies.

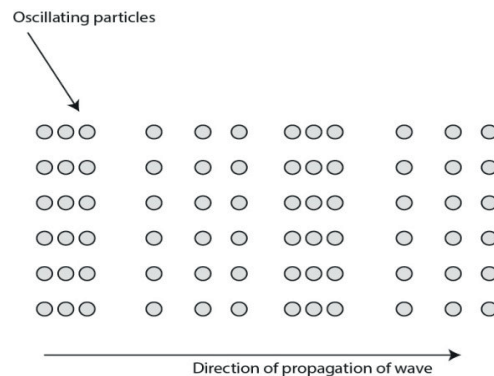


Figure 2.1. Particle oscillations in a longitudinal wave

However, in solid bodies another kind of wave may also occur. This wave is called a transverse wave as the particles no longer oscillate in the direction of propagation of wave but at right angles to it as shown in Figure 2.2.

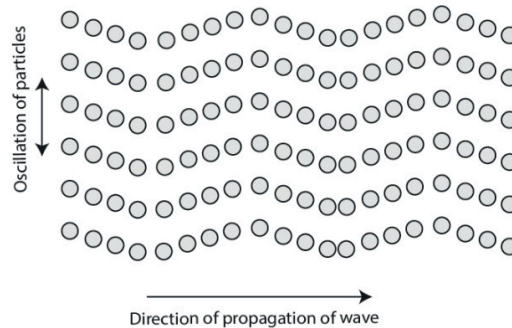


Figure 2.2 Particle oscillations in a transverse wave

This wave is also called a shear wave. Since liquids and gases are incapable of transmitting shear, transverse waves cannot travel through them [1]. Waves have different velocities and the longitudinal wave velocity is typically more than twice the shear wave velocity in metals.

The waves described above are for infinite medium and are not restricted by the size or shape of the medium of propagation. For finite bodies, there are different waves which can be defined by the deformation of the bodies. Some of these waves are Surface or Rayleigh waves [2] which exist on the surface of a flat or curved medium which is otherwise infinite and involves the motion of only the top row of particles of the solid medium. When a solid medium is further limited in size to a finite thickness, a pure surface cannot exist unless its wavelength is much smaller than the thickness of the plate. In such a solid we have Lamb waves which propagate along the wave with particles oscillating perpendicular to the direction of propagation. Lamb waves are also called guided waves and are of symmetrical and asymmetrical modes [3].

The reflection and transmission of wave impinging an interface between two materials depends on the acoustic impedance of the materials and the angle of incidence. Acoustic wave impedance is a property of a material which provides the resistance of the material to the propagation of a wave through it. The different acoustic impedances of materials cause reflection and transmission of waves at the interface between one material to another.

Furthermore elastic wave propagation is complicated by the fact that mode conversion occurs at a non-normal angle of incidence, and also that reflection/refraction occur at a discontinuities inside a test object. In mode conversion a longitudinal wave impinging at an interface will be converted to a shear wave or vice-versa depending on the acoustic impedance mismatch between the two materials.

A typical example from Non-destructive Evaluation (NDE) imaging is the multiple mode conversion that can occur at cracks[4]. There, mode conversion generates both longitudinal and shear diffracted waves at the tip of the crack. A surface wave may also be generated along the crack, which has a different speed and hence will result in additional diffracted waves at the crack tips [5]. The resulting signals will then consist of a mix of different wave modes which will be very difficult to discriminate.

The next section describes the efforts to model ultrasonic beam propagation from transducers.

2.2. Modelling of Ultrasonic beam propagation

A typical ultrasonic NDE model consists of three fundamental components. A) the source of the ultrasound b) Propagation and scattering of waves through a medium of different geometrical and material properties and c) Scattering from defects embedded in the specimen [6]. This section describes modelling techniques which are used for modelling the beam emitted from transducers.

In NDE applications, the ultrasonic beam emitted by the transducer undergoes changes while propagating through the test structure. The shape and size of the propagating beam affects the received signals and hence it is beneficial to model the propagation of beams to understand the effects of the structure on the beam.

Beam modelling for single element transducers has been carried out using exact, semi analytical and numerical methods [7]. A standard beam model setup for a transducer radiating ultrasonic waves into a medium is shown in Figure 2.3 where x_1 , x_2 and x_3 are the coordinate axes.

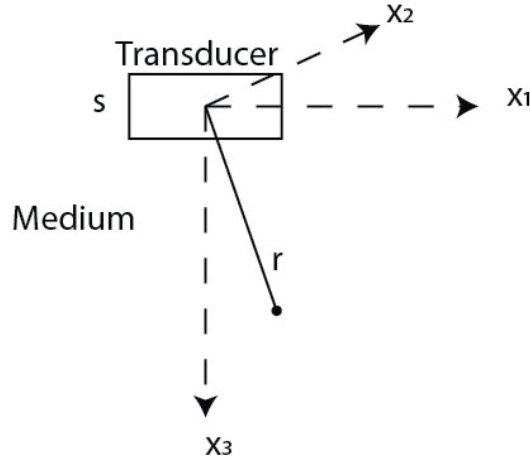


Figure 2.3. Transducer radiating ultrasonic waves into a medium

Exact methods use the superposition of point sources to model the transducer beam. In the point source method point sources are superimposed on the face of the transducer using Rayleigh-Sommerfeld integrals as shown in Eq. (2.3) [8].

$$p(X, \omega) = \frac{-i\omega\rho v_0(\omega)}{2\pi} \int_s \frac{\exp(ikr)}{r} ds \quad (2.3)$$

Where p is the pressure at coordinates X in the medium, ρ is the density of the medium, s is the surface area of the transducer, r is distance from the face of the transducer to a point in the medium, ω is the angular frequency and v_0 is the initial velocity at the face of the transducer

The exact methods might lead to multiple integrals on the surface of the transducer and on the interfaces which are encountered in the structure [9]. These integrals are solved using numerical integration or by other methods such as the edge element method proposed by Lerch et al. [10]. Spies [11] circumvented solving the multiple integrals by using the saddle point method. These superposition techniques can be used to model the beam transmitted across interfaces but require a large number of point sources making them less efficient. The pencil method [12]–[14] is another method which is used to carry out wavefield computations in homogeneous isotropic and anisotropic media. The Pencil method considers the emitting transducer to be made up of many point sources emitting a bundle of paraxial rays. In the pencil method, numerical integration also needs to be carried out as point sources are considered [15].

Another method introduced by Kundu et al. is the Distributed point source method (DPSM) [16]–[19] which is a technique based on the superposition of

fundamental solutions related to the source and target point. The method employs a collection of points distributed on the interfaces and boundaries present in the structure as shown in Figure 2.4.

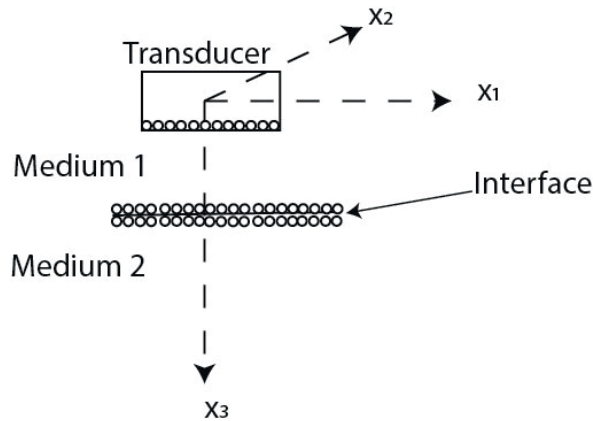


Figure 2.4 Discrete Point Source Modelling of a transducer.

These points are of unknown strength. Boundary conditions are then imposed from which a system of equations with the unknown strengths is obtained. The solution for the unknown strengths then requires calculating the Green's function for the media between the source and target points. This method can also be used for layered structures [20]. For isotropic media Green's function is a closed form algebraic expression whereas for anisotropic media the governing equations are more complex and Green's function to calculate the unknown strengths at the distribute point sources needs to be evaluated numerically and hence becomes computationally expensive [21].

The Finite Element Method (FEM) [22] has also been employed to model beam propagation in structures. FEM has been used to compute wave propagation in isotropic and anisotropic media [23], [24][25], [26]. It remains non-singular for complex geometries and curved surfaces [27]. Finite element methods require the discretization of the entire modelling medium which increases the required computational time and power especially when a 3-D solution is required. FEM also requires the use of absorbing boundaries [28] and the reflection from these boundaries in most cases cannot be avoided as using of perfectly matched layers (PMLs) reduces the reflection from medium boundaries but is incapable of completely eliminating them [28]. Recently the spectral element method (SEM) has been used to model wave propagation in anisotropic media [29]–[31]. SEM allows the usage of basis functions in the form of high order polynomials such as the Legendre polynomials, Chebyshev polynomials, etc which lead to higher accuracy over non uniformly spaced nodes [32]. SEM converges faster to the exact

solution than FEM due to the use of high order polynomials and reduced degrees of freedom of the structure. The drawback of SEM lies in the difficulty to program complex geometries and also the high computational cost per degree of freedom [33].

Finite Difference Time Domain (FDTD) Methods are also used for computing the wavefields in complex geometries [34]–[37]. FDTD requires the computational domain to be discretised into grids and the spacing of the grid should be fine so as to be able to resolve the smallest wavelength and the smallest features in the model. This becomes computationally expensive and can lead to high computational times [38].

An alternative method for modelling the beam from finite width transducers which is based on the paraxial approximation is to model the radiation as a superposition of Gaussian beams [39]. As Gaussian beams are based on the paraxial approximation it has been shown that it is possible to analytically calculate the reflection and transmission of such beams at planar and curved interfaces[40]–[43]. Following this work Huang developed the Multi Gaussian Beam (MGB) model for a single transducer to simulate propagation through an anisotropic medium. The Multi Gaussian beam is computationally efficient as it requires the superposition of a small number of Gaussian beams and is accurate within the paraxial approximation. Following Huang's work, the MGB model for a single transducer was then applied for composite curved parts.

Another method is to model the wavefield by a superposition of plane waves at the face of the transducer (angular spectrum) as plane waves can be analytically transmitted and reflected from planar interfaces [44]–[46]. The method of angular spectrum is also computationally efficient due to the use of Fourier transformation. Although this method can be used for anisotropic materials it is not viable for curved interfaces as it leads to singularities.

To summarize, the models based on FEM, FDTD, DPSM and Rayleigh Sommerfeld methods are non-singular when interacting with curved surfaces, can be used to model complex geometries but are computationally expensive as they either require discretization of the domain, evaluation of multiple integrals or a large number of elements. Modelling based on SEM is faster than FEM but is difficult to program for complex geometries and is still computationally expensive. Angular spectrum based modelling is computationally efficient but singularities occur when interacting with curved interfaces. Models based on the superposition of Gaussian beams have been shown to be computationally efficient and non-singular when interacting with curved interfaces.

The next section presents models for scattering from defects.

2.3. Scattering from defects

In NDE ultrasonic waves are used to inspect materials with flaws in them. The wave from the transducer travels through the material, interacts with any flaws that are present and is then scattered back to the transducer. Hence the received signal depends heavily on the type of flaw present and the scattering by the flaw. To solve the waves scattered by a flaw in an elastic solid, a complex boundary value problem needs to be solved. Numerical methods such as FEM [24], [25], [47]–[49], Finite Difference [50], Boundary Element Method (BEM) [51], T-matrix methods, etc, have been used to solve flaw scattering problems. These numerical methods are limited by the small wavelengths required for the flaw scattering at high frequencies due to which the computational domain becomes large and the methods become computationally inefficient.

This led to the development of approximate methods such as the Kirchoff approximation [7], [43], [52], [53], Born approximation [7], [54], geometrical theory of diffraction (GTD) [55], [56] etc. The Kirchoff approximation is a high frequency approximation which requires $ka > 1$ where a is the characteristic flaw dimension and k is the wavenumber. Huang et. al [43] showed that the Kirchoff approximation works well to describe the major characteristics of the pulse echo reflection for flaws with $ka < 1$. In the Kirchoff approximation it is assumed that the part of the flaw where the wave strikes can be described as an interaction between a plane wave and a plane interface. On the remainder of the surface the wave field is assumed to be zero due to which creeping waves are not taken into account. Huang [43] also showed that for anisotropic stress free scatterers embedded in anisotropic media, the Kirchoff approximation is the same as that of isotropic media. For geometrically simple flaws the boundary value problem can be solved exactly by the method of separation of variables [57].

In the next section I will introduce phased array ultrasonic testing

2.4. Phased array ultrasonic testing

Ultrasonic testing is the most widely used technique for the inspection of composites and bonded joints. The test may be carried out by using a single transducer in pulse-echo, two transducers in through transmission mode or a phased array. In either case it is compulsory that the transducers be coupled to the structure via a liquid medium due to the severe impedance mismatch between air and solid materials [58].

In a phased array ultrasonic setup, the transducer is composed off an array of small piezo electric elements, where each element of the array can be separately driven and the response of each element independently received. Figure 5 shows a linear array consisting of identical rectangular elements where the length of the elements in the x_1 direction a_1 is much smaller than the length in the x_2 direction a_2 . The gap length between the elements g is the same for all the elements, and the element to element spacing s is called the pitch of the array [59].

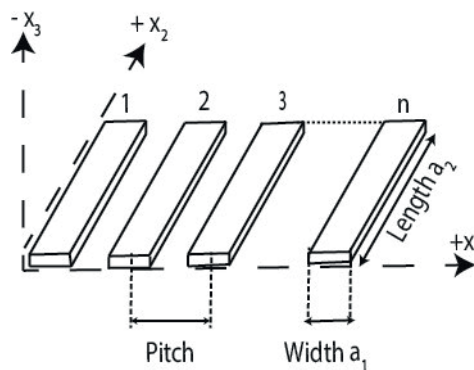


Figure 2.5. Elements in a phased array transducer

In order to steer the beam of ultrasonic wave in a required direction, time delay laws need to be applied to the elements of the array depending on the angle and the focusing distance required.

In recent years due to the requirement of quicker inspection speeds and ease of interpretation over conventional NDE, ultrasonic arrays were implemented in industry. Early research work on arrays began in the fields of radar (Electromagnetic wave) and sonar (Acoustic wave) systems for tracing objects in motion [60]. Arrays were adapted into these fields as in order to locate objects, the beam needed to be steered and this could easily be done as air and water were isotropic and homogeneous media [61]. The ease with which the beam from an array could be steered attracted the attention of the medical field which led to the development of ultrasound phased array, which was able to focus and steer the ultrasound energy to a particular point in the body [62]. In medical science the material properties of the test objects have acoustic impedances close to that of water and are conformable allowing a range of transducer shapes to be easily used and manipulated. The fluid like properties of the body also mean that only longitudinal waves are present, significantly simplifying the imaging [63]. The key developments in phased array technology were then transferred to the NDE field.

The next section provides a review of the modelling of beams from phased array transducers.

2.5. Modelling of beam from phased array transducers

A phased array consists of multiple transducer elements to which time delays can be applied allowing the steering of the ultrasonic beam in any desired direction or the focusing of the beam at a specific location. Beam steering and focusing of phased array transducers has been studied extensively by Azar et al. [64] which led to the formulation of time delay laws. To predict the wave field generated from arrays, single element models such as the Rayleigh Sommerfeld have been expanded and applied for an array of transducers [59]. However, the exact and numerical models for an array of transducers face the same drawbacks as stated earlier for the single element models. Kim et al. generated the basis sets for Gaussian beams emitted from rectangular shaped array elements by applying a clever use of the circ function [65]. Park et al. then expanded the Multi Gaussian beam model [66] for phased array transducers radiating into an isotropic medium and observed that beam steering above 20° was not accurately calculated as the beam is steered at an angle exceeding the paraxial limit of about 20° . To facilitate beam steering beyond the paraxial limit, a multi Gaussian beam model based on the application of a linear phasing on the array element face was developed in isotropic structures by Huang et al. [67].

Anisotropy of the material under inspection affects the propagation of the radiating ultrasonic beam from single element and array transducers [68]. While testing of multi-layered structures such as composite structures, more importance is placed on the received signal than on tracing the individual beam propagation and reflections in each ply.

The next section presents theory and literature review about wave propagation in anisotropic media.

2.6. Wave propagation in Anisotropic media

As stated in chapter 1, homogeneous anisotropic materials and layered composite materials are being widely used in aircraft structures. Hence regular ultrasonic non-destructive testing of these structures is carried out which is complicated due to the anisotropy and layering of such structures. Hence the focus of this thesis is on anisotropic homogenous materials such as austenitic steel and anisotropic layered structures such as composite materials.

Wave propagation in anisotropic media is complicated due to the existence of two different velocities. Composite materials are known to exhibit anisotropic behaviour. The stiffness matrix is composed of 21 independent stiffness coefficients and as such, purely anisotropic materials are rare. In laminate composite materials, the system of layers that extend in the x-y direction make the material orthotropic and hence the number of independent coefficients decreases to 9 [69]. A laminate with a balanced stacking sequence with plies at various orientations, for example [0/+45/90/-45/-45/90/+45/0] will lead to a quasi-isotropic behaviour in the plane of the layers [69].

The link between material properties and the ultrasonic wave propagation is given by the Christoffel equation [70], [71] as shown in Eq. (2.4).

$$c_{ijkl}n_jn_k - \rho c_p^2 \delta_{il} = 0 \quad (2.4)$$

Where c_{ijkl} are the elastic constants, n is unit vector in the direction of wave propagation, ρ is the density of the material, c_p is the phase velocity, δ is the kronecker delta and $i, j, k, l = 1, 2, 3$.

Given that the material properties are known from mechanical tests or data sheets from the manufacturer, the phase velocity can be calculated as functions of the angle of propagation. As shown in previous studies [72], [73], the inverse problem can be treated and if the velocities are known, the mechanical properties can be calculated. According to Love-Kirchoff shell theory and Classical laminate theory [74], an accurate determination of stiffness parameters is possible when the thickness of the component is much smaller than the other physical dimensions, typically a few millimetres [75]. Also work has been done on thick samples up to 19 mm thick [76].

In anisotropic materials the velocity with which the wavefront travels or the velocity of the wave in the energy direction is called the group velocity [77]. The velocity at which the phase of the wave travels is called the phase velocity and in a direction perpendicular to the wavefront. It is important to note that the Christoffel equation is valid only with the phase velocities. For isotropic materials both the group and phase velocity have the same magnitude and same direction of propagation when no dispersion takes place (velocity is independent of frequency). However this is no longer true for anisotropic materials due to dispersion with the material. In anisotropic materials because of the dispersion due to the oriented internal structure of the medium, the wave front will be distorted which will induce beam skewing [77].

2.7. Modelling Wave propagation in layered anisotropic media

A variety of approaches to simulate the response from multilayer structures have been reported in literature. One of these approaches is applying ray methods to the homogenized multilayer structure [14]. Though these have the advantage of being applicable to planar and curved geometries, they fail to show the effect of reflection and reverberation from the plies on the received signal due to the homogenization of multi-layered media as a single homogeneous medium.

A hybrid Ray-FDTD approach was developed which utilizes ray methods for propagation through the coupling medium and the FDTD method to calculate the response of the layered medium [78]. This method can solve for complex geometries but is time consuming and computationally expensive as it employs FDTD.

A different approach is to use highly effective plane wave models from geophysics literature to calculate the reflection and transmission at the layer interfaces [79]–[82]. The Transfer matrix method developed by Thomson [81] and Haskell [80] are the basic matrix formulations which have been used. These suffer from instability problems for large frequency/thickness (fd) products where f is the frequency and d is the thickness of the layer. Knopoff [79] suggested a global matrix method to overcome the instability problems. For anisotropic media Nayfeh [77] developed the transfer matrix method which again suffered from stability problems. Rokhlin and Wang [83] developed the recursive stiffness matrix method which uses individual layer stiffness matrices to build up the global stiffness matrix for the entire laminate.

The plane wave models for multi-layered media above do not reflect the real situation where a finite size transducer is used which emits a bounded beam. The diffraction of the bounded beam can be modelled using the angular spectrum, where the fields anywhere in the space can be defined as a sum of an infinite number of plane waves in different directions but this does not take the effects of a finite width transducer into account.

2.8. Gaussian Beams

Construction of the bulk wave propagation from ultrasonic transducers involves the accurate superposition of a number of plane or spherical waves. As the beam from an ultrasonic transducer is highly directional, the paraxial approximation is an appropriate approximation to be applied to the propagating beam. This leads to considering superimposing of a small amount of Gaussian

beams. Hence the solution for a Gaussian beam of elliptical cross section traveling along the x_3 direction is given by the Eq. (2.5) [7].

$$p = P_0 \sqrt{\frac{q_{x0}q_{y0}}{q_x q_y}} \exp \left[ikx_3 + \frac{ik}{2} \left(\frac{x_1^2}{R_{x_1}(x_3)} + \frac{x_2^2}{R_{x_2}(x_3)} \right) - \left(\frac{x_1^2}{w_{x_1}(x_3)} + \frac{x_2^2}{w_{x_2}(x_3)} \right) - i\omega t \right] \quad (2.5)$$

Where P_0 is the initial pressure, q_{x0} and q_{y0} are complex constants, q_x and q_y are complex functions to satisfy the paraxial equation, w_{x1} and w_{x2} are the widths of the Gaussian beam in the x_1 and x_2 directions respectively, k is the wavenumber, R_{x1} and R_{x2} are the radii of the Gaussian beam in the x_1 and x_2 directions respectively as shown in Figure 2.6.

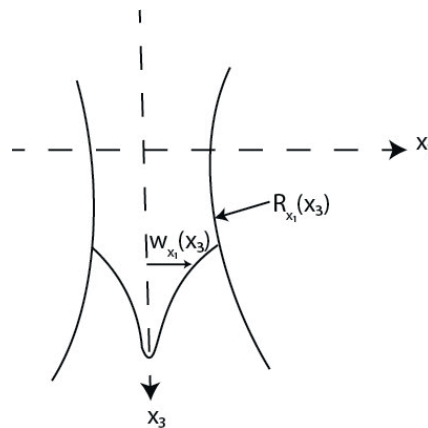


Figure 2.6 Cross section of an elliptical Gaussian beam

The next section gives an overview of algorithms used for imaging structures

2.9. Imaging of composite structures

The development of the full matrix capture (FMC) [84] data acquisition technique allows the application of post processing algorithms to image the structure. Time domain methods such as the Synthetic Aperture Focusing Technique (SAFT) [85], Total Focusing Method (TFM) [86]–[88] and plane wave imaging (PWI) [89] have been used to image isotropic structures. Frequency domain algorithms such as the wavenumber algorithm [90] have been applied to image isotropic structures for computational efficiency. For imaging anisotropic structures, the TFM has been modified using the Backwall reflection method to experimentally calculate the velocity and to account for the changing velocity [91]–[93]. In recent years research regarding Nonlinear imaging algorithms [94]–

[96] has increased but these methods still suffer from detection accuracies due to nonlinearities produced due to equipment and cannot be used directly on the FMC data.

To account for the anisotropic velocity in layered anisotropic media, it is beneficial to model the entire laminate as a homogeneous anisotropic medium and to obtain the velocities using these effective properties. The next subsection presents the homogenization methods used for layered isotropic and anisotropic media

2.10. Effective properties of laminated media

Over the years various methods have been developed to obtain the effective or homogeneous properties of isotropic and anisotropic layered media. Classical laminate theory works well for thin laminates but as the thickness of the laminate increases higher order plate theories are used which are mathematically complex. Hence for thick laminates, earlier efforts were concentrated on obtaining the equivalent stiffness constants of laminate made with isotropic layers by employing dispersion and elastic wave propagation theories [97], [98]. Continuum theory was applied by Sun et. al [99] in which the microstructure of an alternate layered medium was modelled. Another approach by Enie and Rizzo [100] was to apply classical laminate theory for in plane properties. Out of plane properties were predicted based on assuming uniform in-plane strain and uniform interlaminar normal and shear stress distributions. Sun et.al assumed the continuity of interlaminar stresses across ply boundaries and continuity of in plane strain through the thickness of the laminate. They developed closed form expressions for the effective properties taking the anisotropic nature of the plies into account. A boundary value approach was used by Roy and Tsai [101] which used Airy stress functions to calculate the three dimensional effective properties of the laminate. Chen and Tsai [102] assumed a parabolic variation of the interlaminar shear stresses in the laminate to account for the effect of the stacking sequence for symmetric laminates.

2.11. Data acquisition

An ultrasonic NDE system involves the generation, propagation and reception of short transient signals. The driver of the system is the pulser section of a pulser-receiver. The pulser puts out very short repetitive electrical pulses having amplitudes in the order of several hundred volts. These electrical pulses drive the transducer (usually consisting of a single element crystal or several

elements when used as an array) in contact with a part being examined, and these are converted into mechanical energy, which then propagates as a beam of ultrasound in the part. If a flaw is present in the path of the beam, some part of the incident ultrasonic wave will be scattered in different directions and can be picked up by the same transducer or a different one as shown in Figure 2.7. The receiving piezoelectric crystal transducer transforms the scattered pulses from the flaw into electrical pulses, using the fact that piezoelectric crystals are reciprocal in nature. These received signals are amplified in the receiver portion of the pulser-receiver and are then displayed on the oscilloscope as voltage vs time[103].

In the standard phased array process, time delays are applied to the elements in a phased array probe in order to generate a physical acoustic beam which is formed by the constructive interference of the various wavefronts. In reception the same time delays are applied to the signals which are received so as to put them in phase at the summing amplifier. The summed A-scan signal is then passed on to the computer for digitization and recording. Figure 2.7 shows the standard phased array process[104].

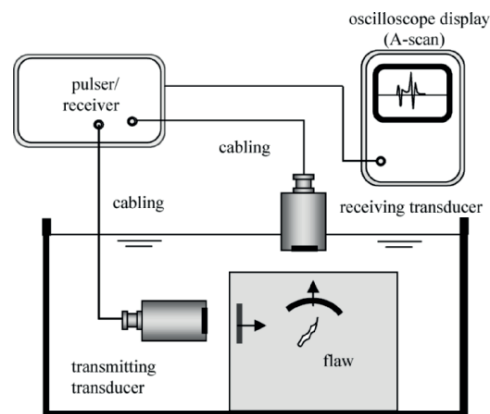


Figure 2.7: An ultrasonic testing setup [15]

A different approach for processing ultrasonic array data was traditionally based on firing parallel circuits that enable the staggered firing of transmitter elements to produce the wavefront. In this approach called Full Matrix Capture (FMC) they proposed collecting the time domain signals of every transmitter-receiver pair and storing them in a matrix. This approach is shown in Figure 2.8.

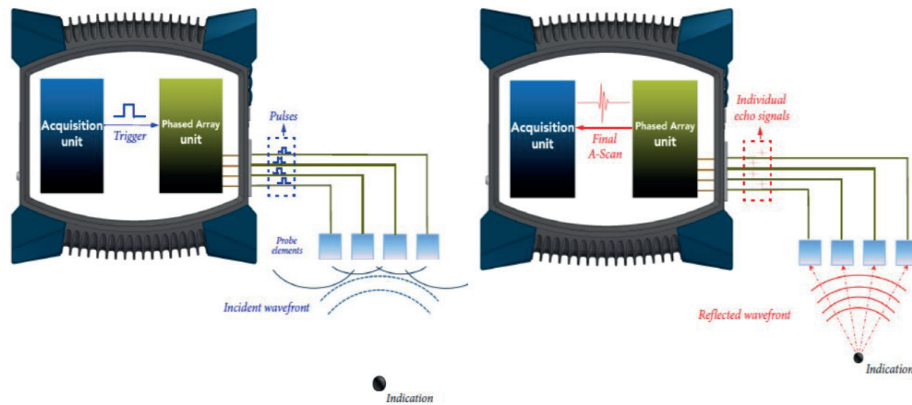


Figure 2.8. Transmitting and receiving signals using a Phased Array [104]

This type of acquisition allows the emulation of any beam forming or imaging to be performed as a post processing operation of the matrix. A further advantage of using full matrix capture is that advanced NDE processing such as time of flight diffraction etc, can be carried out on the same data (at a future date) without the need for further experimentation. The full matrix of data also contains the scattering matrix which represents the scattered field of a defect [84].

2.12. Research Question

The above literature study led to the identification of specific scientific gaps which this thesis hopes to bridge. It was seen that modelling and imaging the ultrasonic phased array NDE of isotropic materials is fairly straightforward whereas for anisotropic homogenous or layered structures, the inherent anisotropic nature of the structure and the layering affect the received signal. Hence we come to the main question of this thesis

How can I model and image the ultrasonic array testing of anisotropic homogenous or layered structures in a way which is accurate and computationally efficient?

The main question can then be answered by solving the following sub questions

1. **How can I model the beam propagation in anisotropic media from ultrasonic phased arrays in a computationally efficient, non-singular and accurate way at different steering angles?**

It was seen in Sections 2.2 and 2.5 that the beam models developed have certain drawbacks. The exact models based on the point source superposition technique suffers from a large computational cost as the transducer elements need to be composed of a number of point sources and this leads to solving of multiple integrals over the surface of the transducer. As a phased array consists of a number of such elements, the number of integrals that need to be evaluated become quite large hence leading to a computationally inefficient model. The distributed point source method suffers from the drawback that it is dependent on the Green's solution of the inspection medium, which for anisotropic medium is not a closed form expression and has to be evaluated numerically. The FEM/FDTD/BEM models require more computational power as the number of elements increase, as the frequency of the inspecting wave increases and also as the thickness of the material increases. It is important to have a beam model for transducer radiation into anisotropic structures, so as to realise the effect that anisotropy has on parameters such as on the focus point, focusing distance, steering angle, etc.

2. How can I develop a model to simulate the ultrasonic array signals while testing multi-layered composite materials?

The ultrasonic arrays signals obtained from the inspection of composite materials are not trivial due to the presence of multiple echos from the layer interfaces, the resonance of the plies, the attenuation due to scattering within the layers and the direction dependent velocity. The element size and pitch also influence the ultrasonic signals which are received by the elements. It was seen in section 2.7 that the finite size of the transducer needs to be taken into consideration so as to account for the diffraction caused by such a transducer. It is necessary to hence have a forward model which would hence simulate the response of a multi-layered anisotropic laminate when it is tested with an array of transducers of finite sizes.

3. How does the anisotropy and layup of the composite structure affect the imaging of defects and how can I develop a model to simulate the scattering from a defect

The detection of defects present in layered composite structures is also affected by the response of the structure to the ultrasonic wave passing through it. It is important for the forward model to incorporate the scattering from defects and the influence of the scattering on the output signals. Furthermore the application of imaging algorithms on the FMC is not straightforward as in the case of isotropic

materials due to the direction dependent velocity. For composite structures TFM which is a time domain imaging algorithm has been used by applying Backwall Reflection Method (BRM) to adjust for the anisotropic velocity.

The following chapters will be used to detail the methodology and the solutions to these research questions.

2.13 References

- [1] J. Krautkrämer and H. Krautkrämer, *Ultrasonic Testing of Materials*. Springer Science & Business Media, 2013.
- [2] J. Krautkrämer and H. Krautkrämer, *Ultrasonic Testing of Materials*. Springer Science & Business Media, 2013.
- [3] Z. Su and L. Ye, “Fundamentals and Analysis of Lamb Waves,” *Lect. Notes Appl. Comput. Mech.*, 2009, doi: 10.1007/978-1-84882-784-4_2.
- [4] J. A. Ogilvy and J. A. G. Temple, “Diffraction of elastic waves by cracks: application to time-of-flight inspection,” *Ultrasonics*, vol. 21, no. 6, pp. 259–269, 1983, doi: 10.1016/0041-624X(83)90058-6.
- [5] B. R. Tittmann, “Scattering of elastic waves from simple defects in solids, a review,” *Wave Motion*, vol. 5, no. 4, pp. 299–306, 1983, doi: 10.1016/0165-2125(83)90019-7.
- [6] R. B. Thompson and T. A. Gray, “A model relating ultrasonic scattering measurements through liquid–solid interfaces to unbounded medium scattering amplitudes,” *J. Acoust. Soc. Am.*, vol. 74, no. 4, pp. 1279–1290, 1983, doi: 10.1121/1.390045.
- [7] L. W. Schmerr, *Fundamentals of Ultrasonic Nondestructive Evaluation: A Modeling Approach (Springer Series in Measurement Science and Technology)*. 2016.
- [8] L. S. Jr, *Fundamentals of ultrasonic nondestructive evaluation: a modeling approach*. 2013.
- [9] M. Rudolph, “Ultrasonic beam models in anisotropic media,” 1999.
- [10] T. P. Lerch, L. W. Schmerr, and A. Sedov, “Ultrasonic beam models: An edge element approach,” *J. Acoust. Soc. Am.*, vol. 104, no. 3, pp. 1256–1265, 1998, doi: 10.1121/1.424334.
- [11] M. Spies, “Elastic waves in homogeneous and layered transversely isotropic media: Plane waves and Gaussian wave packets. A general approach,” *J. Acoust. Soc. Am.*, vol. 95, no. 4, p. 1748, 1994, doi: 10.1121/1.408694.
- [12] N. Gengembre and A. Lhémy, “Pencil method in elastodynamics: Application to ultrasonic field computation,” *Ultrasonics*, 2000, doi: 10.1016/S0041-624X(99)00068-2.
- [13] S. Deydier, N. Gengembre, P. Calmon, V. Mengeling, and O. Pétillon, “Ultrasonic field computation into multilayered composite materials using a homogenization method based on ray theory,” in *AIP Conference Proceedings*, 2005, doi: 10.1063/1.1916789.
- [14] S. Deydier, N. Leymarie, P. Calmon, and V. Mengeling, “Modeling of the ultrasonic propagation into carbon-fiber-reinforced epoxy composites, using a ray theory based homogenization method,” in *AIP Conference Proceedings*, 2006, doi: 10.1063/1.2184630.
- [15] S. Kolkoori, *Quantitative Evaluation of Ultrasonic Wave Propagation in Inhomogeneous Anisotropic Austenitic Welds using 3D Ray Tracing Method: Numerical and Experimental Validation*, vol. Doctoral t. 2014.
- [16] T. Yanagita, T. Kundu, and D. Placko, “Ultrasonic field modeling by distributed point source method for different transducer boundary conditions,” *J. Acoust. Soc. Am.*, 2009,

- doi: 10.1121/1.3203307.
- [17] R. Ahmad, T. Kundu, and D. Placko, "Modeling of phased array transducers," *J. Acoust. Soc. Am.*, vol. 117, no. 4, pp. 1762–1776, Apr. 2005, doi: 10.1121/1.1835506.
- [18] S. Banerjee and T. Kundu, "Ultrasonic field modeling in plates immersed in fluid," *Int. J. Solids Struct.*, 2007, doi: 10.1016/j.ijsolstr.2007.02.011.
- [19] D. Placko and T. Kundu, "Modeling of ultrasonic field by distributed point source method," in *Ultrasonic Nondestructive Evaluation: Engineering and Biological Material Characterization*, 2003.
- [20] D. Placko and T. Kundu, *DPSM for Modeling Engineering Problems*. 2006.
- [21] S. Fooladi and T. Kundu, "Distributed point source modeling of the scattering of elastic waves by a circular cavity in an anisotropic half-space," *Ultrasonics*, 2019, doi: 10.1016/j.ultras.2018.09.002.
- [22] O. Zienkiewicz, R. Taylor, and J. Z. Zhu, *The Finite Element Method: its Basis and Fundamentals: Seventh Edition*. 2013.
- [23] A. Van Pamel, C. R. Brett, and M. J. S. Lowe, "A methodology for evaluating detection performance of ultrasonic array imaging algorithms for coarse-grained materials," *IEEE Trans. Ultrason. Ferroelectr. Freq. Control*, vol. 61, no. 12, pp. 2042–53, Dec. 2014, doi: 10.1109/TUFFC.2014.006429.
- [24] A. Velichko and P. D. Wilcox, "A generalized approach for efficient finite element modeling of elastodynamic scattering in two and three dimensions," *J. Acoust. Soc. Am.*, vol. 128, no. 3, pp. 1004–14, 2010, doi: 10.1121/1.3467775.
- [25] W. Lord, R. Ludwig, and Z. You, "Developments in ultrasonic modeling with finite element analysis," *J. Nondestruct. Eval.*, vol. 9, no. 2–3, pp. 129–143, 1990, doi: 10.1007/BF00566389.
- [26] Z. You, M. Lusk, R. Ludwig, and W. Lord, "Numerical Simulation of Ultrasonic Wave Propagation in Anisotropic and Attenuative Solid Materials," *IEEE Trans. Ultrason. Ferroelectr. Freq. Control*, vol. 38, no. 5, pp. 436–445, 1991, doi: 10.1109/58.84288.
- [27] A. Minachi, Z. You, R. Bruce Thompson, and W. Lord, "Predictions of the Gauss-Hermite beam model and finite element method for ultrasonic propagation through anisotropic stainless steel," *IEEE Trans. Ultrason. Ferroelectr. Freq. Control*, vol. 40, no. 4, pp. 338–346, 1993, doi: 10.1109/58.251282.
- [28] X. Zhang, D. Zhang, Q. Chen, and Y. Yang, "Second-order scalar wave field modeling with a first-order perfectly matched layer," *Solid Earth*, vol. 9, no. 6, pp. 1277–1298, Nov. 2018, doi: 10.5194/se-9-1277-2018.
- [29] S. Paunekar and S. Gopalakrishnan, "Spectral finite element method for studying the wave response on using sh modes in adhesively bonded metallic joints," *Struct. Heal. Monit. 2017 Real-Time Mater. State Aware. Data-Driven Saf. Assur. - Proc. 11th Int. Work. Struct. Heal. Monit. IWSHM 2017*, vol. 1, pp. 1787–1794, 2017, doi: 10.12783/shm2017/14060.
- [30] A. Chakraborty and S. Gopalakrishnan, "A spectral finite element model for wave propagation analysis in laminated composite plate," *J. Vib. Acoust. Trans. ASME*, 2006, doi: 10.1115/1.2203338.
- [31] D. Komatitsch, R. Martin, J. Tromp, M. A. Taylor, and B. A. Wingate, "Wave propagation in 2-D elastic media using a spectral element method with triangles and quadrangles," *J. Comput. Acoust.*, 2001, doi: 10.1142/S0218396X01000796.
- [32] D. Komatitsch, C. Barnes, and J. Tromp, "Simulation of anisotropic wave propagation based upon a spectral element method," *Geophysics*, 2000, doi: 10.1190/1.1444816.
- [33] R. Sridhar, A. Chakraborty, and S. Gopalakrishnan, "Wave propagation analysis in

- anisotropic and inhomogeneous uncracked and cracked structures using pseudospectral finite element method,” *Int. J. Solids Struct.*, 2006, doi: 10.1016/j.ijsolstr.2005.10.005.
- [34] Z. P. Chi, Z. P. Zhao, and N. Li, “The modeling of piezoelectric transducers using the FDTD method,” *Proc. 7th Int. Conf. Mach. Learn. Cybern. ICMLC*, vol. 4, no. July, pp. 2154–2159, 2008, doi: 10.1109/ICMLC.2008.4620762.
- [35] N. Dominguez and F. Reverdy, “Simulation of Ultrasonic Testing of Composite Structures 2 . A model for composite ultrasonic testing applications,” *11th Eur. Conf. non-destructive Test. ECNDT 2014*, 2014, [Online]. Available: http://www.ndt.net/events/ECNDT2014/app/content/Paper/344_Dominguez.pdf.
- [36] D. K. Wilson and L. Liu, “Finite-Difference, Time-Domain Simulation of Sound Propagation in a Dynamic Atmosphere,” no. ERDC/CRREL TR-04-12, p. 63, 2004.
- [37] E. G. Bazulin, D. A. Kononov, and M. S. Sadykov, “Finite-Difference Time Domain Method. Calculating Echo Signals in Homogeneous Isotropic Materials,” *Russ. J. Nondestruct. Test.*, vol. 54, no. 7, pp. 469–478, 2018, doi: 10.1134/S1061830918070021.
- [38] J. T. Welter, J. N. Wertz, J. C. Aldrin, V. Kramb, and D. Zainey, “Model-driven optimization of oblique angle ultrasonic inspection parameters for delamination characterization,” in *AIP Conference Proceedings*, 2018, doi: 10.1063/1.5031600.
- [39] M. Spies and W. Jager, “Synthetic aperture focusing for defect reconstruction in anisotropic media,” *Ultrasonics*, vol. 41, no. 2, pp. 125–131, 2003, doi: 10.1016/S0041-624X(02)00407-9.
- [40] R. Thompson and E. Lopes, “The effects of focusing and refraction on Gaussian ultrasonic beams,” *J. Nondestruct. Eval.*, vol. 4, no. 2, 1984, [Online]. Available: <http://link.springer.com/article/10.1007/BF00566401>.
- [41] J. J. Wen and M. A. Breazeale, “A diffraction beam field expressed as the superposition of Gaussian beams,” *J. Acoust. Soc. Am.*, vol. 83, no. 5, pp. 1752–1756, 1988, doi: 10.1121/1.396508.
- [42] M. Spies, “Analytical methods for modeling of ultrasonic nondestructive testing of anisotropic media,” *Ultrasonics*, vol. 42, no. 1–9, pp. 213–9, 2004, doi: 10.1016/j.ultras.2004.01.012.
- [43] R. Huang, “Ultrasonic modeling for complex geometries and materials,” *Iowa State Univ.*, 2006, [Online]. Available: <http://adsabs.harvard.edu/abs/2006PhDT.....54H>.
- [44] J. W. Goodman, “Introduction to Fourier Optics, 2nd ed.,” *Quantum Semiclassical Opt. J. Eur. Opt. Soc. Part B*, vol. 8, no. 5, p. 491, 1996, doi: 10.1088/1355-5111/8/5/014.
- [45] D. Belgroune, J. F. De Belleval, and H. Djelouah, “Modelling of the ultrasonic field by the angular spectrum method in presence of interface,” in *Ultrasonics*, 2002, vol. 40, no. 1–8, pp. 297–302, doi: 10.1016/S0041-624X(02)00110-5.
- [46] M. E. Schafer and P. A. Lewin, “Transducer characterization using the angular spectrum method,” *J. Acoust. Soc. Am.*, vol. 85, no. 5, pp. 2202–2214, 1989, doi: 10.1121/1.397869.
- [47] A. Van Pamel, C. R. Brett, P. Huthwaite, and M. J. S. Lowe, “Finite element modelling of elastic wave scattering within a polycrystalline material in two and three dimensions,” *J. Acoust. Soc. Am.*, 2015, doi: 10.1121/1.4931445.
- [48] C. Miki, K. Ikeda, K. Tateishi, and M. Takahashi, “Numerical simulation of ultrasonic pulse-echo inspection,” *Struct. Eng. Eng.*, 1993.
- [49] T. Ashizawa, Y. Mizutani, N. Toyama, A. Todoroki, and Y. Suzuki, “Numerical analysis and experimental observation of ultrasonic wave propagation in CFRP with curved fibers,” *Compos. Struct.*, 2018, doi: 10.1016/j.compstruct.2018.03.089.
- [50] J. B. Cole, R. A. Krutar, S. K. Numrich, and D. B. Creamer, “Finite-difference time-domain simulations of wave propagation and scattering as a research and educational

- tool,” *Comput. Phys.*, 1995, doi: 10.1063/1.168528.
- [51] A. Saez and J. Dominguez, “Boundary Element Analysis of Wave Scattering in Transversely Isotropic Solids,” in *Advances in Boundary Element Methods*, 2009, doi: 10.4203/ccp.44.1.5.
- [52] A. L. Lopez-Sanchez, H. J. Kim, L. W. Schmerr, and T. A. Gray, “Modeling the response of ultrasonic reference reflectors,” *Res. Nondestruct. Eval.*, vol. 17, no. 2, pp. 49–69, 2006, doi: 10.1080/09349840600689459.
- [53] A. L. Lopez-Sanchez, H. J. Kim, L. W. Schmerr, and A. Sedov, “Measurement models and scattering models for predicting the ultrasonic pulse-echo response from side-drilled holes,” *J. Nondestruct. Eval.*, vol. 24, no. 3, pp. 83–96, 2005, doi: 10.1007/s10921-005-7658-4.
- [54] L. W. Schmerr and A. Sedov, “Ultrasonic Crack Characterization: a Constrained Inversion Algorithm,” *Rev. Prog. Quant. Nondestruct. Eval.*, vol. 5 A, no. 1, pp. 367–374, 1986, doi: 10.1007/978-1-4615-7763-8_37.
- [55] M. Darmon, V. Dorval, A. Kamta Djakou, L. Fradkin, and S. Chatillon, “A system model for ultrasonic NDT based on the Physical Theory of Diffraction (PTD),” *Ultrasonics*, vol. 64, pp. 115–127, 2016, doi: 10.1016/j.ultras.2015.08.006.
- [56] V. Dorval, M. Darmon, S. Chatillon, and L. Fradkin, “Simulation of the UT inspection of planar defects using a generic GTD-Kirchhoff approach,” in *AIP Conference Proceedings*, 2015, doi: 10.1063/1.4914798.
- [57] A. Lopez-Sanchez, “Ultrasonic system models and measurements,” *Iowa State Univ.*, 2005, [Online]. Available: <http://adsabs.harvard.edu/abs/2005PhDT.....128L>.
- [58] P. Cawley and R. D. Adams, “Defect types and non-destructive testing techniques for composites and bonded joints,” *Mater. Sci. Technol.*, vol. 5, no. 5, pp. 413–425, 1989, doi: 10.1179/026708389790222366.
- [59] L. W. Schmerr, *Fundamentals of Ultrasonic Phased Arrays*, vol. 215, no. May 2003. Cham: Springer International Publishing, 2015.
- [60] S. Stergiopoulos, *Advanced signal processing handbook: Theory and implementation for radar, sonar, and medical imaging real-time systems*. 2000.
- [61] R. J. Mailloux, “Phased array theory and technology,” *Proc. IEEE*, vol. 70, no. 3, pp. 246–291, 1982, doi: 10.1109/PROC.1982.12285.
- [62] O. T. Von Ramm and S. W. Smith, “Beam Steering with Linear Arrays,” *IEEE Trans. Biomed. Eng.*, vol. BME-30, no. 8, pp. 438–452, 1983, doi: 10.1109/TBME.1983.325149.
- [63] P. D. Wilcox, J. Zhang, and B. W. Drinkwater, “Defect characterization using ultrasonic arrays,” *Proc. SPIE*, vol. 6935, pp. 69350X–69350X–12, 2008, doi: 10.1117/12.776235.
- [64] L. Azar, Y. Shi, and S. C. Wooh, “Beam focusing behavior of linear phased arrays,” *NDT E Int.*, vol. 33, no. 3, pp. 189–198, 2000, doi: 10.1016/S0963-8695(99)00043-2.
- [65] H. J. Kim, L. W. Schmerr, and A. Sedov, “Generation of the basis sets for multi-Gaussian ultrasonic beam models,” in *AIP Conference Proceedings*, 2005, vol. 760, pp. 978–985, doi: 10.1063/1.1916779.
- [66] J. S. Park, S. J. Song, and H. J. Kim, “Calculation of Radiation Beam Field from Phased Array Ultrasonic Transducers Using Expanded Multi-Gaussian Beam Model,” *Solid State Phenom.*, vol. 110, pp. 163–168, 2006, doi: 10.4028/www.scientific.net/SSP.110.163.
- [67] R. Huang, L. W. Schmerr, and A. Sedov, “Modeling the radiation of ultrasonic phased-array transducers with Gaussian beams,” *IEEE Trans. Ultrason. Ferroelectr. Freq. Control*, vol. 55, no. 12, pp. 2692–2702, 2008, doi: 10.1109/TUFFC.2008.984.
- [68] B. P. Newberry and R. Bruce Thompson, “A paraxial theory for the propagation of ultrasonic beams in anisotropic solids,” *J. Acoust. Soc. Am.*, vol. 85, no. 6, pp. 2290–2300,

- 1989, doi: 10.1121/1.397775.
- [69] O. I.-2nd Isaac M. Daniel, "Engineering mechanics of composite materials," *Materials & Design*. 2006.
- [70] S. I. Rokhlin, D. E. Chimenti, and P. B. Nagy, *Physical ultrasonics of composites*. Oxford University Press, 2011.
- [71] D. Royer, *Elastic waves in solids / 1, Free and guided propagation*. Springer, 2000.
- [72] B. Hosten, M. Deschamps, and B. R. Tittmann, "Inhomogeneous wave generation and propagation in lossy anisotropic solids. Application to the characterization of viscoelastic composite materials," *J. Acoust. Soc. Am.*, vol. 82, no. 5, p. 1763, 1987, doi: 10.1121/1.395170.
- [73] M. Castaing, B. Hosten, and T. Kundu, "Inversion of ultrasonic, plane-wave transmission data in composite plates to infer viscoelastic material properties," *NDT E Int.*, vol. 33, no. 6, pp. 377–392, 2000, doi: 10.1016/S0963-8695(00)00004-9.
- [74] A. K. Kaw, *Mechanics of composite materials, second edition*. 2005.
- [75] H. Altenbach, J. Altenbach, and W. Kissing, *Mechanics of Composite Structural Elements*. Berlin, Heidelberg: Springer Berlin Heidelberg, 2004.
- [76] J. W. Littles, L. J. Jacobs, and A.-H. Zureick, "Single-sided ultrasonic technique to characterize thick FRP composites," *J. Nondestruct. Eval.*, vol. 17, no. 4, pp. 223–230, Dec. 1998, doi: 10.1007/BF02447050.
- [77] A. H. Nayfeh, "The general problem of elastic wave propagation in multilayered anisotropic media," *J. Acoust. Soc. Am.*, 1991, doi: 10.1121/1.400988.
- [78] K. Jezzine, D. Ségur, R. Ecault, and N. Dominguez, "Simulation of ultrasonic inspections of composite structures in the CIVA software platform," *19th World Conf. Non-Destructive Test. 2016*, pp. 1–8, 2016, [Online]. Available: <http://creativecommons.org/licenses/by-nd/3.0/>.
- [79] L. Knopoff, "A Matrix Method for Elastic Wave Problems," *Bull. Seismol. Soc. Am.*, 1964.
- [80] N. A. Haskell, "The dispersion of surface waves on multilayered media*," *Bull. Seismol. Soc. Am.*, vol. 43, no. 1, pp. 17–34, Jan. 1953.
- [81] W. T. Thomson, "Transmission of elastic waves through a stratified solid medium," *J. Appl. Phys.*, 1950, doi: 10.1063/1.1699629.
- [82] S. I. Rokhlin and L. Wang, "Ultrasonic waves in layered anisotropic media: Characterization of multidirectional composites," *Int. J. Solids Struct.*, 2002, doi: 10.1016/S0020-7683(02)00500-0.
- [83] L. Wang and S. I. Rokhlin, "Ultrasonic wave interaction with multidirectional composites: Modeling and experiment," *J. Acoust. Soc. Am.*, vol. 114, no. 5, p. 2582, 2003, doi: 10.1121/1.1616920.
- [84] C. Holmes, B. W. Drinkwater, and P. D. Wilcox, "Post-processing of the full matrix of ultrasonic transmit–receive array data for non-destructive evaluation," *NDT E Int.*, vol. 38, no. 8, pp. 701–711, 2005, doi: 10.1016/j.ndteint.2005.04.002.
- [85] F. Lingvall, "Time-domain Reconstruction Methods for Ultrasonic Array Imaging Dissertation for the degree of Doctor of Philosophy in Electrical Engineering with specialization in Signal Processing," 2004.
- [86] P. D. Wilcox, "Ultrasonic arrays in NDE: Beyond the B-scan," *Rev. Prog. Quant. Nondestruct. Eval. Vol. 32*, vol. 1511, no. 1, pp. 33–50, 2013, doi: 10.1063/1.4789029.
- [87] J. Zhang, B. W. Drinkwater, and P. D. Wilcox, "Comparison of ultrasonic array imaging algorithms for nondestructive evaluation.," *IEEE Trans. Ultrason. Ferroelectr. Freq. Control*, vol. 60, no. 8, pp. 1732–45, 2013, doi: 10.1109/TUFFC.2013.2754.

- [88] L. Moreau, B. W. Drinkwater, and P. D. Wilcox, "Ultrasonic imaging algorithms with limited transmission cycles for rapid nondestructive evaluation.," *IEEE Trans. Ultrason. Ferroelectr. Freq. Control*, vol. 56, no. 9, pp. 1932–44, 2009, doi: 10.1109/TUFFC.2009.1269.
- [89] A. Volker, "Plane wave imaging using phased array," *Rev. Prog. Quant. NDE*, vol. 1581, pp. 124–131, 2014, doi: 10.1063/1.4864811.
- [90] A. J. Hunter, B. W. Drinkwater, and P. D. Wilcox, "The wavenumber algorithm for full-matrix imaging using an ultrasonic array," *IEEE Trans. Ultrason. Ferroelectr. Freq. Control*, vol. 55, no. 11, pp. 2450–2462, 2008, doi: 10.1109/TUFFC.952.
- [91] C. Li, D. Pain, P. D. Wilcox, and B. W. Drinkwater, "Imaging composite material using ultrasonic arrays," *NDT E Int.*, vol. 53, pp. 8–17, 2013, doi: 10.1016/j.ndteint.2012.07.006.
- [92] D. Pain and B. W. Drinkwater, "Detection of fibre waviness using ultrasonic array scattering data," *J. Nondestruct. Eval.*, vol. 32, no. 3, pp. 215–227, 2013, doi: 10.1007/s10921-013-0174-z.
- [93] Y. Humeida, V. J. Pinfield, R. E. Challis, P. D. Wilcox, and C. Li, "Simulation of ultrasonic array imaging of composite materials with defects," *IEEE Trans. Ultrason. Ferroelectr. Freq. Control*, vol. 60, no. 9, pp. 1935–1948, 2013, doi: 10.1109/TUFFC.2013.2778.
- [94] J. N. Potter, A. J. Croxford, and P. D. Wilcox, "Nonlinear ultrasonic phased array imaging," *Phys. Rev. Lett.*, 2014, doi: 10.1103/PhysRevLett.113.144301.
- [95] E. Barbieri and M. Meo, "Time reversal DORT method applied to nonlinear elastic wave scattering," *Wave Motion*, 2010, doi: 10.1016/j.wavemoti.2010.01.004.
- [96] G. P. Malfense Fierro and M. Meo, "Nonlinear imaging (NIM) of flaws in a complex composite stiffened panel using a constructive nonlinear array (CNA) technique," *Ultrasonics*, 2017, doi: 10.1016/j.ultras.2016.09.018.
- [97] G. W. Postma, "WAVE PROPAGATION IN A STRATIFIED MEDIUM," *GEOPHYSICS*, 1955, doi: 10.1190/1.1438187.
- [98] E. Behrens, "Sound Propagation in Lamellar Composite Materials and Averaged Elastic Constants," *J. Acoust. Soc. Am.*, 1967, doi: 10.1121/1.1910587.
- [99] C. T. Sun, J. D. Achenbach, and G. Herrmann, "Continuum theory for a laminated medium," *J. Appl. Mech. Trans. ASME*, 1964, doi: 10.1115/1.3601237.
- [100] R. B. Enie and R. R. Rizzo, "Three-Dimensional Laminate Moduli," *J. Compos. Mater.*, vol. 4, no. 1, pp. 150–154, 1970, doi: 10.1177/002199837000400118.
- [101] A. K. Roy and S. W. Tsai, "Three-dimensional effective moduli of orthotropic and symmetric laminates," *J. Appl. Mech. Trans. ASME*, 1992, doi: 10.1115/1.2899462.
- [102] H. J. Chen and S. W. Tsai, "Three-dimensional effective moduli of symmetric laminates," *J. Compos. Mater.*, 1996, doi: 10.1177/002199839603000803.
- [103] L. W. Schmerr and J.-S. Song, *Ultrasonic Nondestructive Evaluation Systems: Models and Measurements*. 2007.
- [104] P. Tremblay and D. Richard, "Development and Validation of a Full Matrix Capture Solution," *NDT.net*, pp. 457–466, 2012.

3

Methodology

The methodology applied in this thesis revolves around answering each sub question separately. In this chapter I provide the methodology adopted to answer each sub question and the justification behind the choices which are made.

3.1 Methodology followed for each sub question

In this section I describe the methodology for each sub question.

1. How can I model the beam propagation in anisotropic media from ultrasonic phased arrays in a computationally efficient, non-singular and accurate way at different steering angles?

Phased arrays are commonly used in two configurations, using all the elements to steer the beam and full matrix capture. In the beam steering configuration, while testing structures, beam steering takes place and hence it is important to model the beam emitted from a phased array which undergoes beam steering. It is important to understand the effects of anisotropy on the steering of a beam emitted from a phased array in such materials. Hence we require a beam model which incorporates the ultrasonic beam emitted from phased array transducers, propagation in homogeneous anisotropic media and enables beam steering.

Models based on the paraxial approximation such as the Multi Gaussian beam method have been shown to be computationally efficient as they require the superposition of a small number of Gaussian beams [1]. Such beam models are also non-singular when interacting with curved interfaces [2]. This makes the MGBs a natural choice for developing a computationally inexpensive model for beam propagation in homogeneous anisotropic media. In this thesis, a model is developed for beam propagation from a phased array through homogeneous anisotropic media, which enables beam steering and is accurate when the beam is steered above the paraxial limit. In chapter 4 it will be shown how the MGB model for radiation from phased arrays into isotropic media can be modified for anisotropic media by including the slowness surface curvatures and a linear phasing will be applied to the elements to enable steering above the paraxial limit. The developed model is also validated with a numerical model and comparisons between the computational efficiency are also made.

2. How can I develop a model to simulate the ultrasonic array signals while testing multi-layered composite materials?

The beam model developed in Chapter 4, though computationally efficient for homogeneous anisotropic media, when applied for multilayered anisotropic structures becomes computationally expensive. The cost of computation increases due to the fact that in thin plies such as those used in composite laminates, multiple

reflections take place in the layers which cause overlapping echos in the received signal. To simulate these signals the beam has to be tracked through every layer and every reflection which becomes computationally expensive and is a complicated combinatorics problem [3]. While simulating the received signals of such structures, the interest lies with the final output signal and the effect of layering on it. The stiffness matrix method has been used to calculate the reflection and transmission coefficients at the top and bottom of a layered anisotropic material respectively.

The received signals depend on the beam emitted from the transducer, response of the layered structure and the effect of inherent system variables such as input voltage, cabling, etc.

In Chapter 5, I develop a model which takes into account the above by combining the multi Gaussian beam model for a rectangular transducer with the reflection coefficients generated using the stiffness matrix method. The stiffness matrix method is chosen as it is stable at high frequencies and low layer thicknesses [4]. To generate the full matrix signals as accurately as those in the real world scenario, I chose to adopt an experimental system efficiency factor which is described in chapter 5 [5]. The Angular spectrum method is then used to combine the MGBs, stiffness matrix approach as the stiffness matrix approach is applicable only to plane waves and the system efficiency factor to generate FMC signals.

3. How does the anisotropy and layup of the composite structure affect the imaging of defects?

To answer this question we would need the scattering of the defect embedded in such a structure and to combine it with the response of the laminated structure. The model developed in Chapter 5 considers a laminate surrounded by a semi-infinite medium. In Chapter 6 I propose a method to calculate the response of a laminate surrounded by a semi-infinite anisotropic medium. This is done to model the scattering from the defect, as it is assumed to be embedded in a semi-infinite anisotropic medium with the elastic properties of an effective homogeneous anisotropic material bounded by the layers of the laminate above it. The defect chosen is a side drilled hole as it is commonly used as a reference defect in ultrasonic testing. The scattering of the defect is calculated using exact solutions and is combined with the response of the layers above the defect so as to simulate the scattering signal from the defect. Simulation of FMC signals is carried out and the TFM imaging algorithm, which is the gold standard in imaging algorithms for FMC is used to image the SDH and the laminate. The TFM is corrected for anisotropic velocity by using model generated group velocity. Experimental and

model generated TFM images are compared qualitatively and quantitatively by using SNR values of the image.

Hence it can be seen that in this thesis I will develop and validate a computationally inexpensive model to simulate the signals from homogeneous anisotropic and layered structures. The beam model developed in Chapter 4 provides an insight into various parameters which affect the beam propagation in anisotropic media and the answering of questions 2 and 3 leads to the development of a model to simulate the output signals from a layered media and the scattering from defects embedded in such a media. The answers to these three questions provide the answer for the main research question by providing models which are computationally inexpensive, accurate, and are validated experimentally and numerically.

3.2 References

- [1] M. Rudolph, "Ultrasonic beam models in anisotropic media," *Iowa State Univ.*, p. 253, 1999.
- [2] R. Huang, "Ultrasonic modeling for complex geometries and materials," 2006.
- [3] F. Hron, B. T. May, J. D. Covey, and P. F. Daley, "Synthetic seismic sections for acoustic, elastic, anisotropic, and vertically inhomogeneous layered media.," *Geophysics*, vol. 51, no. 3, pp. 710–735, 1986, doi: 10.1190/1.1442124.
- [4] S. I. Rokhlin and L. Wang, "Ultrasonic waves in layered anisotropic media: Characterization of multidirectional composites," *Int. J. Solids Struct.*, vol. 39, no. 21–22, pp. 5529–5545, 2002, doi: 10.1016/S0020-7683(02)00500-0.
- [5] L. W. Schmerr, *Fundamentals of Ultrasonic Nondestructive Evaluation A Modeling Approach Second Edition*. 2016.

4

Modelling Of Phased Array Radiation Through Anisotropic Media Using Multi Gaussian Beams

Abstract

In this chapter I develop a Multi Gaussian based beam model to describe the propagation of a beam from a phased array into an homogeneous anisotropic medium. First an Ordinary Multi Gaussian Beam model is developed (OMGB) which is shown to lose accuracy once the beam is steered above the paraxial limit. Next a Linearly Phased Multi Gaussian beam model is developed which modifies the OMGB to maintain accuracy above the paraxial limit. Austentic steel is chosen as the material through which the beam propagation at different steering angles is modeled. The results of the developed models are then validated against a Finite Element Model (FEM). A comparison of parameters such as amplitude error, computational time between the developed and FEM model is also presented.

Adapted from : C. Anand, S. Delrue, H. Jeong, S. Shroff, R.Groves, R.Benedictus, Simulation of Ultrasonic Beam Propagation From Phased Arrays in Anisotropic Media Using Linearly Phased Multi-Gaussian Beams, IEEE TUFFC 2020; 106

4.1 Introduction

In Chapter 2, it was seen that there are a number of beam models which have been formulated to describe the propagation of a beam emitted by single or array transducers in isotropic and anisotropic media. These beam models suffer from either mathematical complexity, computational efficiency or are singular when propagating through curved interfaces. In this chapter I will address research sub question 1 introduced in chapter 2. The question pertains to the development of a beam model in anisotropic media which is required to be computationally inexpensive, non-singular when interacting with curved surfaces and accounts for beam steering at different angles. Paraxial models are computationally inexpensive as they are based on the assumption of paraxial propagation of rays. The Multi Gaussian beam (MGB) model is an efficient paraxial beam model which is non-singular when interacting with curved interfaces and is computationally inexpensive as it requires only a small number of beams to model the radiation from a transducer, hence is suitable for the requirements of question 1. Therefore I address question 1 by developing a paraxial model based on multi Gaussian beams to simulate the beam propagation from a phased array into anisotropic materials. Austenitic steel has been chosen as the material through which the beam propagation is modeled due to its inherent anisotropy and usage in components of aircraft landing gear [1]. The next section introduces the background theory for the propagation of a beam from a single element transducer into an anisotropic media [2].

4.2 Background theory of the paraxial MGB model for beam propagation in anisotropic media

This section describes the preliminary theory of Gaussian beam propagation in anisotropic media.

Consider a single circular transducer of diameter $2a$ with its emitting surface lying in the x_1 - x_2 plane and its normal pointing in the x_3 direction. The x_3' axis is taken along the group velocity direction (i.e. at an angle θ with respect to the normal direction x_3) and the x_1' - x_3' plane is taken as the plane of incidence as shown in Fig. 4.1.

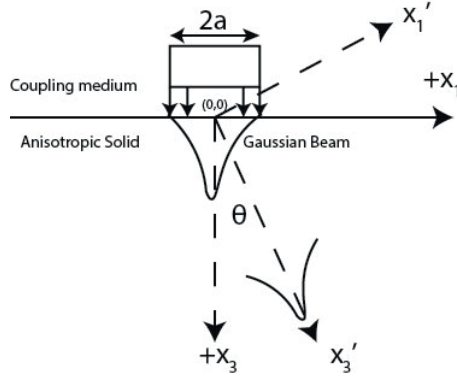


Fig. 4.1: Gaussian beam radiating from a transducer at an angle θ (group velocity direction)

Wen and Breazeale determined that only ten Gaussian beam coefficients A_n and B_n were required to represent an ultrasonic beam. These coefficients were given in their seminal paper in 1988 [3]. Using these coefficients, the velocity amplitude v and the phase \mathbf{M} of a Gaussian beam in a solid can be described by the solution of the paraxial equation [2]

$$\mathbf{v} = v_0 \sum_{n=1}^{10} A_n \frac{\sqrt{\det[\mathbf{M}(x_3')]} }{\sqrt{\det[\mathbf{M}(0)]}} \mathbf{d} \exp \left[i\omega \left(\frac{x_3'}{u_p} + \frac{1}{2} \mathbf{X}^T \mathbf{M}(x_3') \mathbf{X} \right) \right] \quad (4.2)$$

With,

$$\mathbf{M}(0)_n = \frac{2iB_n}{\omega a^2} \mathbf{I}, \quad \mathbf{M}(x_3') = \mathbf{M}(0) \left[\mathbf{I} + \frac{x_3'}{c_p} \mathbf{S}_p \mathbf{M}(0) \right]^{-1} \quad (4.3)$$

And

$$\mathbf{S}_p = c_p \begin{bmatrix} (c_p - 2C) & -D \\ -D & (c_p - 2E) \end{bmatrix} \quad (4.4)$$

In Eq. (4.1) and Eq. (4.2), v_0 and $\mathbf{M}(0)$ are the initial velocity and phase amplitudes at the transducer face, $\mathbf{X}(x_1', x_2', x_3')$ are the coordinates in the group velocity direction, \mathbf{d} is the polarization vector, \mathbf{I} is the identity matrix, ω is the angular frequency, the magnitudes of the phase velocity and group velocity are denoted by c_p and u_p respectively and A_n , B_n are the gaussian beam coefficients. The parameters C , D and E in Eq. (4.2) and Eq. (4.3) are the slowness surface curvatures which are measured in the slowness coordinates. They determine the rate of divergence or convergence of the beam due to diffraction. These parameters

are obtained by expanding the x_3' component of the slowness vector s_0 using a Taylor series expansion as follows

$$s_{x_3'} = s_0 + As_{x_1'} + Bs_{x_2'} + \left(C - \frac{I}{2s_0} \right) s_{x_1'}^2 + Ds_{x_1'}s_{x_2'} + \left(E - \frac{I}{2s_0} \right) s_{x_2'}^2 \quad (4.5)$$

Where $s_{x_1'}$, $s_{x_2'}$ and $s_{x_3'}$ are the slowness vector components and s_0 is the slowness value. Expansion of the slowness vector also gives the parameters A and B which are related to the deviation or skew of the group velocity from the slowness direction. For an isotropic material $A = B = C = D = E = 0$.

In practical applications, transducer arrays mainly consist of rectangular shaped elements of a fixed length and width. Hence in the next section Eq. (4.1) is modified for transducers arrays with rectangular shaped elements.

4.3 Development of Ordinary and linearly phased MGB models for phased array beam propagation in anisotropic media

4.3.1 Development of the Ordinary MGB (OMGB) model for phased array

The first model developed in this chapter to calculate the ultrasonic beam propagation from an array of transducers in anisotropic media is based on the expanded multi-Gaussian beam model developed for an array of rectangular transducers in isotropic media [4], [5]. Firstly, this expanded multi Gaussian beam model for element j , developed for isotropic media is shown in Eq. (4.5). Eq. (4.1) has been developed by considering a one dimensional circular transducer hence only one set of A coefficients are required, whereas for rectangular transducers, the transducers considered are 2-dimensional having length and width, hence A_n and A_m are required to describe the Gaussian beam radiating from a rectangular transducer.

$$\mathbf{v}_j = \mathbf{d} \exp \left(i\omega \frac{x_3}{c_p} \right) \sum_{m=1}^{10} \sum_{n=1}^{10} v_0 \frac{A_n A_m}{\sqrt{1 + c_p x_3 [\mathbf{M}_{mn}(0)]_{11}} \sqrt{1 + c_p x_3 [\mathbf{M}_{mn}(0)]_{22}}} \times \exp \left[\frac{1}{2} \mathbf{X}^T \mathbf{M}_{mn}(x_3) \mathbf{X} \right] \quad (4.6)$$

Where

$$[\mathbf{M}_{mn}(0)]_{11} = \frac{iB_m}{D_1}, [\mathbf{M}_{mn}(0)]_{22} = \frac{iB_n}{D_2} \quad (4.7)$$

$$D_1 = \frac{ka_1^2}{2}, D_2 = \frac{ka_2^2}{2}$$

$$[\mathbf{M}_{mn}(x_3)]_{11} = \frac{[\mathbf{M}_{mn}(0)]_{11}}{1 + c_p x_3 [\mathbf{M}_{mn}(0)]_{11}}$$

$$[\mathbf{M}_{mn}(x_3)]_{22} = \frac{[\mathbf{M}_{mn}(0)]_{22}}{1 + c_p x_3 [\mathbf{M}_{mn}(0)]_{22}} \quad (4.8)$$

$$[\mathbf{M}_{mn}(x_3)]_{12} = [\mathbf{M}_{mn}(x_3)]_{21} = 0$$

The subscripts in Eq. (4.8) are the indices of matrix elements. For isotropic materials the group velocity and the phase velocity are equal hence in Eq. (4.5) the phase velocity c_p is used. k is the wave number and a_1 and a_2 are the width and length of the rectangular transducer respectively. A_n, A_m, B_n, B_m are the Wen and Breazzle coefficients as stated before.

Now in this chapter the OMBG for anisotropic media is developed by modifying Eq. (4.5) using parameters from Eq. (4.3) and by using some simple linear algebra and matrix rearrangement.

The OMGB model for ultrasonic beams from an array into anisotropic media is formulated as shown in Eq. (4.8). The angle of incidence due to steering is in the group velocity direction, hence the rotated coordinates are now $\mathbf{X}'(x_1', x_2', x_3')$

$$\mathbf{v}_j = \mathbf{d} \exp\left(i\omega \frac{x_3'}{u_p}\right) \sum_{m=1}^{10} \sum_{n=1}^{10} v_0 A_n A_m \frac{\sqrt{\det[\mathbf{M}_{mn}(x_3')]} }{\sqrt{\det[\mathbf{M}_{mn}(0)]}} \times \exp\left[\frac{1}{2} \mathbf{X}'^T \mathbf{M}_{mn}(x_3') \mathbf{X}'\right] \quad (4.9)$$

For anisotropic media $\mathbf{M}_{mn}(x_3')$ is modified as shown below

$$\mathbf{M}_{mn}(x_3') = \mathbf{M}_{mn}(0) \left[\mathbf{I} + \frac{D}{c_p} \mathbf{S}_p \mathbf{M}_{mn}(0) \right]^{-1} \quad (4.10)$$

Where c_p depends on the angle of propagation in anisotropic media.

The normalized velocity field from an array of transducers can be then given as follows

$$\mathbf{v} = \sum_{j=1}^N \mathbf{v}_j \exp(i\omega t_j) \quad (4.11)$$

Where t_j is the time delay applied to the j^{th} array element to focus and steer the beam and v_j is the normalized velocity field of a single element. For both focusing and steering the beam the time delay to be applied t_j is given below [6]

$$t_j = \frac{F}{c_p} \left\{ \left[1 + \left(\frac{\bar{N}e}{F} \right)^2 + \frac{2\bar{N}e}{F} \sin \theta_j \right]^{1/2} - \left[1 + \left(\frac{(j-\bar{N})e}{F} \right)^2 + \frac{2(j-\bar{N})e}{F} \sin \theta_j \right]^{1/2} \right\} \quad (4.12)$$

Where F is the focus distance, e is the pitch of the element, $\bar{N} = (N-1)/2$ where N is the number of elements and θ_j is the steering angle of each element.

In anisotropic media, it is important to have accurate angles of propagation from the element to the desired point as the velocity used to calculate the time delays is dependent on the angle of propagation of the beam. Using ray theory [7] and tracing the ray from element j to the desired point at a distance F and angle θ_j , we calculate the phase velocity along this ray. Using this calculated phase velocity we then apply the accurate time delay to the element.

As has been observed in work done by Park et al. [5] that the ordinary multi Gaussian beam model fails when the beam is steered above 20° in isotropic media due to violation of the paraxial approximation. It is shown later in this paper that the same behaviour is observed in anisotropic media. To solve this problem a linear phasing is applied to the array elements as shown in the next section. The linearly phased MGB beam model is then modified to simulate phased array ultrasonic beams in anisotropic structures.

4.3.2 Development of Linearly phased MGB (LMGB) from an array into anisotropic media

Huang et al. [8] showed that by introducing a continuous linearly varying phase on the face of the transducer, a steered sound beam can be produced from a virtual transducer which has its axis in the steering direction. They also showed that the phasing of a Gaussian beam would shift it to a steering direction which is still within the paraxial limit.

The nonparaxial expansion given by Zhao and Gang [9], though appropriate for a single layered isotropic medium, is not suitable for a multi-layered anisotropic medium due to the fact that the formulation does not support the formation of \mathbf{M} matrices which reduce the complexity when dealing with multi-layered anisotropic media. When dealing with layered media, the \mathbf{M} matrices can be further decomposed into A, B, C and D matrices which make beam radiation calculation in layered media simpler.

Hence the linear phasing on the face of the transducer can be applied by rotating the coordinates in the required steering direction from the central axis of the array θ as shown in Fig. 4.2.

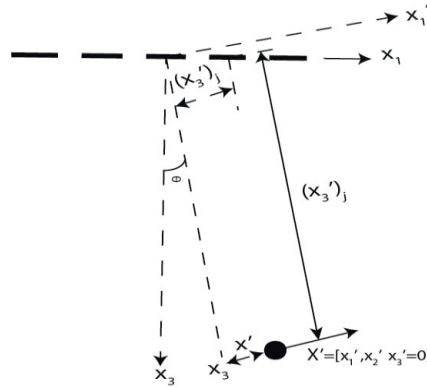


Fig. 4.2 Shows the now rotated coordinates in the steering direction

Doing so, the coordinates and the $\mathbf{M}(0)$ matrix have to be modified to simulate the linear phasing over each element. The velocity has to be also multiplied by an amplitude correction factor $(1/\cos\theta_j)$ as shown in the following equation. Owing to the anisotropic nature of the material, θ_j has to be calculated separately for each element using ray theory. It should be added here that θ_j corresponds to the steering angle from element j whereas θ corresponds to the steering angle from the centre of the array.

$$v'_j(x'_1, x'_2, x'_3) = \frac{1}{\cos\theta_j} v_j \left(\begin{array}{l} x_1 \rightarrow x'_1, x_2 \rightarrow x'_2, x_3 \rightarrow x'_3, d \rightarrow d' \\ \mathbf{M}(0) \rightarrow \frac{1}{\cos^2\theta_j} \mathbf{M}(0) \end{array} \right) \quad (4.13)$$

Using the OMGB model for a phased array in anisotropic media and modifying it to include the amplitude correction factor and modified phase velocity, the velocity field for the j^{th} element is given below

$$\mathbf{v}'_j = \exp(ikx'_3) d' \sum_{m=1}^{10} \sum_{n=1}^{10} \frac{A_n A_m}{\sqrt{1 + \frac{c_p}{u_p} x'_3 [\mathbf{M}_{mn}(0)]_{11}} \sqrt{1 + \frac{c_p}{u_p} x'_3 [\mathbf{M}_{mn}(0)]_{22}}} \quad (4.14)$$

$$\times \exp\left(\frac{i\omega}{2} \mathbf{X}'^T \mathbf{M}_{mn}(x'_3) \mathbf{X}'\right)$$

Where d' is the polarization vector and

$$[\mathbf{M}_{mn}(x'_3)]_{11} = \frac{[\mathbf{M}_{mn}(0)]_{11}}{1 + x'_3 \frac{c_p}{u_p} (c_p - 2C) [\mathbf{M}_{mn}(0)]_{11}} \quad (4.15)$$

$$[\mathbf{M}_{mn}(x'_3)]_{22} = \frac{[\mathbf{M}_{mn}(0)]_{22}}{1 + x'_3 \frac{c_p}{u_p} (c_p - 2E) [\mathbf{M}_{mn}(0)]_{22}} \quad (4.16)$$

$$\mathbf{X}'_j = [x'_1 \ x'_2]$$

Directivity of the element also plays an important role in an array as it describes the beam spread depending on the size of the element and the angle of propagation. The directivity for each element is as shown below [6]

$$D_r = \frac{\sin\left[\frac{(ka_1 \sin \theta_j)}{2}\right]}{(ka_1 \sin \theta_j)/2} \quad (4.17)$$

The directivity can then be included in Eq. (4.13) as follows

$$\mathbf{v}'_j = D_r \exp(ikx'_3) d' \sum_{m=1}^{10} \sum_{n=1}^{10} \frac{A_n}{\sqrt{1 + \frac{c_p}{u_p} x'_3 [\mathbf{M}_{mn}(0)]_{11}}} \times \frac{A_m}{\sqrt{1 + \frac{c_p}{u_p} x'_3 [\mathbf{M}_{mn}(0)]_{22}}} \quad (4.18)$$

$$\times \exp\left(\frac{i\omega}{2} \mathbf{X}'^T_j \mathbf{M}_{mn}(x'_3) \mathbf{X}'_j\right)$$

Hence Eq. (4.17) represents the developed LMGB model.

The next subsection presents details on how the FEM simulation was carried out.

4.3.3 Development of the FEM model using COMSOL

The numerical model was computed using commercially available FEM software COMSOL Multiphysics 5.4. An implicit solver was used to solve this problem. The construction of the FEM model in COMSOL comprises of the following steps

1. Construction of geometry: For verifying the model at hand, it consists of a 2D rectangular domain representing an anisotropic material with a number of line elements at the upper boundary which represent the array elements.

2. Definition of the domain and the boundary conditions: For the domain, this consists of the definition of the material properties (density and elastic tensor). A boundary force is applied on the array elements. These take into account the time delays to be applied to focus and steer the beam. For the other boundaries perfectly matching layers (PMLs) are defined to model an infinitely large domain so as to reduce the reflections from the boundaries.

3. The computational region has to be discretized into smaller elements (i.e. mesh elements) on which the solutions will be calculated. For this problem quadratic triangular Lagrange elements are chosen. For ultrasonic propagation problems, it is recommended that the element size should be less than $\lambda/6$ where λ is the wavelength [10] .

4. Post processing of the output: The model output is then post processed to remove the shear wave contributions. This is done by using spatial Fourier transform to identify the wave number of the shear waves and longitudinal waves. The shear wave contribution is then completely filtered out as the shear wave numbers are different from the longitudinal wave numbers owing to the large difference in velocities and as an inverse Fourier transform returns only the longitudinal wave contribution in the beam.

For this thesis, the COMSOL model consisted of a rectangular domain 80 mm x 100 mm with mesh elements of the size of $\lambda/7$. The PMLs of dimensions 100 mm x 20 mm are defined at the boundaries of the rectangular domain. The domain material properties are user defined as shown in Table I in the next section.

Fig. 4.3 shows an example where the beam is steered at an angle of 20° . In Fig. 4.3(a) the wavefield is consisting of both quasi-longitudinal and quasi-shear waves. Quasi longitudinal and quasi shear waves are longitudinal and shear waves coupled together where the particles are not polarised along the principle axis of polarization. Fig. 4.3(b) shows the wavenumbers present where k_1 is the wavenumber component in the x_1 direction and k_3 is the wavenumber component in the x_3 direction. The magnitude of the Fourier transform of the displacements corresponding to the wavenumbers are shown in the image. The lower value of k_3 corresponds to the quasi-longitudinal wave. Fig. 4.3(c) shows the wavefield after filtering out the shear wave contribution. The beam field now consists of the quasi-longitudinal wave.

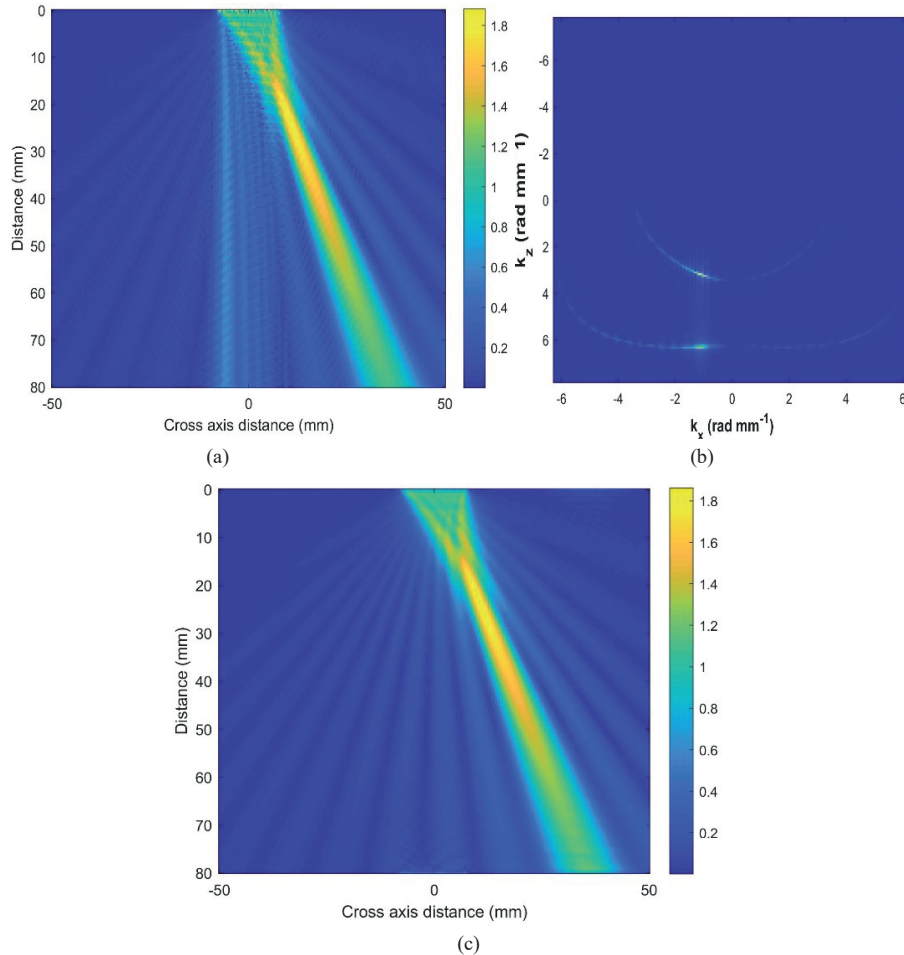


Fig 4.3. (a) Beam field with quasi longitudinal and quasi shear waves (b) Wave numbers corresponding to quasi longitudinal and quasi shear waves (c) Beam field consisting of only the quasi longitudinal wave

4.4 Simulation results

In this section I present results simulated by the OMGB and LMGB model for linear phased arrays in anisotropic materials. These models were programmed and executed using MATLAB 2016. These results are also verified by comparing them to the results obtained by a numerical finite element model implemented in the commercially available software package COMSOL Multiphysics. The setup and geometry under consideration is given in Figure 4.4 where it is considered that the phased array transducer is placed on the top surface of the a block of austenitic steel.

Phased array Transducer

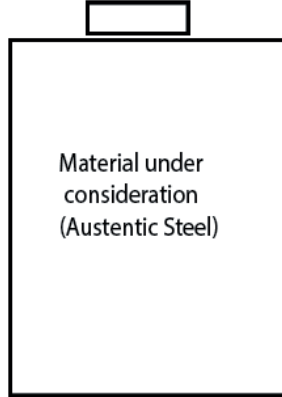


Fig 4.4 Setup considered for simulation

The elastic constants of austenitic steel are given in the table below [11].

Table 4.1 [11]
Material properties of Austenitic Steel

Material properties	Value
$C_{11}=C_{22}$	241.10 GPa
C_{33}	240.12 GPa
C_{12}	96.92 GPa
$C_{13}=C_{23}$	138.03 GPa
$C_{44}=C_{55}$	112.29 GPa
C_{66}	72.09 GPa
Density (ρ)	7820 kg/m ³

The phased array ultrasonic transducer modelled consists of 32 elements, with an element pitch of 0.49 mm, an element width of 0.49 mm and a centre frequency of 2.25 MHz. These parameters were chosen so as to reduce the computation times and the use of computational resources in COMSOL because

with an increase in the number of nodes and number of elements, the FEM simulation takes a longer time to run on a personal computer and is computationally expensive. The beam profile was computed to a depth of 80 mm in the solid and with a desired beam focus F at 40 mm so as to observe the beam field in the far-field and to capture all the effects of anisotropy on the beam propagation and to reduce the reflections from the model edges and corners in COMSOL. It has to be noted here that the magnitudes of the beam profiles plotted are dimensionless quantities.

In the following sections I will first illustrate the beam distortion effects in austenitic steel. Next I will compare the OMGB and LMGB models for angles below the paraxial restriction and after that I will present the comparison and verification of the LMGB model for angles above the paraxial restriction.

4.4.1 Effect of slowness surface curvatures on the beam

The slowness of a wave is the inverse of the phase velocity which is calculated by solving the Christoffel equation which is shown in Eq (4.21).

$$c_{ijkl}n_jn_k - \rho c_p^2 \delta_{il} = 0 \quad (4.21)$$

Where c_{ijkl} are the elastic constants, n is unit vector in the direction of wave propagation, ρ is the density of the material, c_p is the phase velocity and δ is the kronecker delta. Solving the eigenvalue Eq.(4.21) gives the c_p and the inverse of c_p which is the slowness value.

A slowness surface is formed by the loci of the slowness in various directions. The importance of the slowness is the fact that it is directly proportional to the wave number and can be regarded as the wave number at an angular frequency of unity.

Fig. 4.4 shows the slowness surfaces of austenitic steel for quasi longitudinal (qp), quasi shear horizontal (qsh) and quasi shear vertical (qsv) waves (Fig. 4.5 (a)), as well as the variation of the C and E parameters (Fig .4.5 (b)) and the beam skew (Fig. 4.5 (c)).

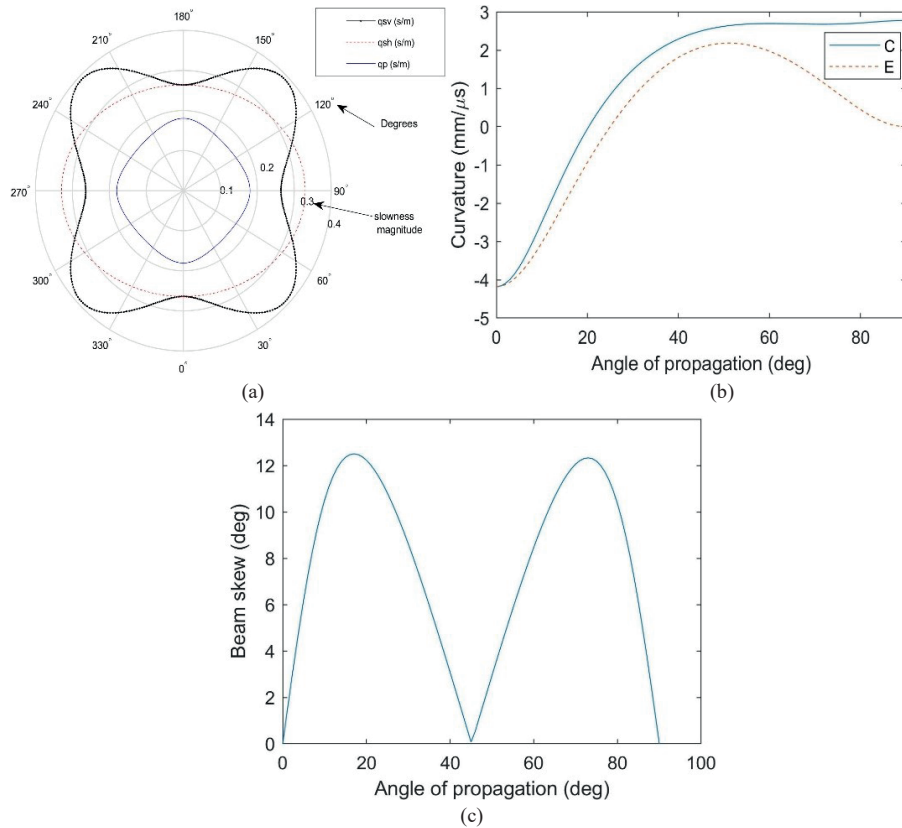


Fig 4.5. (a) Slowness surfaces, (b) Slowness surface curvatures C and E and (c) Beam skew

To show the effect of the slowness parameters on the beam propagation, the values are artificially varied from $C=E=0$ (isotropic case) to $C=E=-4.9 \text{ mm}/\mu\text{s}$ which is arbitrarily chosen to demonstrate the effects of the slowness parameters on the beam propagation. Beam profiles here obtained using the OMGB model for 0° propagation and are shown with the corresponding curvature values in Fig. 4.6.

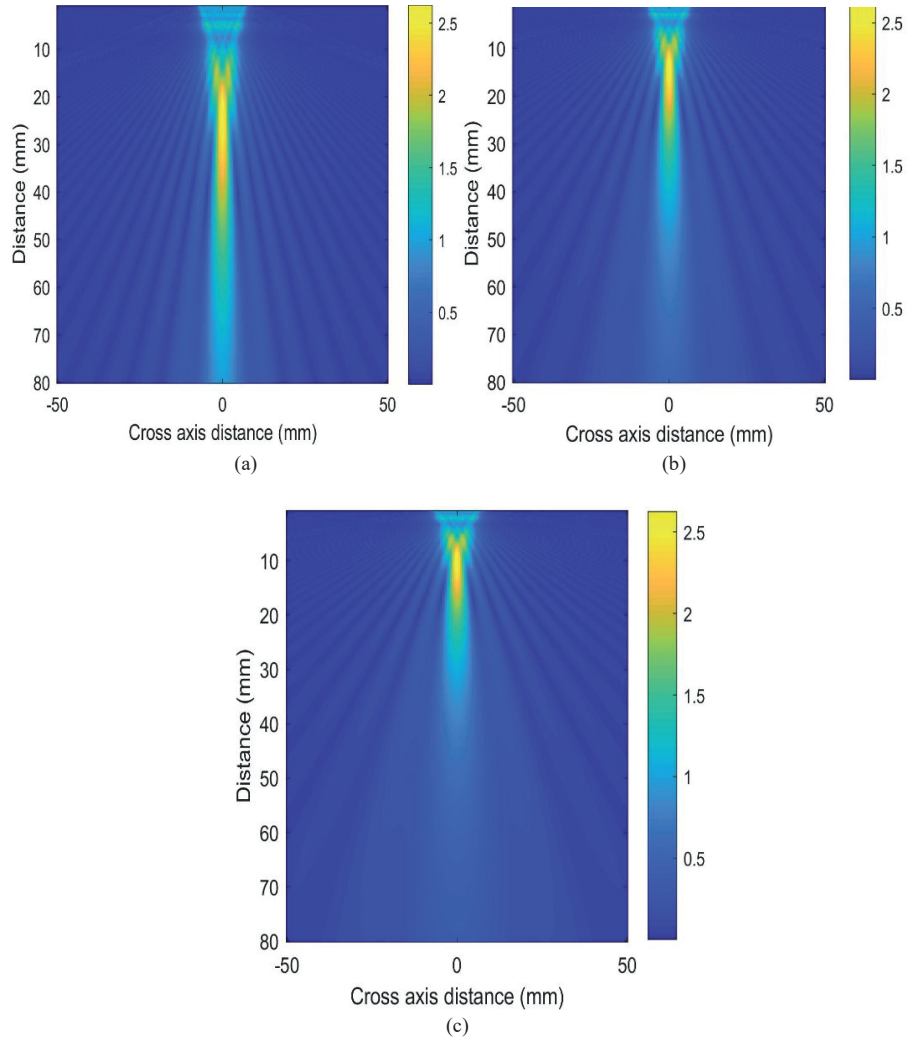


Fig 4.6. Beam field (a) $C=E=0$, (b) $C=E=-2.5$ mm/ μ s and (c) $C=E=-4.9$ mm/ μ s

To see the effect of the slowness parameters we chose the desired focus F to be 40 mm and the steering angle θ is 0° so as to isolate the effect of the slowness parameters on the amplitude of the beam without any effect of beam steering. It can be seen in Figure 4.6 that as the curvature values move towards 0 the beam extends whereas for larger negative curvature values as seen in Figure 4.6 (c) the beam moves towards the face of the transducer (compresses). It can also be seen that between the isotropic Figure 4.6 (a) and anisotropic slowness surface Figure 4.6 (c) curvatures, compression is by a factor of 2.5 as the maximum amplitude in Figure 4.6 (a) occurs at 25 mm and for Figure 4.6 (c) it occurs at 10 mm. The

periodic features which are seen in the figure apart from the main beam are the side beams emanating from the side lobes which have strength less than the main beam in the range of 0 to 0.5 times the maximum amplitude of the main beam.

4.4.2 Comparison of the OMGB and LMGB models below the paraxial limit

Figures. 4.7 and 4.8 show the comparison between the Ordinary Multi Gaussian Beam (OMGB) and Linearly Phased Multi Gaussian Beam (LMGB) models steered at an angle of 0° and 10° respectively and focused at 40 mm. These parameters were chosen so as to compare the results between a non-steering case which forms the baseline and a steered case below the paraxial limit. As can be seen in the figures, both the LMGB and OMGB models are approximately the same for angles below 20° . The slowness curvature values for the steering angle 0° are $C = E = -4.18 \text{ mm}/\mu\text{s}$ and for the steering angle 10° are $C = -2.4856 \text{ mm}/\mu\text{s}$, $E = -3.0292 \text{ mm}/\mu\text{s}$. These differences arise due to the anisotropic nature of the material which causes different slowness values and hence different phase and group velocities in different directions. C and E are different as they are the second derivative of the slowness values in the x_1 and x_2 directions respectively and the slowness surfaces in 3-dimensional space are different along different directions.

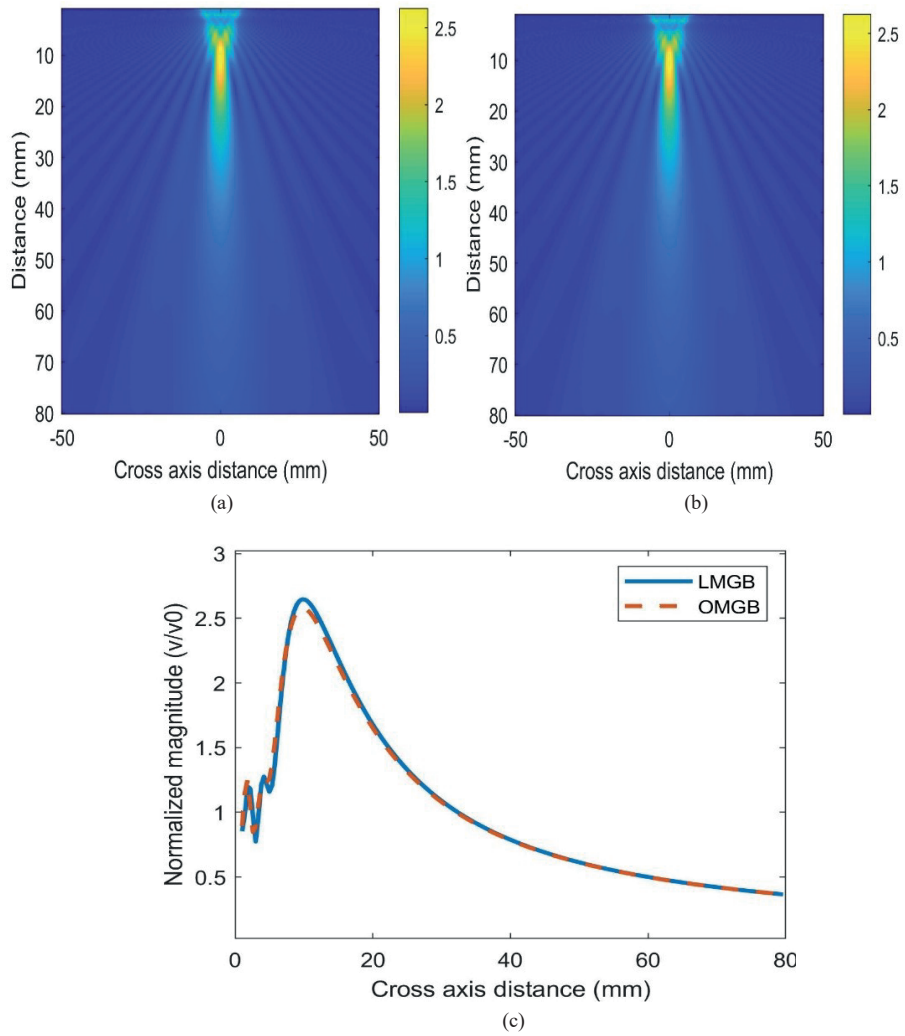


Fig 4.7. Beam field at a steering angle of 0° using (a) OMGB (b) LMGB (c) Onaxis magnitude

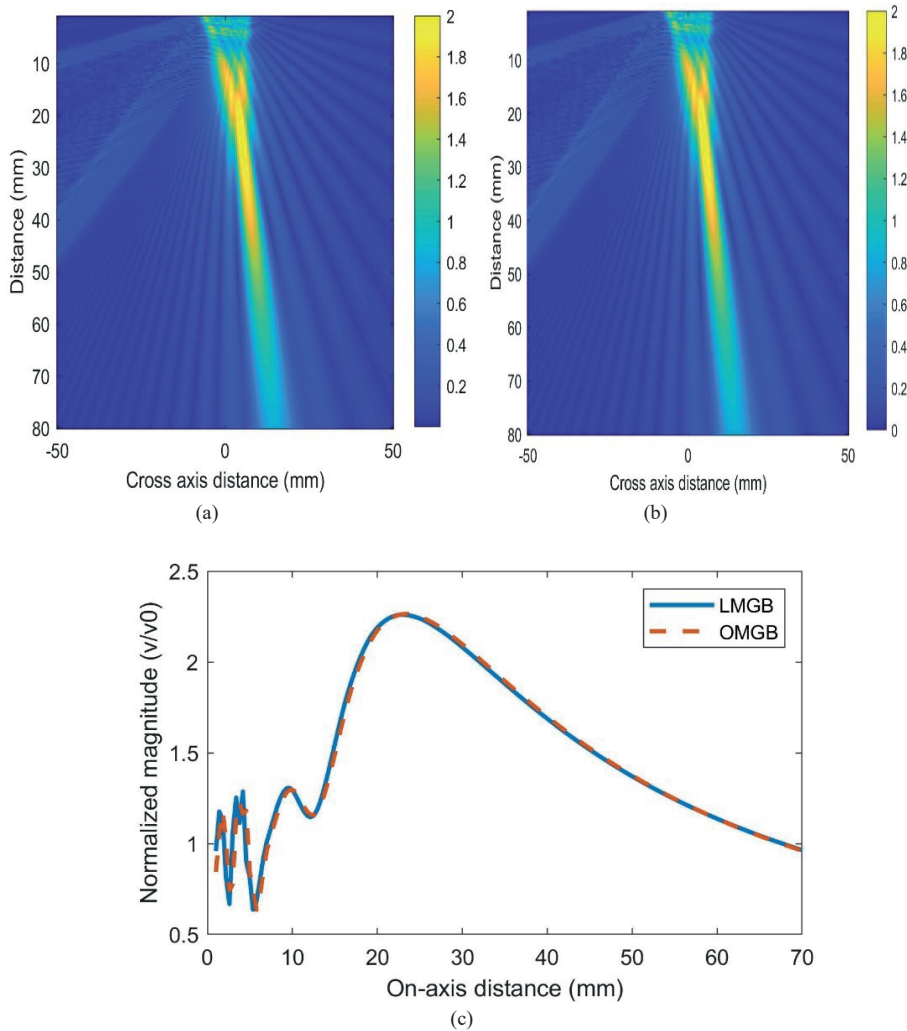


Fig 4.8. Beam field at a steering angle of 10° using (a) OMGB (b) LMGB (c) On axis magnitude

4.4.3 Comparison of OMGB, LMGB and FEM models above the paraxial limit

Fig. 4.9 (a), (b) and (c) show the beam propagation calculated using COMSOL, LMGB and OMGB models respectively, when the beam is steered at an angle of 30° with slowness curvature values, $C = 1.4888 \text{ mm}/\mu\text{s}$, $E = 0.7769 \text{ mm}/\mu\text{s}$

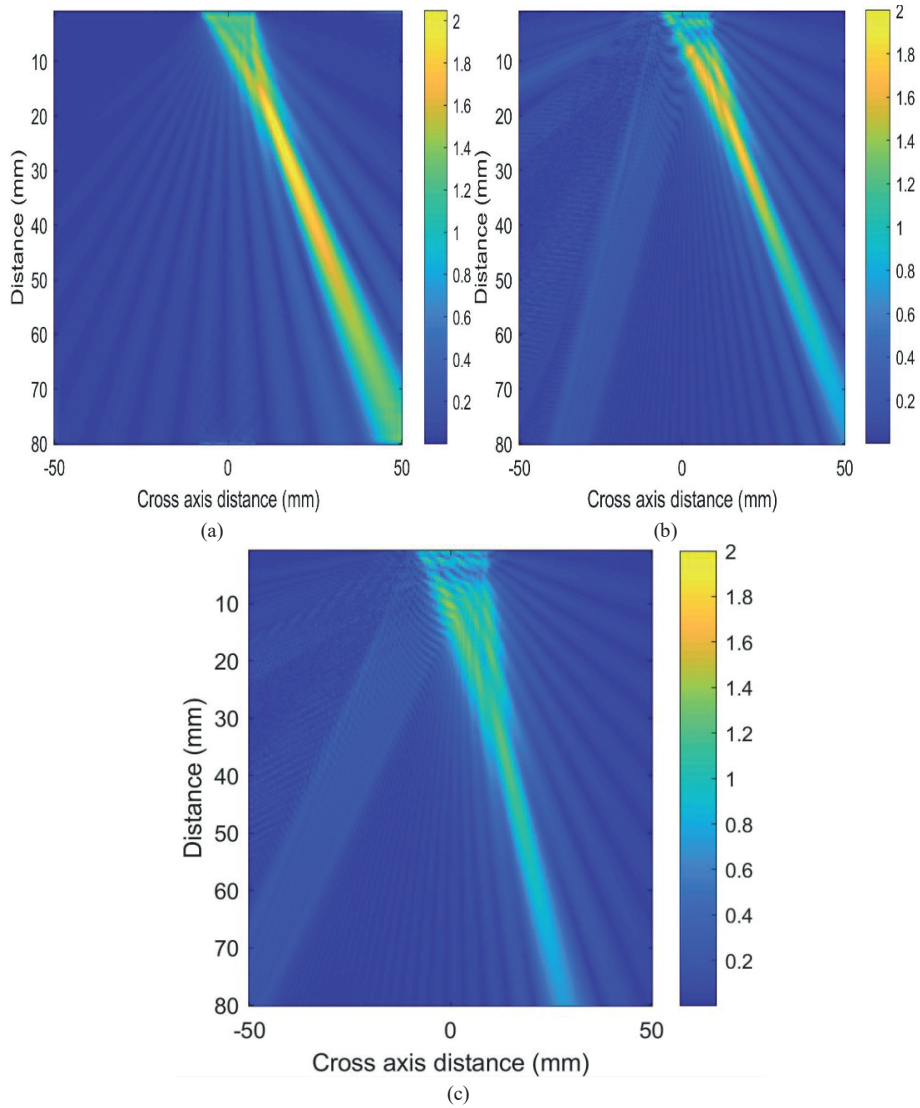


Fig 4.9. Beam field using (a) COMSOL (b) LMGB (c) OMGB for a steering angle of 30°

It is seen from Figure 4.9. that the shape and structure of the beam remains intact for both the numerical (COMSOL) and the LMGB model whereas the beam loses its shape and structure when computed using the OMGB model. This is attributed to the beam from the array elements not being in the paraxial limit. The linear phasing applied to the elements in the LMGB model shifts the axis for each element in the steered direction hence maintaining the paraxial limit in the steering direction. It is also noted that the magnitude curve for FEM falls slower than that using analytical models, hence the beam appears to extend for a longer distance.

Two factors have been attributed to this 1) The array elements used in the analytical models have finite lengths and widths, whereas in the COMSOL simulation though the array elements have a finite width as the computation is considered only in Two-dimensional coordinate system, their lengths are relatively infinite affecting the beam extension. 2) The slowness surface curvatures control the beam diffraction effects and these curvature values are approximates found by fitting a second order polynomial to the slowness. Using higher order polynomials might give more accurate slowness curvature values eliminating this discrepancy too.

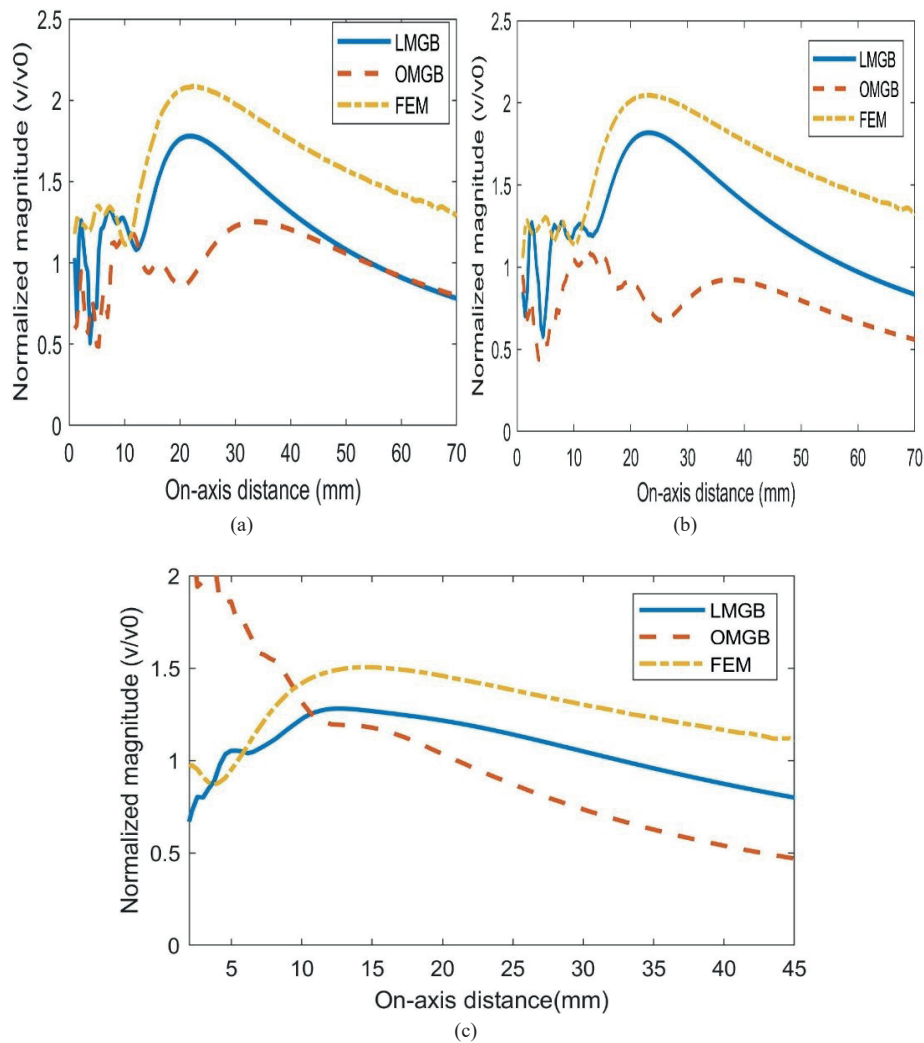


Fig.4.10. On axis beam fields calculated using the analytical and numerical models for steering angles of (a) 20° (b) 30° (c) 45°

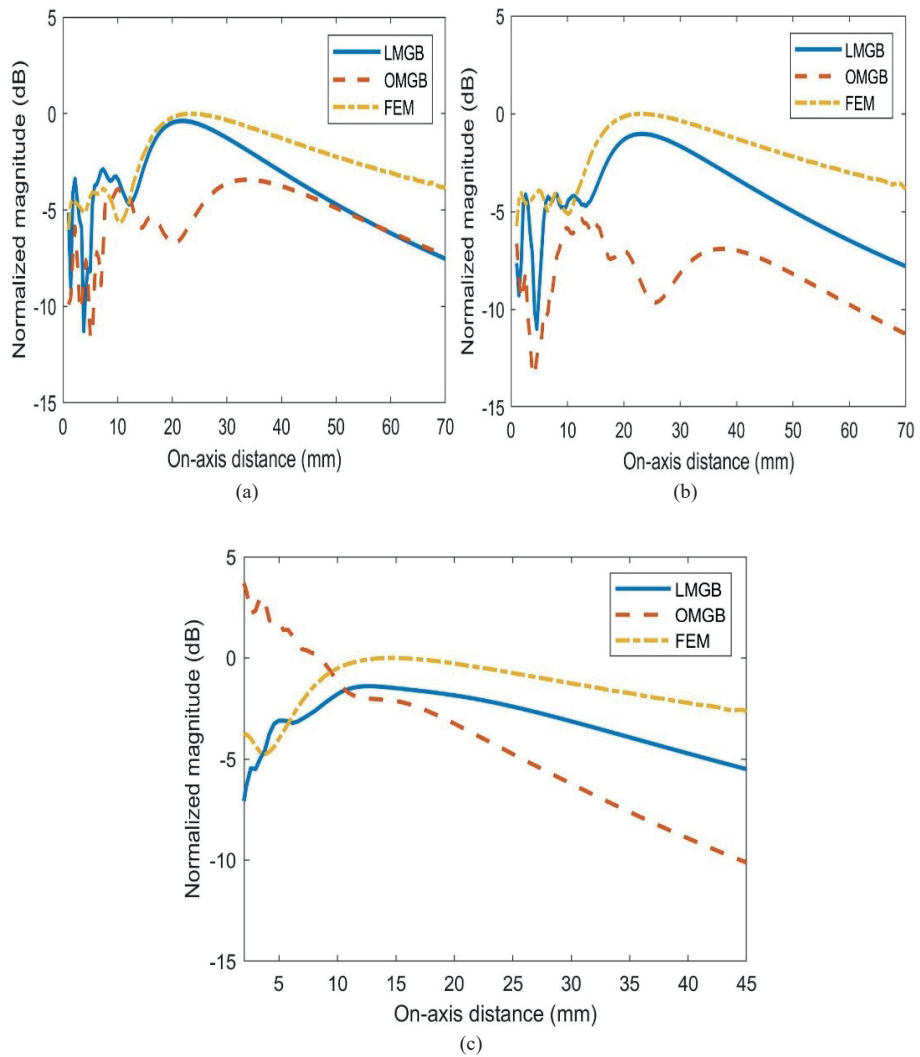


Figure 4.11. On axis beam fields calculated using the analytical and numerical models for steering angles of (a) 20° (b) 30° (c) 45° in the decibel (dB) scale.

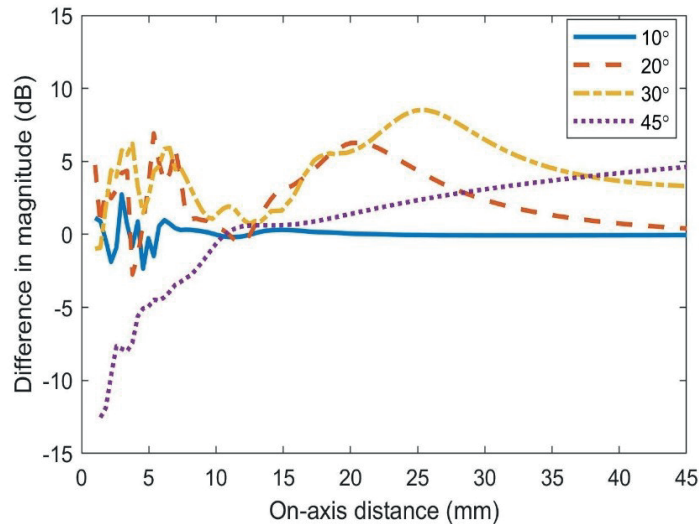


Figure 4.12. Difference in on-axis amplitudes (dB) for different steering angles between the LMGB and OMGB models

As can be seen in the figures, the shape and structure of the beam is maintained for the COMSOL and LMGB cases whereas it breaks down for the OMGB model. The OMGB breaks down due to the dependence of the model on the paraxial approximation which basically assumes that the beam from a transducer is well collimated and traveling perpendicular to the face of the transducer. When the beam is steered it violates this basic assumption of the paraxial approximation and hence leads to erroneous results. Fig. 4.10 (a), (b) and (c) show the on-axis pressure calculated by the three modelling techniques for steering angles 20°, 30° and 45° respectively. It can be seen that at higher steering angles the on-axis magnitude calculated using the OMGB model is drastically different from the LMGB and COMSOL models due to the beam propagating above the paraxial limit for the OMGB model. Fig 4.11 (a), (b), and (c) show the on-axis pressure calculated by the three modelling techniques for steering angles 20°, 30° and 45° respectively in the decibel scale (dB). Fig. 4.12 shows a comparison between the LMGB and OMGB models for different angles at different on-axis distances in dB scale. It is observed that as the angle of propagation increases, the relative error in the far-field increases, the reason being that within a small distance from the face of the transducer the beam can still be assumed to propagate in a direction perpendicular to the transducer face but as the distance increases this assumption fails as the beam is no longer traveling perpendicular to the face of the transducer when steered above 20°.

4.5 Discussions

While comparing the normalized magnitude of the on axis pressure of the three models, it is seen that the COMSOL and the LMGB model show the same shape and structures with an error of +/- 1 dB as seen from Fig. 4.11 of the maximum magnitude, in contrast to the OMGB model. The slight discrepancy in the normalized magnitude in the COMSOL and LMGB models is attributed to the fact that the normalization depends on the magnitude at the surface of the elements which might differ in the different approaches as it is in the near field of the beam. It is also seen from Figure 4.6, that the C and E slowness parameters control the beam diffraction. The beam is seen to move towards the transducer (compression) when the slowness values are varied from 0 to $-4.9 \mu\text{m/s}$. Hence for austenitic steel, even though the focus required is 40 mm, the beam moves towards the transducer with a focus at 15 mm. This is consistent with the anisotropy factor AF as given below [12]

$$AF = \frac{C_{44}}{C_{33}} + \frac{(C_{13} + C_{44})^2}{C_{33}(C_{33} - C_{44})} \quad (4.19)$$

For an isotropic material AF is unity whereas for austenitic steel it is 2.51. This means that traveling along the z axis in austenitic steel, the equivalent distance that the beam has to travel in an isotropic material to achieve the same diffraction is $2.51z$.

Fig. 4.5 (c) shows the beam skew angles but by applying the time delays it is seen from Figures 4.8 and 4.9 that the skewing can be overcome.

At this point it can also be noted that though the numerical model was able to predict the beam propagation, a relatively larger amount of computational resources and time as compared to the multi Gaussian beam models was required to compute it. The LMGB/OMGB models took 180s on a personal computer with 8 GB of RAM whereas the COMSOL model took 400s on a computer with 32 GB of RAM. Also restrictions were placed on the highest frequency which can be modelled as for shorter wavelengths the number of nodes increases hence increasing computational time.

The model proposed in this chapter is suitable for tracking a beam through the material so as to observe the influence of the material on the beam parameters. When the beam passes through multi layered materials where the thickness of the layers is comparable to the wavelength of the passing wave such as layered composite materials, the layers reverberate due to resonance and multiple echos are seen from the different layers. Tracking the beam in such a scenario is

computationally expensive as the number of beams becomes very large and is a very complex combinatorial problem [13].

4.6 Conclusions

In this chapter a modelling approach for anisotropic media using phased arrays was developed to optimize the inspection of such structures. The modelling approach used the linearly phased multi Gaussian beam model (LMGB) to calculate the beam fields in anisotropic media. Comparisons between the Ordinary multi Gaussian beam model (OMGB) and the LMGB model, verified by a numerical model, show that the LMGB model is able to predict beam fields successfully even when the beam is steered above 20° . It is also seen that owing to the anisotropic nature of the material, beam compression takes place due to which the location of the focal point also changes. Beam skewing is also observed due to the anisotropic nature of the material which is compensated by calculating the appropriate time delays.

As this thesis is concerned with the output signal received from inspection of composite materials, the next chapter develops a model which combines the beam emitted from a phased array transducer to the plane wave response of a composite material.

4.7 References

- [1] J. C. Williams and E. A. Starke, "Progress in structural materials for aerospace systems," *Acta Mater.*, 2003, doi: 10.1016/j.actamat.2003.08.023.
- [2] R. Huang, "Ultrasonic modeling for complex geometries and materials," *Iowa State Univ.*, 2006, [Online]. Available: <http://adsabs.harvard.edu/abs/2006PhDT.....54H>.
- [3] J. J. Wen and M. A. Breazeale, "A diffraction beam field expressed as the superposition of Gaussian beams," *J. Acoust. Soc. Am.*, vol. 83, no. 5, pp. 1752–1756, 1988, doi: 10.1121/1.396508.
- [4] D. Ding, Y. Zhang, and J. Liu, "Some extensions of the Gaussian beam expansion: Radiation fields of the rectangular and the elliptical transducer," *J. Acoust. Soc. Am.*, vol. 113, no. 6, p. 3043, 2003, doi: 10.1121/1.1572144.
- [5] J. S. Park, S. J. Song, and H. J. Kim, "Calculation of Radiation Beam Field from Phased Array Ultrasonic Transducers Using Expanded Multi-Gaussian Beam Model," *Solid State Phenom.*, vol. 110, pp. 163–168, 2006, doi: 10.4028/www.scientific.net/SSP.110.163.
- [6] L. W. Schmerr, *Fundamentals of Ultrasonic Phased Arrays*, vol. 215, no. May 2003. Cham: Springer International Publishing, 2015.
- [7] V. Červený, *Seismic ray theory*. Cambridge University Press, 2001.
- [8] R. Huang, L. W. Schmerr, and A. Sedov, "Modeling the radiation of ultrasonic phased-array transducers with Gaussian beams," *IEEE Trans. Ultrason. Ferroelectr. Freq. Control*, vol.

- 55, no. 12, pp. 2692–702, 2008, doi: 10.1109/TUFFC.2008.984.
- [9] X. Zhao and T. Gang, “Nonparaxial multi-Gaussian beam models and measurement models for phased array transducers.,” *Ultrasonics*, vol. 49, no. 1, pp. 126–30, 2009, doi: 10.1016/j.ultras.2008.07.015.
- [10] COMSOL, “COMSOL Multiphysics 5.3 User Guide,” *Manual*, 2014.
- [11] M. Rudolph, “Ultrasonic beam models in anisotropic media,” *Iowa State Univ.*, p. 253, 1999.
- [12] B. P. Newberry and R.B. Thompson, “A paraxial theory for the propagation of ultrasonic beams in anisotropic solids,” *J. Acoust. Soc. Am.*, vol. 85, no. 6, pp. 2290–2300, 1989, doi: 10.1121/1.397775.
- [13] P. F. Daley and F. Hron, “Ray-reflectivity method for SH-waves in stacks of thin and thick layers,” *Geophys. J. R. Astron. Soc.*, vol. 69, no. 2, pp. 527–535, 1982, doi: 10.1111/j.1365-246X.1982.tb04963.x.

5

A Gaussian beam based recursive stiffness matrix model to simulate ultrasonic array signals from composite laminates

Abstract

This chapter proposes a modelling technique based on combining the Multi-Gaussian beam model with the recursive stiffness matrix method to simulate the FMC signals for layered anisotropic media. The chapter provides the steps required for the modelling technique, the extraction of the system efficiency factor and validation of the model with experimentally determined signals for aluminum as an isotropic material and Carbon Fibre Reinforced Plastic (CFRP) laminate as a layered material. The proposed method is computationally inexpensive as compared to numerical models, shows good agreement with the experimentally determined FMC data and enables us to understand the effects of various transducer and material parameters on the extracted FMC signals

Adapted from: C. Anand, R. Groves, R. Benedictus, A Gaussian Beam Based Recursive Stiffness Matrix Model to Simulate Ultrasonic Array Signals from Multi-Layered Media, Sensors 2020

5.1 Introduction

In the previous chapter we saw how beam propagation from a phased array through an homogeneous anisotropic media such as austentic steel can be modeled using Multi Gaussian beams. In recent years layered composite materials are being widely used in primary aircraft structures such as fuselage, wings, etc. [1], [2]. These composite laminates consist of many anisotropic layers of carbon or glass fibres embedded in resin. These layers are stacked on top of each other and cured to fabricate a composite laminate [3]. As per the design requirements the laminates can be of various types such as CFRP , glass fibre reinforced plastic (GFRP) and might consist of a number of layers which have different fibre orientations [4]. Defects might be present in such laminates due to manufacturing process or when in-service [5]–[8]. When such laminates are nondestructively tested using ultrasonic phased arrays, the thickness of the plies being in the order of the wavelength of the inspecting wave of frequencies such as 2.25 or 5 MHz causes the plies to resonate at certain frequencies which gives rise to multiple echos in the received signal. Ply interfaces also scatter the impinging ultrasonic wave due to the presence of small amount of resin left between the plies after manufacture [9]. These multiple echos, interface reflections and direction dependent velocities influence the received ultrasonic signal and might lead to misinterpretation of results. Hence there is a need for computational models to simulate, analyse and study the interaction of finite beam transducers with such multi-layered composite materials by taking into account the above mentioned interactions. The LMGB model developed in the previous chapter is not efficient when applied to a multilayer system where overlapping echos and resonances are present which are not distinguishable. The inefficiency arises due to the high number of beams which need to be tracked due to multiple reflections which leads to a highly complex combinatorics problem [10]. As the interest of this thesis lies in the effects of the beam, ply and structure properties on the received signal, this chapter develops a model which takes into account the beams emitted by a finite sized transducer by modelling it as MGBs and combining it with the plane wave response of the composite laminate. The developed model is used to generate FMC signals for the composite laminate under inspection and the results are verified experimentally. The next section provides the theory which is used to develop the model.

5.2. Theory

5.2.1 Stiffness matrix method for multilayer wave propagation

Let us consider a plane wave impinging on the top layer of a planar multilayer laminate in the x_1 - x_3 plane where the laminate consists of n number of layers as shown in Figure 5.1.

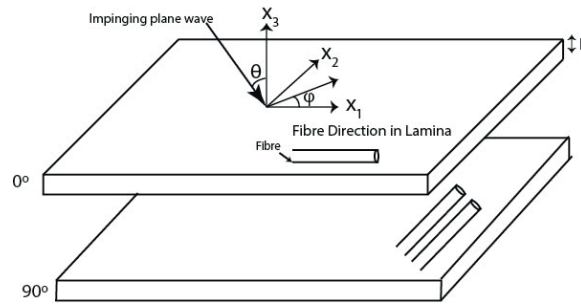


Figure 5.1. CFRP laminas specifying the local axis.

These layers are assumed homogeneous and anisotropic. The anisotropic layers are assumed to be of infinite extent in the plane (x_1 - x_2) normal to the thickness direction. The laminate is bounded by two semi-infinite bounding layers which are denoted by 0 and $n+1$. The plane wave traveling from the upper bounding layer has an incident angle θ with respect to the x_3 axis and its wave vector projection on the x_1 - x_2 plane is denoted by ϕ . The plane wave displacement u in a layer is given by the Eq. (5.1).

$$u = \exp(i(\mathbf{k} \cdot \mathbf{x} - \omega t)) \quad (5.1)$$

Where i is the imaginary number, \mathbf{k} is the wavenumber vector, ω is the angular frequency and t is the time. Due to the application of Snell's law [11] the wavenumber components in the plane of the interfaces should be equal throughout the laminate, i.e. k_1 and k_2 remain the same. The wavenumber component k_3 can be calculated using the Christoffel equation as given below [12]

$$\left(c_{ijkl} k_j k_k - \rho \omega^2 \delta_{il} \right) d_l = 0 \quad (5.2)$$

Where c_{ijkl} is the stiffness tensor, ρ is the density of the material, δ_{il} is the Kronecker delta, d_l is the polarization vector component for different wave modes and $i, j, k,$

l consist of values 1, 2, 3 corresponding to the three axes x_1, x_2, x_3 . Eq. (5.2) can be solved to obtain the values of the wavenumber component k_3 . k_3 will have two solutions for each propagating wave mode. One solution corresponds to the downward going wave in the layer and the other corresponding to the upward traveling wave. The downward traveling wave is denoted here by '+' and the upward traveling wave in the layer by '-'. The wave modes are represented by p with values 1,2 and 3. The quasi-longitudinal wave is represented by $p=3$ and the quasi-shear waves are represented by $p=1,2$.

Hence the displacement in the layer m is given below [13]

$$u_i^m = \sum_{p=1}^3 \left(a^{m,p+} d_i^{m,p+} e^{ik_3^{m,p}(x_3-x_3^m)} + a^{m,p-} d_i^{m,p-} e^{-ik_3^{m,p}(x_3-x_3^m)} \right) e^{i(k_1x_1+k_2x_2-\omega t)} \quad (5.3)$$

where $a^{m,p+/-}$ are the wave amplitudes of the downward and upward traveling waves of mode p in the layer m , $d_i^{m,p+/-}$ is the i th component of the polarization vector (polarization components along the three axes) of wave mode p in the layer m . The coordinate x_3^m is the local coordinate of the layer m . The relationship between the stress and displacement in the layer is given below

$$\sigma_{ij} = \frac{1}{2} c_{ijkl} \left(\frac{\partial u_k}{\partial x_l} - \frac{\partial u_l}{\partial x_k} \right) \quad (5.4)$$

By substituting Eq. (5.3) into Eq. (5.4) a layer stiffness matrix S_m is defined which relates the stresses and displacements at the top and bottom of the layer.

$$\begin{bmatrix} \sigma_{li}^m(0) \\ \sigma_{li}^m(h_m) \end{bmatrix} = S_m \begin{bmatrix} u_i^m(0) \\ u_i^m(h_m) \end{bmatrix} \quad (5.5)$$

Where $\sigma_{li}^m(0)$, $\sigma_{li}^m(h_m)$ are the stress components at the top and bottom of layer m respectively, and $u_i^m(0)$, $u_i^m(h_m)$ are the displacement components at the top and bottom of layer m respectively. The stiffness matrix S_m for the layer is defined as the matrix product shown in Eq. (5.6)

$$S = \begin{bmatrix} \mathbf{F}^+ & \mathbf{D}^+\mathbf{H}^- \\ \mathbf{F}^+\mathbf{H}^+ & \mathbf{F}^- \end{bmatrix} \begin{bmatrix} \mathbf{D}^+ & \mathbf{D}^+\mathbf{H}^- \\ \mathbf{D}^+\mathbf{H}^+ & \mathbf{D}^- \end{bmatrix}^{-1} \quad (5.6)$$

In Eq.(5.6) \mathbf{F} is the matrix consisting of force vectors of the three propagating modes of the wave as shown in Eq. (5.7) , \mathbf{D} is a matrix consisting of the polarization vectors as shown in Eq. (5.8) and \mathbf{H} is a diagonal matrix in which the propagators are distributed along the diagonal with the other elements of matrix being zero. In Equations (5.6), (5.7) and (5.8) subscripts 1,2 and 3 correspond to the different wave modes.

$$\mathbf{F}^\pm = [\mathbf{f}^{\pm 1} \quad \mathbf{f}^{\pm 2} \quad \mathbf{f}^{\pm 3}] \quad (5.7)$$

$$\left(f_i^{\pm p} \right)_m = i(c_{i3kl} k_l p_k)$$

$$\mathbf{D}^\pm = [\mathbf{d}^{\pm 1} \quad \mathbf{d}^{\pm 2} \quad \mathbf{d}^{\pm 3}] \quad (5.8)$$

$$\mathbf{H}^\pm = \text{Diag}[e^{ik_3^\pm h_m} \quad e^{ik_3^\pm h_m} \quad e^{ik_3^\pm h_m}] \quad (5.9)$$

In order to define the stiffness matrix for the entire structure, continuity of stress and displacement is applied at each interface. The equation relating the stress in the upper semi-infinite bounding layer and the lower semi-infinite bounding layer is given below.

$$\begin{bmatrix} \sigma_{li}^0 \\ \sigma_{li}^{n+1} \end{bmatrix} = S_N \begin{bmatrix} u_i^0(0) \\ u_i^{n+1}(h_n) \end{bmatrix} \quad (5.10)$$

Where S_N is the combined stiffness matrix for the entire structure, σ_{li}^0 , σ_{li}^{n+1} are the stress components in the upper and lower bounding layers respectively and $u_i^0(0)$, $u_i^{n+1}(h_n)$ are the displacement components in the upper and lower bounding layers respectively . The above equation can be solved for the unknown reflection and transmission coefficients. Eq. (5.10) leads to the calculation of 9 unknowns from 6 equations. If the bounding layers are considered to be water, then the above equation is simplified as we know the properties of water, the boundary conditions and the wave modes supported in water. As water is the upper bounding layer, the incident wave can only be a longitudinal wave, hence we now know the stress and displacement on the top layer caused by the incident wave. Choosing water as the bounding layer reduces the number of unknowns, while also considering the no-slip boundary condition between the upper semi-infinite bounding layer and the first interface, and the lower semi-infinite bounding layer and the last interface,

$$\begin{aligned} u_1^0(0) &= u_2^0(0) = 0 \\ u_1^{n+1}(h_n) &= u_2^{n+1}(h_n) = 0 \end{aligned} \quad (5.11)$$

The reflection coefficient can be calculated using the below equation [9].

$$R = -\frac{(S_{11}^{33} - \Lambda)(S_{22}^{33} - \Lambda) - S_{21}^{33}S_{12}^{33}}{(S_{11}^{33} + \Lambda)(S_{22}^{33} - \Lambda) - S_{21}^{33}S_{12}^{33}} \quad (5.12)$$

Where S_{mn}^{33} is the (3,3) component of the constitutive matrices of S and

$$\Lambda = -\frac{\cos\theta}{i\omega\rho_f V_f}$$

Where ρ_f and V_f are the density and velocity of sound in water respectively
The next section shows the theoretical fundamentals of multi-Gaussian beams.

5.2.2 Modelling of the transducer Gaussian beams

Recapping from Section 4.3.1 in Chapter 4 we know that, the transducer response of a phased array at a distance z in a fluid or isotropic solid, from the face of the transducer can be modelled as a superposition of multi Gaussian beams [14] as shown below

$$\mathbf{v}_j(x_1, \omega) = \mathbf{d} \exp\left(i\omega \frac{x_3}{c}\right) \sum_{m=1}^{10} \sum_{n=1}^{10} \frac{A_n A_m}{\sqrt{1+cx_3} [\mathbf{M}_{mn}(0)]_{11} \sqrt{1+cx_3} [\mathbf{M}_{mn}(0)]_{22}} \exp\left[\frac{1}{2} X^T \mathbf{M}_{mn}(x_3) X\right] \quad (5.13)$$

Where \mathbf{X} are the coordinates between the j^{th} transmitting element and the receiving elements, c is the wave velocity, x_3 is the distance travelled along the x_3 axis in Figure 5.1 and \mathbf{d} is the polarization vector.

$$\begin{aligned} [\mathbf{M}_{mn}(0)]_{11} &= \frac{iB_m}{D_1}, [\mathbf{M}_{mn}(0)]_{22} = \frac{iB_n}{D_2} \\ D_1 &= \frac{ka_1^2}{2}, D_2 = \frac{ka_2^2}{2} \end{aligned} \quad (5.14)$$

$$\begin{aligned}
[\mathbf{M}_{mn}(x_3)]_{11} &= \frac{[\mathbf{M}_{mn}(0)]_{11}}{1 + cx_3 [\mathbf{M}_{mn}(0)]_{11}} \\
[\mathbf{M}_{mn}(x_3)]_{22} &= \frac{[\mathbf{M}_{mn}(0)]_{22}}{1 + cx_3 [\mathbf{M}_{mn}(0)]_{22}} \\
[\mathbf{M}_{mn}(x_3)]_{12} &= [\mathbf{M}_{mn}(x_3)]_{21} = 0
\end{aligned} \tag{5.15}$$

In the above equations k is the wave number and a_l and a_2 are the width and length of the rectangular transducer respectively. A_n, A_m, B_n, B_m are the Wen and Breazeale coefficients [15]. Wen and Breazeale expressed the radiation from a circular transducer as a superposition of Gaussian beams with coefficients obtained by nonlinear optimization. These coefficients were expanded for a rectangular transducer by Ding et al [16].

Hence at the face of the transducer where $x_3=0$ the velocity distribution is given below

$$\mathbf{v}_j(x, \omega) = \sum_{m=1}^{10} \sum_{n=1}^{10} A_n A_m \exp \left[\frac{1}{2} X^T \mathbf{M}_{mn}(x_3) X \right] \tag{5.16}$$

The velocity distribution in the wavenumber-frequency domain can be calculated as given below by substituting Eq. (5.16) in Eq. (5.17)

$$\mathbf{v}_j(k, \omega) = \int_{-\infty}^{\infty} \mathbf{v}_j(x, \omega) e^{-ikx_1} dx_1 \tag{5.17}$$

Eq. (5.17) is then combined with the system efficiency factor and the reflection coefficient as will be shown in Section 5.3 to generate the FMC signals in the frequency domain.

5.2.3 Angular Spectrum of plane waves

The method of angular spectrum of waves decomposition was first proposed by Goodman [17]. According to the method, a finite beam from a transducer can be decomposed using Fourier decomposition into infinite number of plane waves with different angles of propagation in the spatial frequency domain. The angular spectrum method can be carried out by using the Discrete Fourier Transform to transform from wavenumber domain to the spatial domain. The angular decomposition is given by the below equation

$$F(x_1, x_2) = \int_{-\infty}^{+\infty} \int_{-\infty}^{+\infty} f(k_{x_1}, k_{x_2}) e^{-i(k_{x_1}x_1 + k_{x_2}x_2 + k_{x_3}x_3)} dk_{x_1} dk_{x_2} \quad (5.18)$$

Where $f(k_{x_1}, k_{x_2})$ is the acoustic wave field at the face of the transducer in the wavenumber domain and $F(x_1, x_2)$ is the acoustic wavefield in the spatial domain. k_{x_1} and k_{x_2} are the wavenumber components in the plane normal to plane of propagation of the wave. For 2-D inspection, the wavenumber in the x_2 direction can be considered as 0 and Eq. (5.18) simplifies to the equation given below

$$F(x_1, 0) = \int_{-\infty}^{+\infty} f(k_{x_1}, 0) e^{-i(k_{x_1}x_1 + k_{x_3}x_3)} dk_{x_1} \quad (5.19)$$

Hence Eq. (5.19) can then be used to generate the frequency domain received signal as will be shown in Section 5.3

5.3. Development of a model to simulate the FMC signals

For modelling the array signals from a Gaussian beam transducer, I combine the multi Gaussian beam model for the transducer elements from Eq. (5.17) with the response of the layered material using the stiffness matrix approach from Eq. (5.12) as given below

$$F(x_1, 0) = \int_{-\infty}^{+\infty} v_j(k_{x_1}, 0) \beta(\omega) R(k_{x_1}, 0) e^{-i(k_{x_1}x_1 + k_{x_3}x_3)} dk_{x_1} \quad (5.20)$$

Where $\beta(\omega)$ is the combined system function for a pair of transducer and receiver elements, $R(k_{x_1}, 0)$ is the reflection coefficient of the entire structure calculated using Eq. (5.12) and x_l is the distance between j^{th} element and the receiver position.

The system function for an array element can be calculated in the following way as proposed by Schmerr [18].

1. The backwall echo response F_{BWE} for a transducer element from a known material such as aluminium is calculated experimentally.
2. The backwall echo F_{BWA} is then calculated analytically using a simple testing configuration.

It is assumed that the relationship between the experimental and analytical backwall echo is given by Eq. (5.21)

$$F_{BWE} = \beta(\omega)F_{BWA} \quad (5.21)$$

Hence the combined system response between a pair of elements is given below

$$\beta(\omega) = F_{BWE} / F_{BWA} \quad (5.22)$$

The deconvolution process in Eq. (5.22) is carried out by implementing a Weiner Filter to reduce the sensitivity to noise as given below [19]

$$\beta(\omega) = \frac{F_{BWE}(\omega)F_{BWA}^*(\omega)}{\left[|F_{BWA}|^2 + \varepsilon^2 \max\{|F_{BWA}|^2\}\right]}$$

Where * refers to the complex conjugate, ε is a small noise constant. The system function also takes into account the effect of various external parameters such as bandwidth, cabling etc.

It is assumed that the elements are linear, time invariant and identical in frequency response and directivity as those demonstrated by Huang [14]. Hence the combined system response for just one pair of elements is required to characterize the other elements.

5.4. Simulation and Experimental Results

In this section simulation and experimental results will be presented. The calculations were carried out for three transducer arrays of different centre frequencies, array sizes and number of elements.

The experimental FMC signals were acquired using the FI ToolBox from Diagnostic Sonar. The transducers used were phased array transducers supplied by Olympus . The signals were captured using the Diagnostic Toolbox and were imported into MATLAB® for plotting the data. The simulations were carried out using MATLAB 2017®.

Fig 5.2. Shows the transducer array configuration used for the experiments and simulations where 1, 2,.. denote the array element number and n is the total number of array elements.

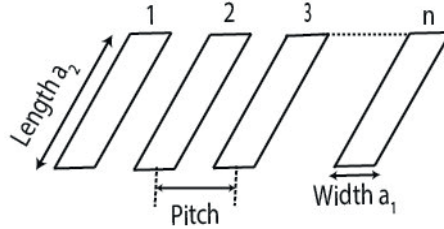


Figure 5.2. Elements of an array transducer.

The specifications of the transducers are shown in the Table 5.1 and were chosen due to their availability in the laboratory

Table 5.1: Transducer Array specifications

	Centre Frequency (MHz)	Pitch (mm)	Number of Elements
Array 1	2.25	1	64
Array 2	5	0.6	16
Array 3	5	1	128

For simulation and experimental purposes I consider an aluminum block 25 mm thick and a CFRP laminate which is quasi isotropic and 19 mm thick with a (0/45/-45/90) layup. There are 169 layers of UniDirectional CFRP prepreg of 110 μm thickness in the laminate with a layer of epoxy resin of thickness 5 μm between them. The properties of Aluminum and unidirectional CFRP lamina[20] are given in the Table 5.2.

Table 5.2: Material Properties [20]

Properties	Aluminum (GPa)	Carbon/Epoxy >65% Fibre-Volume fraction (GPa)
C_{11}	110	13.89(1+0.02i)
C_{22}	110	13.89(1+0.02i)
C_{33}	110	121.7(1+0.001i)
$C_{12}=C_{21}$	60	6.43(1+0.011i)
$C_{13}=C_{31}$	60	5.5(1+0.007i)
$C_{23}=C_{32}$	60	5.5(1+0.007i)
C_{44}	25	5.1(1+0.066i)
C_{55}	25	5.1(1+0.066i)
C_{66}	25	3.73(1+0.027i)

By taking the complex material properties I take into account the attenuation caused due to viscoelasticity in the CFRP lamina. The simulation consists of evaluating the Equations (5.17), (5.22) and then substituting the results in Eq. (5.20).

5.4.1 Total Reflection Coefficient of the materials under inspection

The reflection coefficient was obtained by evaluating Eq. (5.8) for the materials in Table 5.1 at different frequencies and for normal incidence. The reflection coefficients are given in Figure 5.3 (a) and (b)

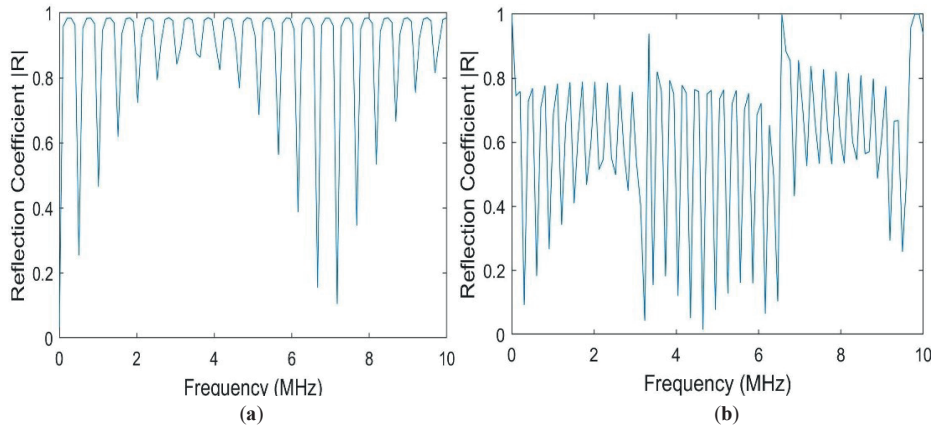


Figure 5.3. (a) Total Reflection coefficient for Aluminum (b) Total Reflection coefficient for CFRP laminate.

Figures 5.3 (a) and (b) show the reflection coefficients for Aluminium and CFRP respectively. The plane wave reflection coefficient is frequency dependent which can be observed in Figure 5. The resonance is characterized with a reflection coefficient of 1 which is observed in Figure 5. At the resonant frequencies the transmission coefficient is 0. The resonant frequencies can also be analytically calculated by the below equation

$$RF = \frac{nc}{2Nh} \quad (5.23)$$

where $n=1,2,3\dots$, c is the velocity of the ultrasonic wave in the material and N is the total number of layers. The resonant frequencies are dependent on the thickness of the material system and velocity of the wave in it. The resonant frequencies calculated using Eq. (5.23) are equal to the resonant frequencies observed by

evaluation of Eq. (5.12). Therefore the reflection coefficients R at various frequencies and wavenumbers can be calculated using the stiffness matrix method and substituted in Eq. (5.20).

5.4.2 System Functions of the transducer arrays

The system function is calculated by using Eq. (5.22). Figures (5.4) and (5.5) show the system functions for elements of centre frequency 2.25 MHz and 5 MHz used for inspection of the aluminum block and the CFRP laminate .

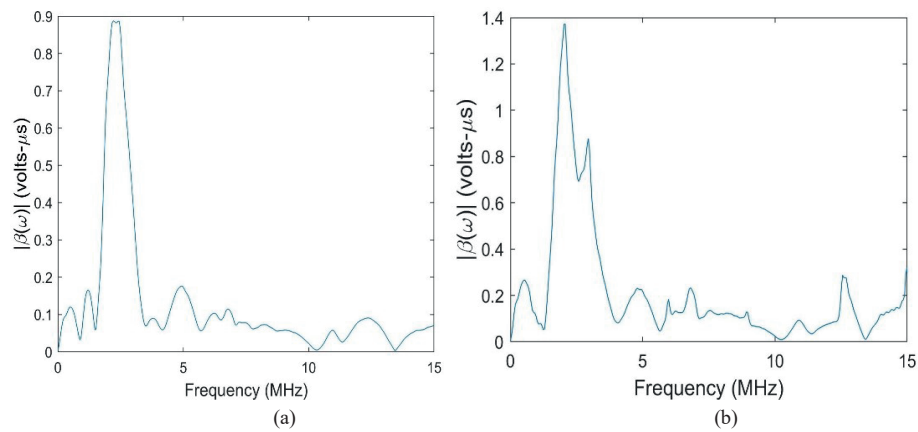


Figure 5.4. System function of pair of elements with centre frequency of 2.25 MHz used for testing (a) Aluminium (b) CFRP laminate

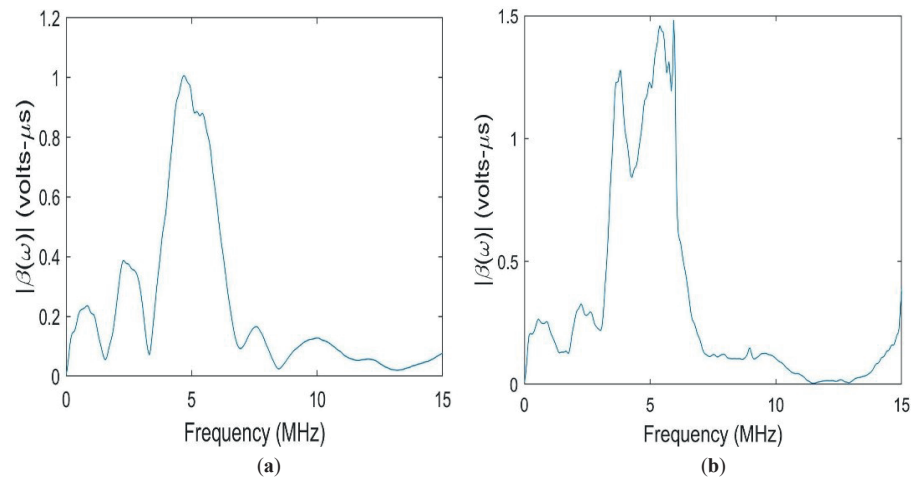


Figure 5.5. System function of a pair of elements with centre frequency of 5 MHz used for testing (a) Aluminium (b) CFRP laminate

In Figures 5.4 and 5.5 it can be observed that the system function peak is at the centre frequency of the transducer and the width of the peak depends on the transducer bandwidth. For narrowband transducers the width of the peak is less than that for wideband transducers.

For the CFRP laminate in Figure 5.4 (b) it is observed that there is another peak close to the central peak. This is attributed to the surface of the CFRP laminate under inspection which can also affect the system function. The system function has to be calculated whenever there is change in central frequency of the transducer or the material under inspection

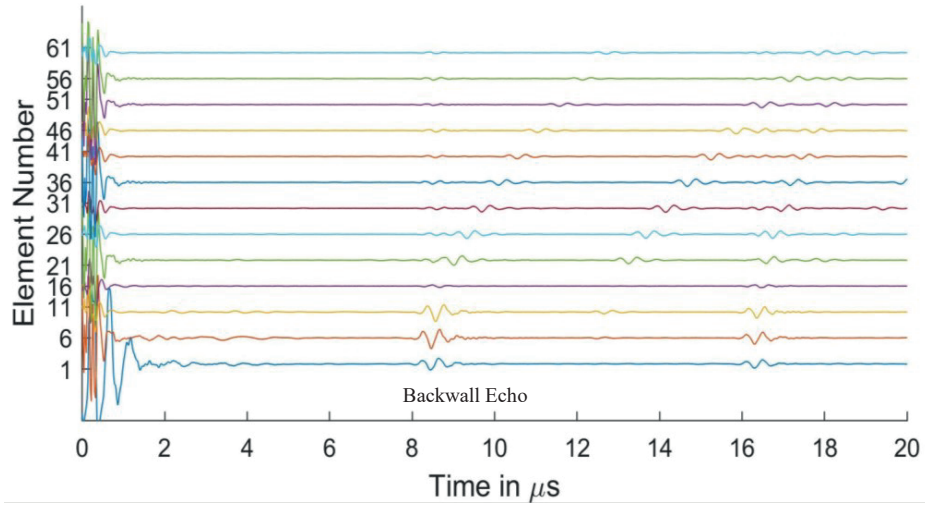
5.4.3 Comparison of experimental and Simulated FMC signals

For the purposes of this chapter, in Figures 5.6, 5.7, 5.8, 5.9 and 5.10 the 1st element, as shown in Figure 5.2, is the transmitting element while the others are receiving elements. Similar figures can be plotted for the other transmitting and receiving elements from the simulated FMC data.

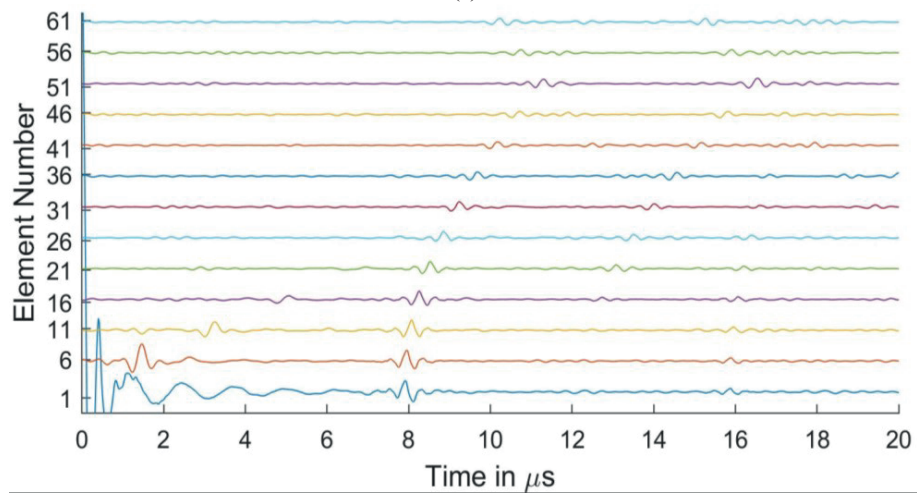
5.4.3.1 Experimental and Simulated FMC signals in Aluminum

Figures 5.6 and 5.7 present the experimental and simulated FMC signals for inspection of aluminum with the Array 1 and Array 2 respectively. In Figures 5.6 and 5.7 the backwall echo can be clearly seen between 8 and 10 μ s. The simulated signals agree with the experimentally determined signals. The front surface reflected signal can be observed at various elements. The slower quasi-shear waves can be seen between 12 and 16 μ s. The second backwall echo is observed at 17 μ s. The signals decrease in amplitude as they move away from the firing element due to material attenuation and the effects of diffraction.

In Figure 5.6(a) a small signal is observed just before 8 μ s. This signal is seen in the experimental result and is missing in the simulation. The signal is a relatively low amplitude signal which can be attributed to small inconsistencies in the experimental aluminum reference block provided by Olympus©. In Figure 5.6 (b) a low amplitude signal can be seen in the simulation results before the backwall echo for elements 56 and 61. These are attributed to the noise signals generated while synthesizing the simulated signals from a high sampling rate which is done so as to correspond with the Nyquist frequency of 50 MHz of the experimental results.

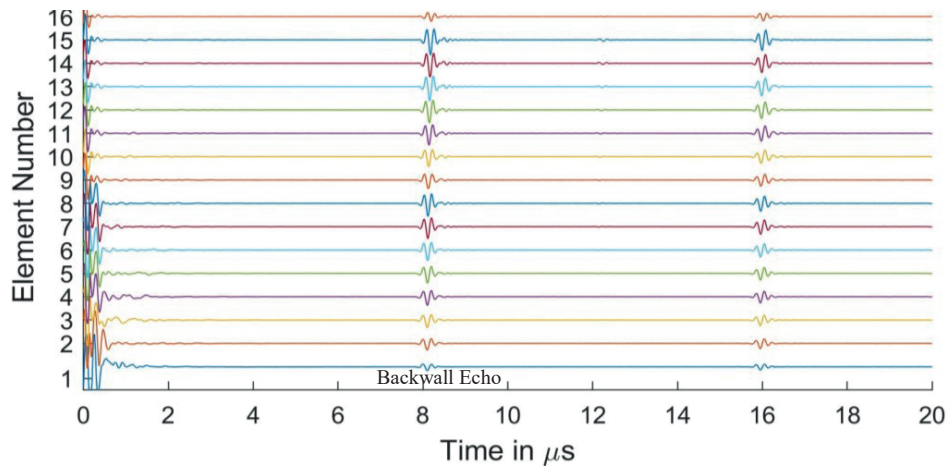


(a)

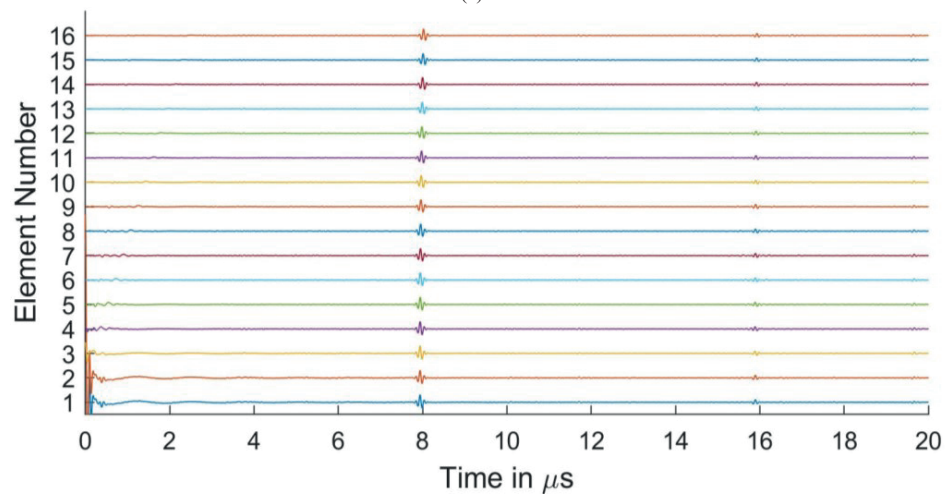


(b)

Figure 5.6. (a) Experimental FMC signals obtained for Aluminium with 2.25 MHz 64 element array
 (b) Simulated FMC signals for Aluminium with 2.25 MHz 64 element array



(a)



(b)

Figure 5.7. (a) Experimental FMC signals obtained for Aluminum with 5 MHz 16 element array (b) Simulated FMC signals for Aluminum with 5 MHz 16 element array

Table 5.3 presents the comparison of the first element backwall amplitude reduction between experimental and simulated results.

Table 5.3: Comparison of backwall amplitude reduction

Frequency (MHz)	Experimental	Simulation
2.25	40.16 dB	39.4 dB
5	10.87 dB	11.28 dB

It can be observed from the table that the amplitude difference between the simulated and the experimental results are less than 2 dB , showing good agreement between the experimental and simulated results. The percentage error between the experimental and simulated results for the 2.25MHz and 5 MHz is calculated to be 1.89% and 3.63% respectively, showing agreement between the simulation and experimental results.

5.4.3.2 Experimental and Simulated Signals in CFRP

Figures 5.8 and 5.9 show the experimental and simulated signals for the CFRP laminate. The amplitude of the backwall echoes are reduced as compared to aluminium due to the increased attenuation of the signals. The reduction of the signals is due to attenuation caused by the viscoelasticity of the lamina, diffraction effects and the scattering of the wave from the ply interfaces. The signals presented for the 64 and 128 elements array are up to element 30 as the elements beyond this do not receive the reflected signal owing to losses as stated above.

Ply resonances can also be observed in the signals. It is also seen that as the centre frequency of the signal increases, the amplitude of the ply resonances and also the scattering from the interfaces increases as seen in Figures 5.8 and 5.9. The slower shear waves cannot be observed due to the increased attenuation of the laminate.

In Figure 5.8(a) for elements 1,3 and 5 signals are observed which occur before the backwall echo. These are missing from the simulated results. This can be attributed to the fact that although the simulation takes the layer attenuation and reflections into consideration, the layers in the manufactured material are not of equal thicknesses and might have pockets of resin and other small defects which influence the signal.

Further in the simulated signals of Figure 5.8 (b) and Figure 5.10 (b), low amplitude signals can be observed at 20 μ s. These low amplitude signals arise as the sampling rate is high to avoid aliasing and hence leads to the computation of a large number of frequencies. Due to this when the inverse Fourier transform is carried out, the time window is longer than 20 μ s and contains noise generated due to the large number of sampling frequencies. As the output signals are cut at 20 μ s for comparison with the experimental results, some of these low amplitude noisy signals are seen.

As a comparison of the effect of the element pitch on the FMC signals, Array 3 is used to inspect the CFRP laminate. In Figure 5.10 the increased pitch and element width of Array 3 show less resonance from the plies as compared to Figure

5.9. This shows one of the ways the simulation model can be used to optimize the array parameters for different thickness and material properties.

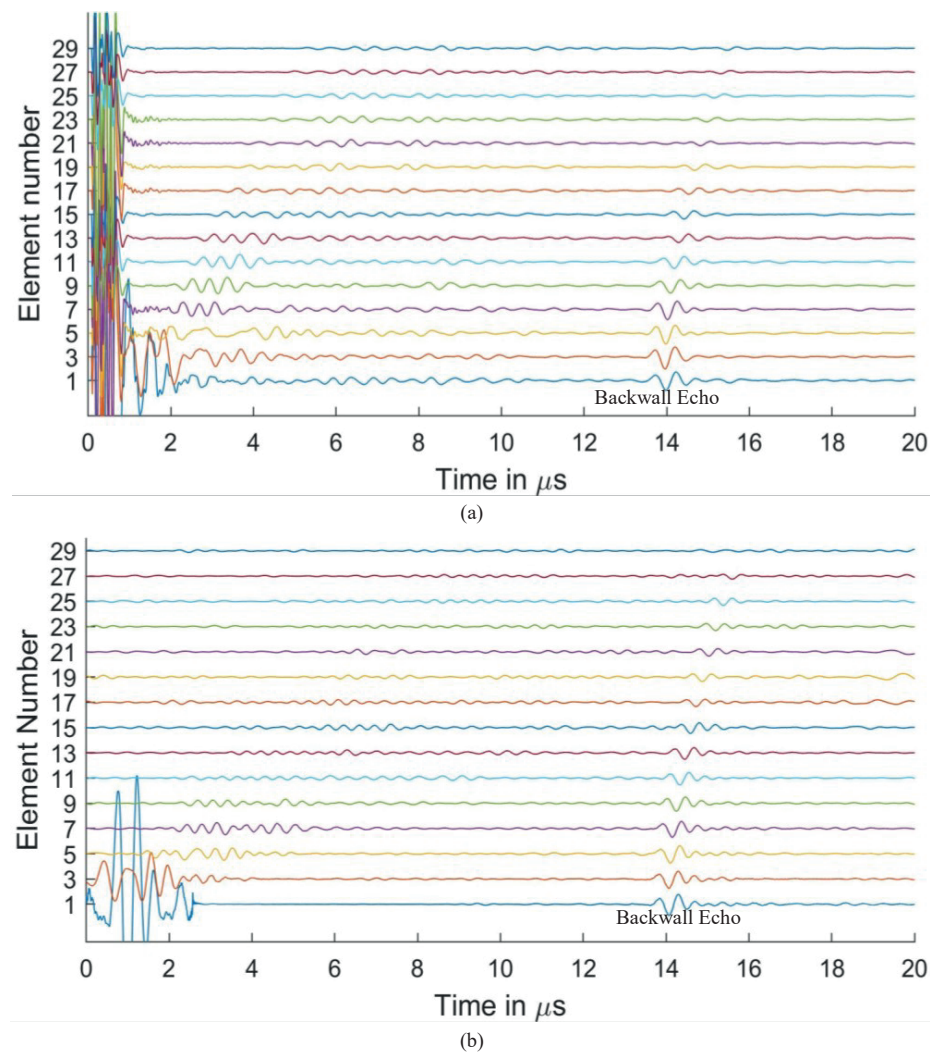
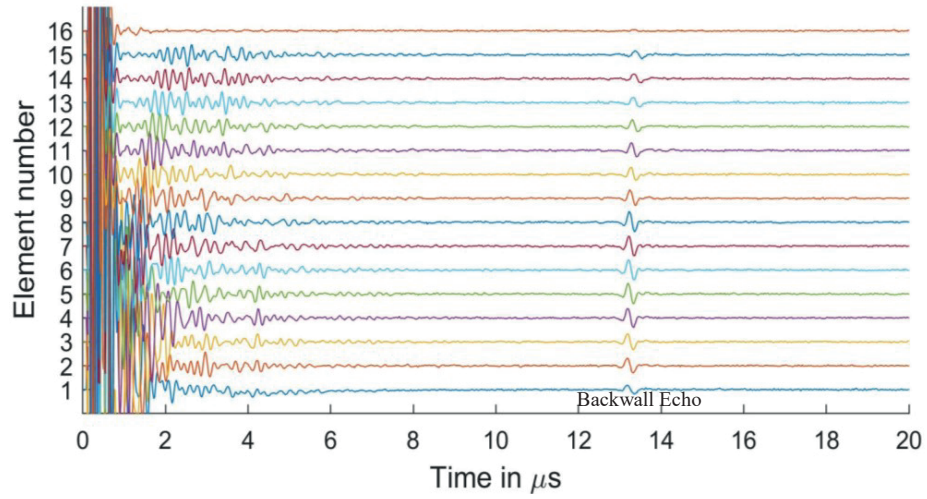
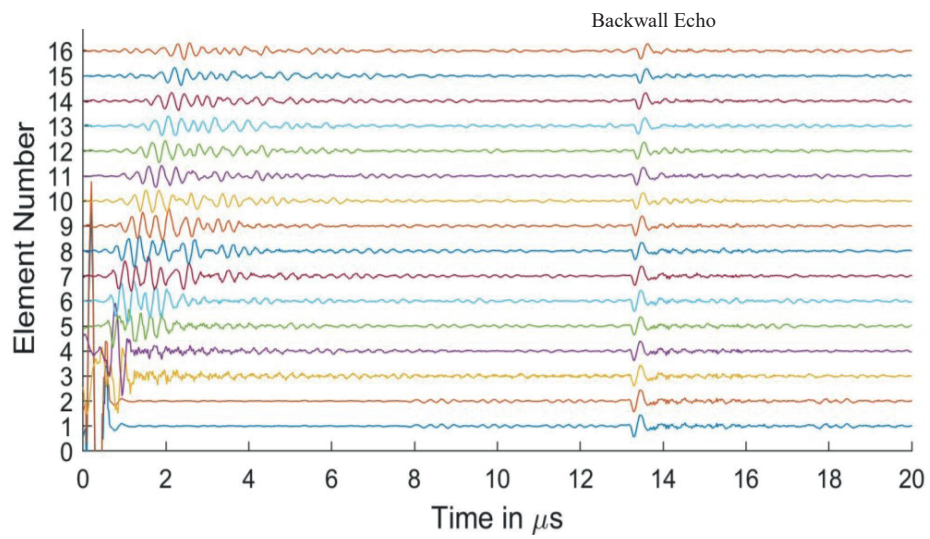


Figure 5.8. (a) Experimental FMC signals obtained for CFRP with 2.25 MHz 64 element array (b) Simulated FMC signals for CFRP with 2.25 MHz 64 element array

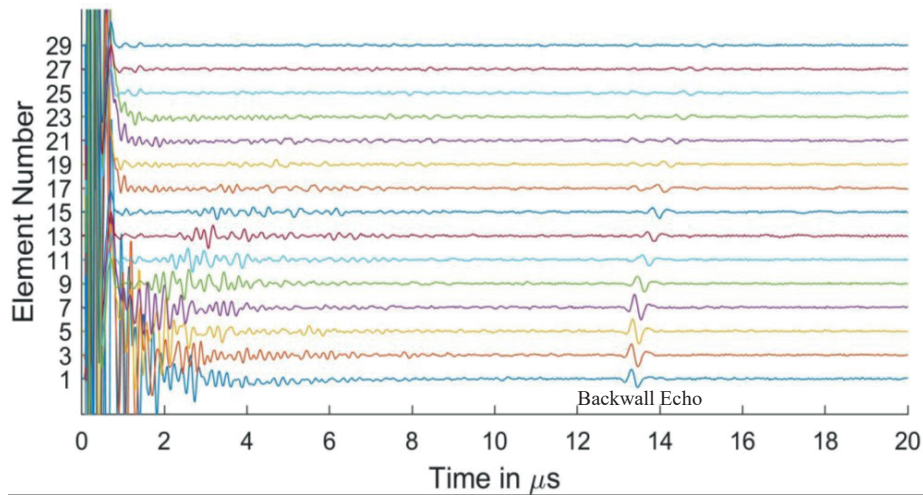


(a)

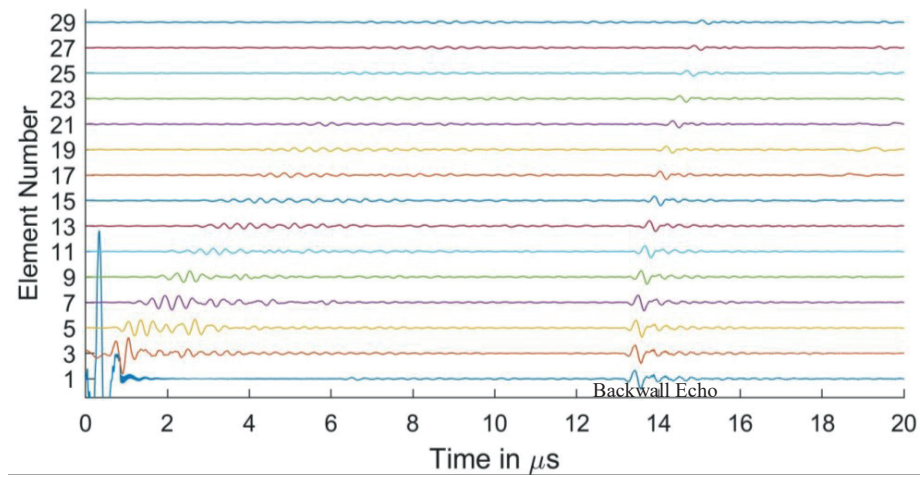


(b)

Figure 5.9 (a) Experimental FMC signals obtained for CFRP with 5 MHz 16 element array (b) Simulated FMC signals for CFRP with 5 MHz 16 element array



(a)



(b)

Figure 5.10. (a) Experimental FMC signals obtained for CFRP with 5 MHz 128 element array (b) Simulated FMC signals for CFRP with 5 MHz 128 element array

It can be observed that the experimental front wall echo consists of noise and hence is not suitable for comparison between the experimental and simulated results. Hence Table 5.4 presents the difference of 1st and 3rd element backwall amplitude, between experimental and simulated results.

Table 5.4: Comparison of backwall echo difference between experimental and simulated results

Frequency	Experimental	Simulation
2.25	5.82 dB	5.5 dB 5.5%
5	6.9 dB	7 dB 1.43%

It can be observed from the table that the difference between the reduced amplitude between the simulated and the experimental results is less than 1 dB, showing good agreement between the results. The percentage error between the experimental and simulated results for the 2.25 MHz and 5 MHz is calculated to be 5.5% and 1.43% respectively, showing agreement between the simulation and experimental results.

5.5. Discussions

As shown in Figure 5.3 the stiffness matrix method predicts the reflection coefficient and the resonant frequency of the system under inspection. This can help in determining the resonant frequency of the material under inspection and hence lead to a better choice of inspection as at resonant frequencies the wave undergoes total reflection leading to no penetration of the material.

Figures 5.6, 5.7, 5.8 and 5.9 show that the proposed modelling techniques to simulate the received FMC signals are in good agreement to the experimental results is also shown by Table 5.3 and Table 5.4 which have percentage errors of less than 6% between the results. Slight discrepancies are noted in the experimental and simulated results. As discussed these discrepancies arise due to the different ultrasonic velocities used in the simulation and in the experimental acquisition owing to slightly different material properties of the experimental and simulated samples. Low amplitude noise is also present in the simulated results which is due to the signal being synthesised from a large number of frequencies.

The thickness of the couplant used and its properties also influence the time of flight as in the simulation the laminate is surrounded by water bounding layers of infinite thickness whereas in the experimental scenario the couplant gel layer has a finite thickness and a slightly different wave velocity. As discussed in Section 5.2 water bounding layers are assumed due to the fact that only longitudinal waves can travel through water, hence only incident longitudinal waves need to be considered entering the material under inspection. Due to this the number of unknowns reduces in Eq. (5.6), enabling us to solve 6 equations for 6 unknowns.

The extensive electrical response of array elements is missing in the simulated results but the computation of the system response by using the backwall method captures the other salient frequency response of the array elements. The frequency responses are observed to be not precisely Gaussian in shape due to different varying factors such as the electronic components of the setup, the top surface of the material inspected, thickness of couplant, etc.

The trend of the diminishing backwall echos as we move further away from the transmitting element is identical for both the experimental and the simulated results. In Figures 5.8, 5.9 and 5.10 we can observe the reverberations from the layers in the simulated results which agree with the experimental results. These reverberations tend to contribute to the noise of the signal and hence the ability of the modelling technique to simulate these for the material under inspection can help in optimising the array parameters without extensive experimental analysis. The slight discrepancy in the results of the CFRP laminate can be attributed to the slightly varying thickness of layers and resin in the manufactured laminate as in the simulation it is assumed that the layers are of constant thickness and parallel to each other. Figures 5.9 and 5.10 also provide a comparison between the array signals received due to different element sizes and pitch which influence the received FMC signals.

5.6. Conclusions

The chapter proposes a Gaussian beam and recursive stiffness matrix based modelling techniques to model the FMC signals from layered CFRP laminates. The simulated signals have good agreement, to within 2 dB and a percentage error of less than 6%, with the experimental signals, and are able to simulate the various different components of the experimental signal which include ply resonances, front wall reflection, back wall echos and also the backwall echos from the slower shear waves. The proposed model takes into account the diffraction effects caused by Gaussian beams and mimics the real world scenario where the transducer emits Gaussian shaped beams. It is also shown how the model can be used to optimize various parameters of the inspection process. The model can be used for both isotropic and anisotropic layered media, where the anisotropic group velocity is taken into account.

In the next chapter I will modify the developed model to represent a CFRP laminate bounded by an anisotropic bounding medium instead of water. The developed model is then integrated with a scattering model to simulate scattering from a side drilled hole (SDH) embedded in the CFRP laminate. Time domain and Frequency domain imaging algorithms are applied to image the SDH using the

developed model and validated experimentally. A comparison of the imaging algorithm performance and the effect of parameters and material properties is also discussed.

5.7 References

- [1] C. Soutis, *Introduction: Engineering requirements for aerospace composite materials*. Elsevier Ltd, 2014.
- [2] A. Quilter, "Composites in Aerospace Applications," *Inf. Handl. Serv. Inc.*, 2004.
- [3] O. I.-2nd Isaac M. Daniel, "Engineering mechanics of composite materials," *Materials & Design*. 2006.
- [4] D. Gay, S. V. Hoa, and S. W. Tsai, *Composite materials: Design and applications*. 2002.
- [5] S. C. Hong, J. R. Lee, and J. B. Ihn, "In-situ NDE of composite repair patch and thick panel with substructures using mobile pulse-echo ultrasonic propagation imager," *Struct. Heal. Monit. 2017 Real-Time Mater. State Aware. Data-Driven Saf. Assur. - Proc. 11th Int. Work. Struct. Heal. Monit. IWSHM 2017*, vol. 2, pp. 2260–2267, 2017, doi: 10.12783/shm2017/14118.
- [6] M. E. Ibrahim, "Nondestructive evaluation of thick-section composites and sandwich structures: A review," *Compos. Part A Appl. Sci. Manuf.*, vol. 64, pp. 36–48, 2014, doi: 10.1016/j.compositesa.2014.04.010.
- [7] G. F. Hawkins, P. M. Sheaffer, and E. C. Johnson, "NDE of Thick Composites in the Aerospace Industry — An Overview," in *Review of Progress in Quantitative Nondestructive Evaluation*, 1991.
- [8] J. H. Heida, J. P. Derk, "Evaluation of non-destructive inspection methods for composite aerospace structures," *6th NDT Prog. 2011*, pp. 1–12, 2011, [Online]. Available: http://www.ndt.net/article/ndtp2011/papers/1_Heida.pdf.
- [9] S. I. Rokhlin, D. E. Chimenti, and P. B. Nagy, *Physical ultrasonics of composites*. Oxford University Press, 2011.
- [10] F. Hron, B. T. May, J. D. Covey, and P. F. Daley, "Synthetic seismic sections for acoustic, elastic, anisotropic, and vertically inhomogeneous layered media.," *Geophysics*, vol. 51, no. 3, pp. 710–735, 1986, doi: 10.1190/1.1442124.
- [11] S. I. Rokhlin and L. Wang, "Ultrasonic waves in layered anisotropic media: Characterization of multidirectional composites," *Int. J. Solids Struct.*, 2002, doi: 10.1016/S0020-7683(02)00500-0.
- [12] A. H. Nayfeh, "The general problem of elastic wave propagation in multilayered anisotropic media," *J. Acoust. Soc. Am.*, 1991, doi: 10.1121/1.400988.
- [13] S. I. Rokhlin and L. Wang, "Stable recursive algorithm for elastic wave propagation in layered anisotropic media: Stiffness matrix method," *J. Acoust. Soc. Am.*, 2002, doi: 10.1121/1.1497365.
- [14] R. Huang, L. W. Schmerr, and A. Sedov, "Modeling the radiation of ultrasonic phased-array transducers with Gaussian beams.," *IEEE Trans. Ultrason. Ferroelectr. Freq. Control*, vol. 55, no. 12, pp. 2692–702, 2008, doi: 10.1109/TUFFC.2008.984.
- [15] J. J. Wen and M. A. Breazeale, "A diffraction beam field expressed as the superposition of Gaussian beams," *J. Acoust. Soc. Am.*, vol. 83, no. 5, pp. 1752–1756, 1988, doi: 10.1121/1.396508.
- [16] D. Ding, Y. Zhang, and J. Liu, "Some extensions of the Gaussian beam expansion: Radiation

- fields of the rectangular and the elliptical transducer,” *J. Acoust. Soc. Am.*, vol. 113, no. 6, p. 3043, 2003, doi: 10.1121/1.1572144.
- [17] J. W. Goodman, “Introduction to Fourier Optics, 2nd ed.,” *Quantum Semiclassical Opt. J. Eur. Opt. Soc. Part B*, vol. 8, no. 5, p. 491, 1996, doi: 10.1088/1355-5111/8/5/014.
- [18] L. W. Schmerr, *Fundamentals of Ultrasonic Phased Arrays*, vol. 215, no. May 2003. Cham: Springer International Publishing, 2015.
- [19] L. W. Schmerr, *Fundamentals of Ultrasonic Nondestructive Evaluation A Modeling Approach Second Edition*. 2016.
- [20] B. Hosten and M. Castaings, “Transfer matrix of multilayered absorbing and anisotropic media. Measurements and simulations of ultrasonic wave propagation through composite materials,” *J. Acoust. Soc. Am.*, 1993, doi: 10.1121/1.408152.

6

Modelling the scattering from a side drilled hole embedded in a layered anisotropic medium

Abstract

This chapter proposes a modelling technique to simulate the scattering from a side drilled hole (SDH) embedded in a multilayered anisotropic medium. The chapter provides a novel method to calculate the transmission and reflection coefficients of plane waves traveling from layered anisotropic medium into semi-infinite anisotropic medium by combining the transfer matrix and stiffness matrix methods. The chapter describes a method to combine the scattering from defects with the model to simulate the response of a layered structure to simulate the Full matrix capture (FMC) signals which are received from a SDH embedded in a layered medium. Model assisted corrected total focusing method (TFM) imaging is used to image both the simulated and experimental results. The proposed method is validated for both isotropic and anisotropic media by a qualitative and quantitative comparison with experimentally determined signals. The method proposed in the chapter is modular, computationally inexpensive and is in good agreement with experimentally determined signals and enables us to understand the effects of various parameters on the scattering of a defect embedded in a layered anisotropic medium.

Adapted from: C. Anand, R. Groves, R. Benedictus, Modeling the scattering from a side drilled hole embedded in a layered anisotropic medium, Sensors 2021

6.1. Introduction

In the previous chapter I developed a Gaussian beam based recursive stiffness matrix model to simulate the received signals while inspecting a CFRP laminate using an ultrasonic phased array. One of the preliminary assumptions of the model was that the multilayered laminate is bounded by a semi-infinite water layer, allowing only longitudinal waves to impinge onto the composite laminate and thereby reducing the number of unknowns [1]. To simulate the scattering response of defects embedded within the laminate the assumption of water bounding layers is invalid as the defect is surrounded by a homogeneous isotropic or anisotropic elastic medium as seen in Section 5.2.2. To address this limitation, in this chapter, I provide a method to calculate the reflection and transmission coefficients for a multilayered laminate bounded by a semi-infinite anisotropic medium. For a layered structure such as quasi-isotropic CFRP laminate which has a repeated set of layers of different orientations, the lower bounded medium can be modeled as an equivalent homogeneous anisotropic medium [2].

Defects such as side drilled holes (SDH) are commonly used as reference defects for ultrasonic phased array testing [3]. In this chapter I will develop a model to simulate the scattering from an SDH which is embedded in a layered CFRP laminate. The model simulates the received FMC signals from the scattering of an SDH and the modified TFM algorithm is used to image the defect from FMC signals generated from simulations and experimentally. The next section provides the background theory used for modelling the scattering from an SDH in a layered anisotropic medium.

6.2. Background Theory

The following sections give a brief description of the transfer-matrix method which is similar to the stiffness-matrix method of the previous chapter. An understanding of the transfer matrix method is required as it forms the basis for the matrix formulation of the Transmission/Reflection of plane waves from layered media from/into a generally anisotropic semi-infinite medium.

6.2.1 Transfer Matrix method

The transfer matrix gives a relationship between the stress and displacements at the top of a layer m to the stress and displacements at the bottom of the layer as shown in the general equation

$$\begin{bmatrix} \mathbf{u}^m(0) \\ \boldsymbol{\sigma}^m(0) \end{bmatrix} = \mathbf{B} \begin{bmatrix} \mathbf{u}^m(h_m) \\ \boldsymbol{\sigma}^m(h_m) \end{bmatrix} \quad (6.1)$$

Where B is the transfer matrix of the layer.

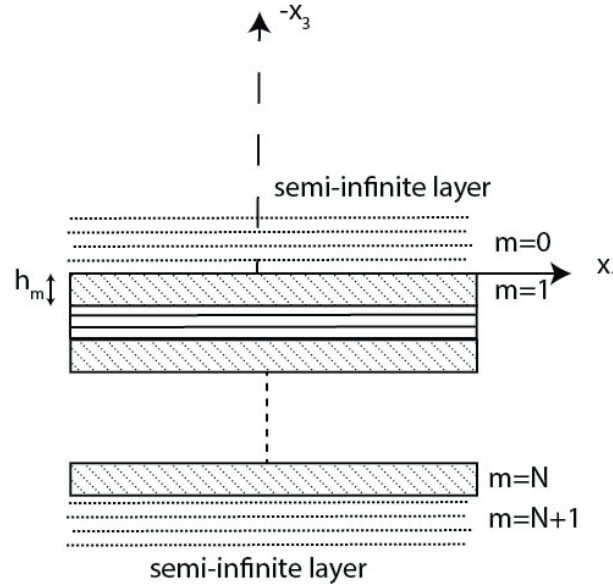


Figure 6.1. Schematic diagram of a laminate of N layers bounded by a semi-infinite medium.

From Section 5.2.1 we know that the displacement in the layer m is given by the below equation

$$u_i^m = \sum_{p=1}^3 \left(a^{m,p+} d_i^{m,p+} e^{ik_3^{m,p+}(x_3-x_3^m)} + a^{m,p-} d_i^{m,p-} e^{-ik_3^{m,p-}(x_3-x_3^m)} \right) e^{i(k_1x_1+k_2x_2-\omega t)} \quad (6.2)$$

Where a is the amplitude of the wave of type p (p =quasi longitudinal, quasi horizontal shear, quasi vertical shear), d is the polarization vector, m is the layer, k_l is the wavenumber along the x_l axis, ω is the angular frequency.

The relationship between stress and displacement is given in Eq. (6.3)

$$\sigma_{ij} = \frac{1}{2} c_{ijkl} \left(\frac{\partial u_k}{\partial x_l} - \frac{\partial u_l}{\partial x_k} \right) \quad (6.3)$$

Where $\boldsymbol{\sigma}$ is the stress, u is the displacement, c_{ijkl} is the stiffness tensor ($i=j=k=l=1,2,3$)

Substituting Eq. (6.2) in Eq. (6.1) and rearranging the displacement and stress at the top surface of the layer m is given by Eq. (6.4)

$$\begin{bmatrix} \mathbf{u}^m(0) \\ \boldsymbol{\sigma}^m(0) \end{bmatrix} = \begin{bmatrix} \mathbf{D}^+ & \mathbf{D}^-\mathbf{H}^- \\ \mathbf{F}^+ & \mathbf{F}^-\mathbf{H}^- \end{bmatrix} \begin{bmatrix} \mathbf{A}^{m+} \\ \mathbf{A}^{m-} \end{bmatrix} \quad (6.4)$$

And at the bottom surface of layer m by Eq. (6.5)

$$\begin{bmatrix} \mathbf{u}^m(h_m) \\ \boldsymbol{\sigma}^m(h_m) \end{bmatrix} = \begin{bmatrix} \mathbf{D}^+\mathbf{H}^+ & \mathbf{D}^- \\ \mathbf{F}^+\mathbf{H}^+ & \mathbf{F}^- \end{bmatrix} \begin{bmatrix} \mathbf{A}^{m+} \\ \mathbf{A}^{m-} \end{bmatrix} \quad (6.5)$$

Relating the displacements and stress from the top and bottom of the layer m

$$\begin{bmatrix} \mathbf{u}^m(0) \\ \boldsymbol{\sigma}^m(0) \end{bmatrix} = \mathbf{B}_m \begin{bmatrix} \mathbf{u}^m(h_m) \\ \boldsymbol{\sigma}^m(h_m) \end{bmatrix} \quad (6.6)$$

Where B_m is the layer transfer matrix between the top surface and bottom surface of layer m which is given by equation

$$\mathbf{B}_m = \begin{bmatrix} \mathbf{D}^+\mathbf{H}^+ & \mathbf{D}^- \\ \mathbf{F}^+\mathbf{H}^+ & \mathbf{F}^- \end{bmatrix} \begin{bmatrix} \mathbf{D}^+ & \mathbf{D}^-\mathbf{H}^- \\ \mathbf{F}^+ & \mathbf{F}^-\mathbf{H}^- \end{bmatrix}^{-1} \quad (6.7)$$

Where F, D and H are defined in Section 5.2.1

6.2.2 Equivalent homogeneous anisotropic properties of a thick laminate

When a layered composite laminate such as CFRP with repeated layers is tested at lower frequencies i.e. longer wavelengths where the thickness of the plies is less than the wavelength of wave, the reflections from the ply interfaces are negligible and have no effect on the propagation of the wave [4]. In such a scenario the laminate can be considered to have equivalent homogenous properties which can be used for calculating the group velocity of the laminate, and for imaging purposes etc. Many methods have been investigated to calculate the equivalent homogeneous properties. For this work I chose the method described by Sun and Li [2] as it gives explicit relations to find the homogeneous anisotropic properties.

Classical laminate theory is used for characterizing thin laminates [5]. For thick laminates higher order plate theories are used which are more mathematically complex [6]. In thick laminates with periodic stacking layers where the characteristic length of deformation of the laminate is larger than the periodicity, the non-homogeneous properties over each typical cell can be replaced by effective properties [7]. Thus each cell of a laminate can be represented as a homogeneous anisotropic solid. Sun and Li considered a thick laminate consisting of repeated sub laminates where the thickness of sub laminates is small as compared to the thickness of the entire laminate. The sub laminate is then evaluated using constant stress and strain assumptions and the effective homogeneous properties of the entire laminate are calculated. The explicit expressions to calculate the effective homogeneous properties are given below where C is the stiffness tensor in Voigt notation [8]

$$\overline{C}_{11} = \sum_{m=1}^N h_m C_{11}^m + \sum_{m=2}^N h_m (C_{13}^m - \lambda_{13}) (C_{13}^1 - C_{13}^m) / C_{33}^m \quad (6.8)$$

$$\overline{C}_{12} = \sum_{m=1}^N h_m C_{12}^m + \sum_{m=2}^N h_m (C_{13}^m - \lambda_{13}) (C_{23}^1 - C_{23}^m) / C_{33}^m \quad (6.9)$$

$$\overline{C}_{13} = \sum_{m=1}^N h_m C_{13}^m + \sum_{m=2}^N h_m (C_{33}^m - \lambda_{33}) (C_{13}^1 - C_{13}^m) / C_{33}^m \quad (6.10)$$

$$\overline{C}_{22} = \sum_{m=1}^N h_m C_{22}^m + \sum_{m=2}^N h_m (C_{23}^m - \lambda_{23}) (C_{23}^1 - C_{23}^m) / C_{33}^m \quad (6.11)$$

$$\overline{C}_{23} = \sum_{m=1}^N h_m C_{23}^m + \sum_{m=2}^N h_m (C_{33}^m - \lambda_{33}) (C_{23}^1 - C_{23}^m) / C_{33}^m \quad (6.12)$$

$$\overline{C}_{33} = 1 / \sum_{m=1}^N h_m / C_{33}^m \quad (6.13)$$

$$\overline{C}_{16} = \sum_{m=1}^N h_m C_{16}^m + \sum_{m=2}^N h_m (C_{13}^m - \lambda_{13}) (C_{36}^1 - C_{36}^m) / C_{33}^m \quad (6.14)$$

$$\overline{C}_{26} = \sum_{m=1}^N h_m C_{26}^m + \sum_{m=2}^N h_m (C_{23}^m - \lambda_{23}) (C_{36}^1 - C_{36}^m) / C_{33}^m \quad (6.15)$$

$$\overline{C}_{36} = \sum_{m=1}^N h_m C_{36}^m + \sum_{m=2}^N h_m (C_{33}^m - \lambda_{33}) (C_{36}^1 - C_{36}^m) / C_{33}^m \quad (6.16)$$

$$\overline{C}_{66} = \sum_{m=1}^N h_m C_{66}^m + \sum_{m=2}^N h_m (C_{36}^m - \lambda_{36}) (C_{36}^1 - C_{36}^m) / C_{33}^m \quad (6.17)$$

$$\overline{C}_{44} = \left(\sum_{m=1}^N h_m C_{44}^m / \Delta_m \right) / \Delta \quad (6.18)$$

$$\overline{C_{45}} = \left(\sum_{m=1}^N h_m C_{45}^m / \Delta_m \right) / \Delta \quad (6.19)$$

$$\overline{C_{55}} = \left(\sum_{m=1}^N h_m C_{55}^m / \Delta_m \right) / \Delta \quad (6.20)$$

Where h_m is the thickness of the ply and

$$\lambda_{13} = \overline{C_{13}}, \lambda_{23} = \overline{C_{23}}, \lambda_{33} = \overline{C_{33}}, \lambda_{36} = \overline{C_{36}}$$

$$\Delta = \left(\sum_{k=1}^N \frac{h_m C_{44}^m}{\Delta_m} \right) \left(\sum_{k=1}^N \frac{h_m C_{55}^m}{\Delta_m} \right) - \left(\sum_{k=1}^N \frac{h_m C_{45}^m}{\Delta_m} \right)^2 \quad (6.21)$$

$$\Delta_m = C_{44}^m C_{55}^m - (C_{45}^m)^2 \quad (6.22)$$

These effective homogenized anisotropic elastic constants are then used in section 6.3.1 for calculating the transmission coefficient from layered medium into homogenized anisotropic media in which the side drilled hole is embedded. These effective elastic constants are also used in Section 6.3.2 and Section 6.3.3 to calculate the group velocity which is used to calculate the scattering of the side drilled hole and also used to calculate the angle dependent velocity for the total focusing method algorithm.

The next section describes the method to calculate the scattering from a side drilled hole.

6.2.3 Scattering coefficient of a side drilled hole (SDH)

Side drilled holes are the reference reflectors which are used in ultrasonic nondestructive testing [9]. As Side drilled holes have a simple geometry, the exact scattering from it can be calculated using the method of separation of variables [10]. The Kirchoff approximation could also be used to describe the scattering from a SDH but is a far field and high frequency approximation where the size of the hole is much larger than the wavelength of the inspecting wave. Many defects of importance such as voids, porosity etc are smaller than the incident wavelength and hence Kirchoff scattering is not a good choice in such cases. Hence for this thesis the scattering coefficient is evaluated using the method of separation of variables [10] which is given in the below equations, where $A(\omega)$ is the dimensionless scattering coefficient obtained by solving the scattering integral using the method of separation of variables as the scatterer has a simple geometrical shape

$$A_{scatt}(\omega) = \frac{1}{L} \sqrt{\frac{2i}{\pi k_p}} \sum_{n=0}^{\infty} (2 - \delta_{0n}) M_n(k_a b) \cos(n\theta) e_r \quad (6.23)$$

$$M_n = \frac{i}{2k_p b} \left\{ 1 + \frac{C_n^{(2)}(k_p b) C_n^{(1)}(k_s b) - D_n^{(2)}(k_p b) D_n^{(1)}(k_s b)}{C_n^{(1)}(k_p b) C_n^{(1)}(k_s b) - D_n^{(1)}(k_p b) D_n^{(1)}(k_s b)} \right\} \quad (6.24)$$

$$C_n^{(i)}(x) = (n^2 + n - (k_s b)^2 / 2) H_n^{(i)}(x) - x H_{n-1}^{(i)}(x) \quad (6.25)$$

$$D_n^{(i)}(x) = (n^2 + n) H_n^{(i)}(x) - n x H_{n-1}^{(i)}(x) \quad (6.26)$$

Where H is the hankel function and $i=0,1$ corresponds to the order of the Hankel function, L is the length of the Side drilled hole, θ is the angle between the angle of incidence and angle of scattering, b is the radius of the Side drilled hole, δ is the Kronecker delta and e_r is the unit vector of the receiving transducer.

For the pulse echo response of a Side drilled hole embedded in anisotropic materials Huang suggested that the scattering of the SDH is the same as that of an Side drilled hole embedded in an isotropic medium for a particular angle of incidence [11]. Hence for a particular angle of incidence I consider the equivalent homogeneous anisotropic medium as isotropic and calculate the properties at that particular angle of propagation.

6.3. Development of a model to facilitate scattering of Side drilled hole in an layered anisotropic medium

This section provides the steps required to develop a model to simulate the scattering from a SDH which is embedded in an layered anisotropic medium and to post process the Full Matrix Capture signals using model assisted corrected Total focusing method.

6.3.1 Reflection and Transmission coefficients of layered structure bounded by anisotropic media

In this section I derive the equations for the reflection and transmission coefficients for a layered medium bounded by semi-infinite anisotropic media

The reflection and transmission coefficients are derived by combining the transfer matrix method and the stiffness matrix method.

Consider the upper semi-infinite layer 0 as shown in Figure 6.1 where $A^{\text{reflected}}$ is the amplitude of the wave reflected from the layered structure, A^{incident} is the amplitude of the downward moving incident wave. Then from Eq. (6.3) we get

$$\begin{bmatrix} \mathbf{u}^1(0) \\ \boldsymbol{\sigma}^1(0) \end{bmatrix} = \begin{bmatrix} \mathbf{D}^+ & \mathbf{D}^-\mathbf{H}^- \\ \mathbf{F}^+ & \mathbf{F}^-\mathbf{H}^- \end{bmatrix} \begin{bmatrix} \mathbf{A}^{incident} \\ \mathbf{A}^{reflected} \end{bmatrix} \quad (6.27)$$

\mathbf{H} can be removed from the above equation as it controls the decay of the wave of complex wavenumbers in a finite thickness of the material and as I am interested in just the semi-infinite layer, there is no decay due to this term.

$$\begin{bmatrix} \mathbf{u}^1(0) \\ \boldsymbol{\sigma}^1(0) \end{bmatrix} = \begin{bmatrix} \mathbf{D}^+ & \mathbf{D}^- \\ \mathbf{F}^+ & \mathbf{F}^- \end{bmatrix} \begin{bmatrix} \mathbf{A}^{incident} \\ \mathbf{A}^{reflected} \end{bmatrix} \quad (6.28)$$

After matrix manipulation of Eq. (6.29) I get the below equation

$$\begin{bmatrix} \mathbf{u}^1(0) \\ \boldsymbol{\sigma}^1(0) \end{bmatrix} = \begin{bmatrix} \mathbf{D}^+ \\ \mathbf{F}^+ \end{bmatrix} [\mathbf{A}^{incident}] + \begin{bmatrix} \mathbf{D}^- \\ \mathbf{F}^- \end{bmatrix} [\mathbf{A}^{reflected}] \quad (6.29)$$

At the N^{th} layer where $m=N$ before the lower semi-infinite anisotropic medium we have the equation as shown in Eq. (6.30)

$$\begin{bmatrix} \mathbf{u}^m(h_m) \\ \boldsymbol{\sigma}^m(h_m) \end{bmatrix} = \begin{bmatrix} \mathbf{D}^+\mathbf{H}^+ & \mathbf{D}^- \\ \mathbf{F}^+\mathbf{H}^+ & \mathbf{F}^- \end{bmatrix} \begin{bmatrix} \mathbf{A}^{transmitted} \\ \mathbf{A}^{reflected} \end{bmatrix} \quad (6.30)$$

There is no reflected upward travelling wave in the lower semi-infinite medium due to no reflection boundary being present, so

$$\mathbf{A}^{reflected} = 0 \quad (6.31)$$

Eq. (6.32) can then be written as shown below

$$\begin{bmatrix} \mathbf{u}^m(h_m) \\ \boldsymbol{\sigma}^m(h_m) \end{bmatrix} = \begin{bmatrix} \mathbf{D}^+ \\ \mathbf{F}^+ \end{bmatrix} [\mathbf{A}^{transmitted}] \quad (6.32)$$

We also know the stiffness matrix formulation in Chapter 5 (Section 5.2.1) given by Eq. (5.5) as

$$\begin{bmatrix} \sigma_{li}^0 \\ \sigma_{li}^{m+1} \end{bmatrix} = \mathcal{S}_N \begin{bmatrix} u_i^0(0) \\ u_i^{n+1}(h_m) \end{bmatrix} \quad (6.33)$$

The above equations can be rewritten and solved in terms of the incident, transmitted, reflected amplitudes and the stiffness matrix as shown below

$$\begin{bmatrix} \mathbf{u}^1(0) \\ \mathbf{u}^m(h_m) \end{bmatrix} = \begin{bmatrix} \mathbf{D}^+(\mathbf{0})\mathbf{A}^{incident} + \mathbf{D}^-(\mathbf{0})\mathbf{A}^{reflected} \\ \mathbf{D}^+(\mathbf{n}+1)\mathbf{A}^{transmitted} \end{bmatrix} \quad (6.34)$$

$$\begin{bmatrix} \sigma^l(0) \\ \sigma^m(h_m) \end{bmatrix} = \begin{bmatrix} \mathbf{F}^+(\mathbf{0})\mathbf{A}^{incident} + \mathbf{F}^-(\mathbf{0})\mathbf{A}^{reflected} \\ \mathbf{F}^+(\mathbf{n}+1)\mathbf{A}^{transmitted} \end{bmatrix} \quad (6.35)$$

$$\begin{bmatrix} \mathbf{F}^+(\mathbf{0})\mathbf{A}^{incident} + \mathbf{F}^-(\mathbf{0})\mathbf{A}^{reflected} \\ \mathbf{F}^+(\mathbf{n}+1)\mathbf{A}^{transmitted} \end{bmatrix} = \begin{bmatrix} \mathbf{S}_{11} & \mathbf{S}_{12} \\ \mathbf{S}_{21} & \mathbf{S}_{22} \end{bmatrix} \begin{bmatrix} \mathbf{D}^+(\mathbf{0})\mathbf{A}^{incident} + \mathbf{D}^-(\mathbf{0})\mathbf{A}^{reflected} \\ \mathbf{D}^+(\mathbf{n}+1)\mathbf{A}^{transmitted} \end{bmatrix} \quad (6.36)$$

Carrying out matrix Multiplication an rearranging the matrices in Eq. (6.36) , we formulate Eq. (6.37) to calculate the amplitude of the reflected and transmitted wave in the semi-infinite medium

$$\begin{bmatrix} -\mathbf{S}_{11}\mathbf{D}^-(\mathbf{0}) + \mathbf{F}^-(\mathbf{0}) & -\mathbf{S}_{12}\mathbf{D}^+(\mathbf{n}+1) \\ -\mathbf{S}_{21}\mathbf{D}^-(\mathbf{0}) & -\mathbf{S}_{22}\mathbf{D}^+(\mathbf{n}+1) + \mathbf{F}^+(\mathbf{n}+1) \end{bmatrix} \begin{bmatrix} \mathbf{A}^{reflected} \\ \mathbf{A}^{transmitted} \end{bmatrix} = \begin{bmatrix} \mathbf{S}_{11}\mathbf{D}^+(\mathbf{0}) - \mathbf{F}^+(\mathbf{0}) \\ \mathbf{S}_{21}\mathbf{D}^+(\mathbf{0}) \end{bmatrix} \begin{bmatrix} \mathbf{A}^{incident} \end{bmatrix} \quad (6.37)$$

For simplicity the amplitude of the incident wave can be taken as unity and the above equation can then be solved to calculate the amplitude of the reflected and transmitted wave, which are the reflection and transmission coefficients respectively of the upper and lower bounding layers.

6.3.2 Calculation of the scattering from Side drilled hole embedded in the medium

I use the bounded beam approach to calculate the received signal from an SDH as the its scattering has been calculated in the frequency-space domain and not in the frequency-wavenumber domain. In the bounded beam approach the signal from the transmitting element to the scatterer, the signal received by the receiving element and the scattering response of the Side drilled hole in the frequency space domain are multiplied as shown below [12] in the frequency domain to produce the output signal which is dimensionless as shown in Eq. (6.38).

$$V(x_t, x_r, 0, \omega) = V_t(x_t, 0, \omega) V_r(x_r, 0, \omega) A(x_t, x_r, \omega) \quad (6.38)$$

Where

$$V_t(x_t, 0, \omega) = \int_{-\infty}^{+\infty} v_t(k_{x_t}, 0) \beta(\omega) T(k_{x_t}, 0) e^{-i(k_{x_t} x_t)} dk_{x_t} \quad (6.39)$$

$$V_r(x_r, 0, \omega) = \int_{-\infty}^{+\infty} v_r(k_{x_r}, 0) \beta(\omega) T(k_{x_r}, 0) e^{-i(k_{x_r} x_r)} dk_{x_r} \quad (6.40)$$

T is the transmission coefficient of the plane waves traveling from layered media into homogeneous equivalent anisotropic media, β is the system function as explained in Chapter 5, Section 5.3, v_t is the acoustic wavefield at the face of the transmitting transducer, v_r is the acoustic wavefield at the face of the receiving transducer calculated from the previous chapter. A is the scattering magnitude of the SDH calculated using Eq. (6.23)

The received signal time domain signal from the scatterer is then calculated using the equation

$$V(x_t, x_r, t) = \int_{-\infty}^{+\infty} V(x_t, x_r, \omega) e^{-i(\omega t)} d\omega \quad (6.41)$$

Eq. (6.41) gives the received Full matrix capture signal for scattering from a defect embedded in a medium. Eq. (6.41) is used to generate the Full Matrix Capture data which is used by the imaging algorithm to image the defect and the scattering from the defect

The next section gives an explanation of the Total Focusing Method.

6.3.3 Total Focusing Method Imaging

The total focusing method is considered the gold standard of imaging algorithms [13]. It is a delay and sum algorithm which uses the entire full matrix capture data. The TFM algorithm generates an image by synthetically focusing at every pixel in the image domain as given in the below equation

$$I(x, z) = \left| \sum V_{t,r} \left(\frac{\sqrt{((x_1)_t - x_1)^2 + x_3^2} + \sqrt{((x_1)_r - x_1)^2 + x_3^2}}{c} \right) \right| \quad (6.42)$$

Where I is the intensity of the image at the point x, z , c is the velocity of the wave in the medium, $V_{t,r}$ is the received signal for a transmitter receiver pair.

For anisotropic media the velocity c is calculated using the Christoffel equation as shown in Appendix A and varies as per the angle of propagation. Hence the varying group velocity in an anisotropic material is taken into consideration, which differentiates the model assisted corrected Total Focusing Method from the isotropic Total Focusing Method.

6.3.4 Quantitative comparison of the images

The image formed using experimental data is different from the one formed using the simulated data as the experimental image additionally contains the scattering from the Side drilled hole and interaction of the signals with the

layers below the Side drilled hole and backwall. In defect detection, the signal from the defect is important hence in order to compare the experimental and simulated images and also for comparison between different simulated images, the SNR of the defect should be considered. In this context the SNR is defined as the ratio of the peak amplitude of the scatterer to the noise in the image around the scatterer. The reverberations from the layers, and the signals from the laminated structure are considered as noise as they affect the received signal from the scatterer. In this case the SNR is given by Eq. (6.43)

$$SNR = \sqrt{\frac{\text{Peak Signal (SDH)}}{\sigma_{RMS} (\text{Noise})}} \quad (6.43)$$

The Signal to noise ratio for the simulated image can be calculated in the following steps

1. Simulate the response from the embedded scatterer and calculate the peak amplitude of the scatterer.
2. Simulate the response of the laminate without the scatterer and calculate the root mean square of the amplitudes of the signal in a chosen region around the scatterer which is the “noise” of the image.
3. Use equation 6.43 to calculate the Signal to Noise Ratio of the Side Drilled Hole. The same procedure is carried out for the experimental Total focusing method image wherein the laminate Full matrix capture signals are processed before and after the SDH has been drilled into the laminate.

The next section presents the results for each step and the final image which was simulated using Total Focusing Method.

6.4. Simulation and Results

In this section simulation and experimental results will be presented. The calculations were carried out using two transducer arrays of different center frequencies, array size and number of elements.

The experimental FMC signals were acquired using the FI ToolBox from Diagnostic Sonar. The transducers used were phased array transducers supplied by Olympus . The signals were captured using the Diagnostic Toolbox and were imported into MATLAB® for plotting the data. The simulations were carried out using MATLAB 2017®.

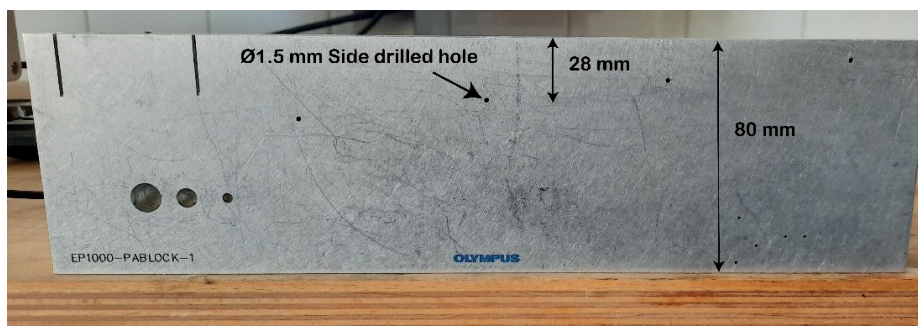
The specifications of the transducers are shown in the Table 6.1.

Table 6.1: Transducer Array specifications

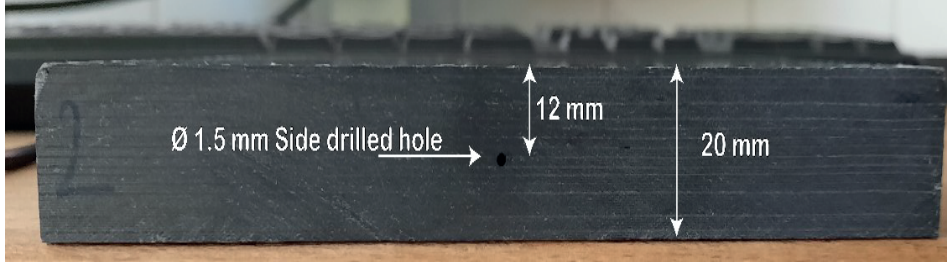
	Centre Frequency (MHz)	Pitch (mm)	Number of Elements
Array 1	2.25	1	64
Array 2	5	0.6	16

For simulation and experimental purposes I consider an aluminum block 80 mm thick (Olympus EP1000-PABLOCK-1) as shown in Figure 6.2 (a). Only 1 SDH of diameter 1.5 mm at a depth of 28 mm for simplicity is considered for simulation and experimental validation purposes. A CFRP laminate which was quasi isotropic and 19 mm thick with (0/45/-45/90) layup is considered for simulation and experimental purposes as shown in Figure 6.2 (b). There are 169 layers of UniDirectional CFRP prepreg of 110 μm thickness in the laminate with layer of epoxy resin of thickness 5 μm between them. The laminate was manufactured from Toray TC380 unidirectional prepreg in an epoxy resin system. Manufacturing was carried out using autoclave curing. The hole in the CFRP laminate is at a depth of 12 mm from the surface of the laminate as shown in the Figure 6.2 (b) which was manufactured by drilling. As the size of the side drilled hole is relatively small and the side drilled hole has a length of 20 mm it was assumed that delamination caused due to drilling was minimal. For the purpose of the simulation, the layers containing the SDH and below it have been homogenized.

The aluminium and CFRP lamina properties are the same as shown in Chapter 5 Table 2.



(a) Aluminium block with SDH of different diameters



(b) CFRP laminate with one SDH

Figure 6.2. (a) Picture of the aluminium block with SDH used to verify the simulation results (b) CFRP laminate with one side drilled hole use to verify the simulation results

6.4.1 Calculation of equivalent homogeneous properties

By substituting the lamina properties into Eq. (6.8) - Eq. (6.22) I get the equivalent homogeneous anisotropic properties as shown below

Table 6.2: Equivalent Homogeneous Anisotropic Properties

Properties	Values in GPa
\overline{C}_{11}	54.76(1+0.002i)
\overline{C}_{22}	54.76(1+0.002i)
\overline{C}_{33}	13.89(1+0.02i)
\overline{C}_{12}	18.53(1+0.01i)
\overline{C}_{13}	5.96(1+0.004i)
\overline{C}_{23}	5.96(1+0.005i)
\overline{C}_{44}	4.3(1+0.06i)
\overline{C}_{55}	4.3(1+0.06i)
\overline{C}_{66}	18.12(1+0.03i)

These properties in Table 6.2 were then used to calculate the transmission coefficient of the plane waves into the semi-infinite anisotropic medium and were also used to calculate the group velocity in the medium.

In the next section the simulation and experimental results for a SDH embedded in an isotropic medium are presented.

6.4.2 SDH embedded in Aluminium inspected by a 2.25 and 5 MHz array

In this section I present the simulation and experimental results of the scattering from an side drilled hole embedded in an isotropic medium. Simulation and experimental full matrix capture signals are generated for an isotropic material so as to prove the validity of the developed model for both isotropic and anisotropic materials. The images of a side drilled hole embedded in an isotropic material are also generated so as to compare the differences between scattering in isotropic and anisotropic embedding mediums.

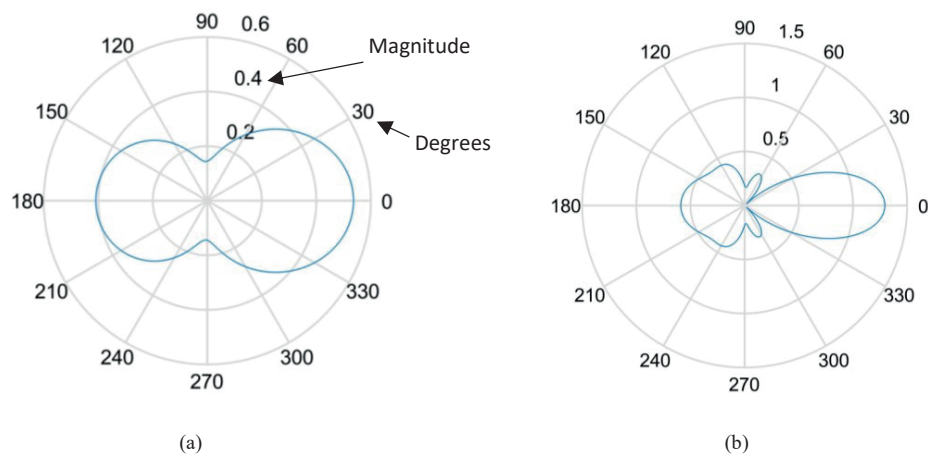


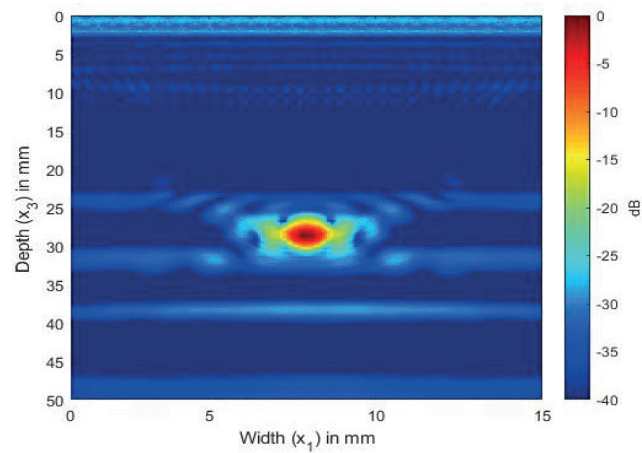
Figure 6.3 (a) Non-dimensional scattering magnitude of 1.5 mm diameter hole in aluminium at 2.25 MHz frequency (b) Non-dimensional scattering magnitude of 1.5 mm diameter hole in aluminium at 5 MHz frequency.

Figure 6.3 (a) and (b) shows the nondimensional scattering magnitude of 1.5 mm diameter side drilled hole embedded in aluminium when inspected by a waves of centre frequency 2.25 and 5 MHz respectively. It is observed that as the frequency increases the magnitude of the scattering amplitude also increases. It is also observed that as the wavelength of the inspecting wave increases as compared to the size of the SDH, the scattering becomes less directional.

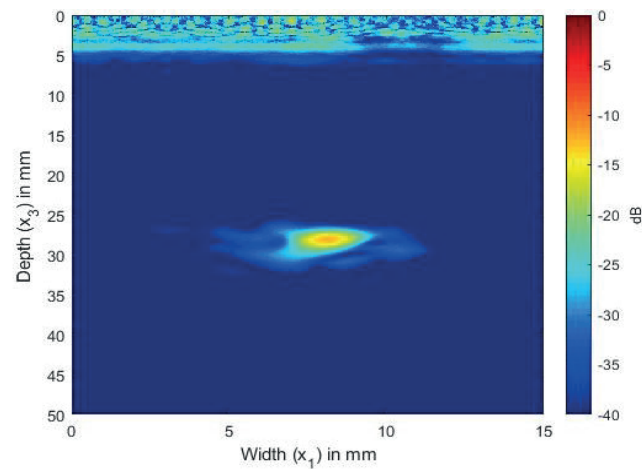
In Figure 6.4 (a) and (b) I present the simulated and experimentally obtained TFM image of SDH embedded in aluminium. The aluminium block shown in Figure 6.2 (a) was used to obtain the FMC signals experimentally.

Figures 6.4 (a) and (b) shows the scattering of a hole of diameter 1.5 mm embedded in aluminium at a depth of 28 mm and inspected by a ultrasonic arrays of frequency 2.25 MHz. Figure 6.4 (a) shows the TFM image generated from the

FMC signals obtained from the simulation whereas Figure 6.4 (b) shows the TFM image generated for the FMC signals obtained experimentally



(a)

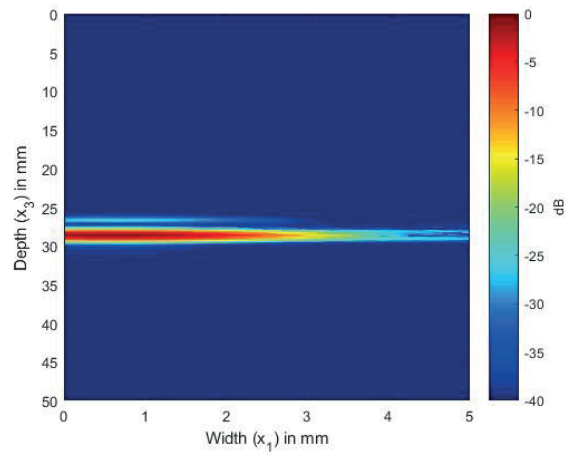


(b)

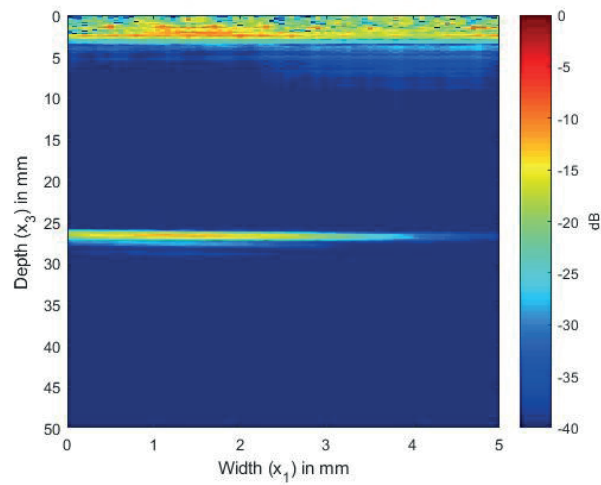
Figure 6.4. (a) TFM image of simulated SDH FMC signals in aluminium using the 2.25 MHz array (b) TFM image of experimental SDH FMC signals in aluminium using the 2.25 MHz array

Figure 6.5 (a) and (b) shows the scattering of a hole of diameter 1.5 mm embedded in aluminium at a depth of 28 mm inspected by a ultrasonic arrays of frequency 5 MHz. Figures 6.5 (a) shows the TFM image generated from the FMC

signals obtained from the simulation whereas Figure 6.5 (b) shows the TFM image generated for the FMC signals obtained experimentally



(a)



(b)

Figure 6.5. (a) TFM image of simulated SDH FMC signals in aluminium using the 5 MHz array (b) TFM image of experimental SDH FMC signals in aluminium using the 5 MHz array

It can be seen from Figure 6.4 (a) that the location and size of the SDH are accurate when the frequency 2.25 MHz is used. The simulation results agree

qualitatively with the experimental results. When the SDH is inspected by the 5 MHz array as shown in Figure 6.5, the SDH seems to be spread over a large area. In the case of the 5 MHz array the simulated and the experimental image are in good agreement. Table 6.3 shows a comparison of the lengths of the side drilled hole along the x and y axis for the simulated and experimental results. The lengths show that the side drilled hole is almost circular when inspected by 2.25 MHz array whereas it is elliptical when inspected by the 5 MHz array.

Table 6.3: Comparison of SDH dimensions in Aluminium

	Simulated		Experimental	
	Length in x	Length in y	Length in x	Length in y
2.25 MHz	1.6 mm	2.3 mm	1.65 mm	2.05 mm
5 MHz	3.41 mm	2.1 mm	3.1mm	1.8 mm

To have a quantitative analysis between the simulation and experimental results, the signal to noise ratio values of the SDH are provided in Table 6.3. The SNR values are calculated using the described equation and procedure in Section 6.3.4. It can be observed the error between the signal to noise ratio values is within the range of +/- 8 dB between the simulated and experimental values.

Table 6.4: SNR of SDH in Aluminium

Central Frequency of Array	SNR of SDH in simulated image	SNR of SDH in experimental image
2.25 MHz	-42.9 dB	-39.5 dB
5 MHz	-26.1 dB	-33.4 dB

For ease of the understandability of the reader Figure 6.6 shows a scaled comparison of the simulated SDH

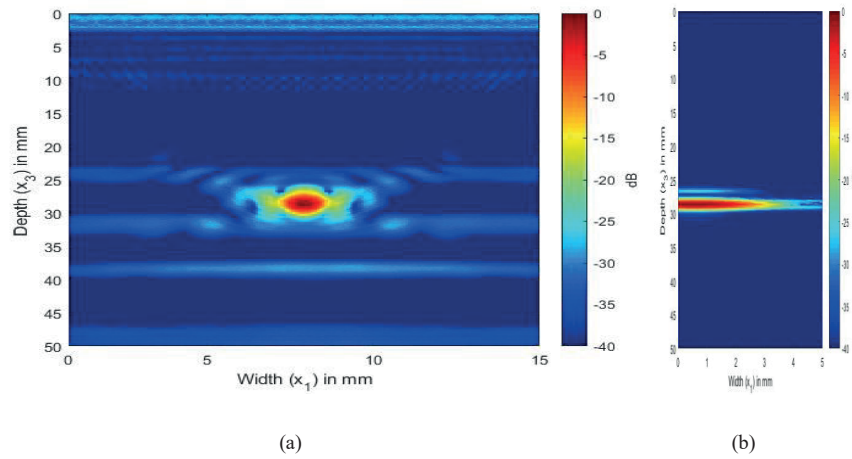


Fig 6.6 A scaled comparison showing the simulated defect when inspected by (a) 2.25 MHz array (b) 5 MHz array

In the next section the simulation and experimental results for a side drilled hole embedded in an equivalent anisotropic medium are presented

6.4.3 SDH embedded in CFRP inspected by arrays of centre frequencies 2.25 and 5 MHz

Figure 6.7 (a) and (b) gives the nondimensional scattering magnitude of a SDH embedded in the homogenized CFRP laminate with equivalent homogeneous properties at center frequencies of 2.25 and 5 MHz respectively. The scattering is given as a function of scattering angle for angles of incidence of 0, 30 and 60 degrees.

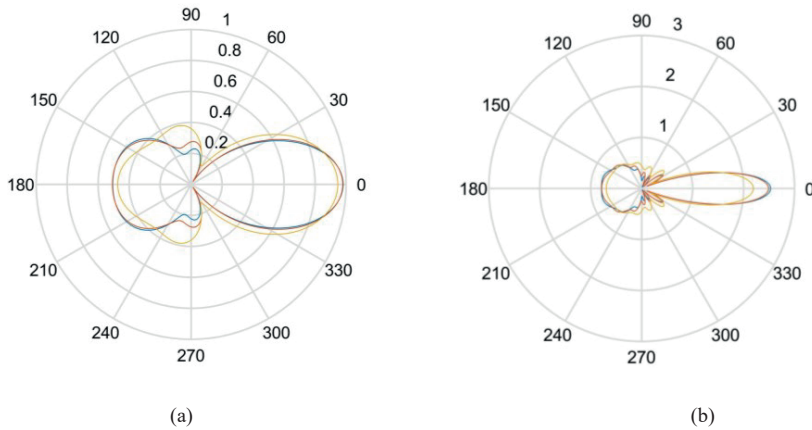


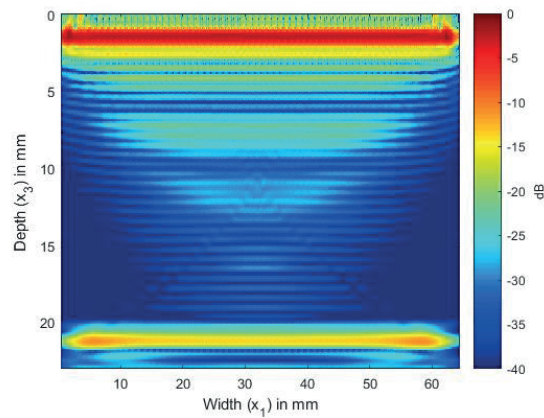
Figure 6.7. (a) Scattering amplitude as a function of angle of incidence for 0° (blue), 30° (orange) and 60° (yellow) for 1.5 mm diameter SDH embedded in homogenized CFRP at 2.25 MHz, (b) Scattering amplitude as a function of angle of incidence for 0° (blue), 30° (orange) and 60° (yellow) for 1.5 mm diameter embedded in homogenized CFRP at 5 MHz

In Figure 6.7 it can be observed that as the angle of incidence increases the scattering amplitude decreases and the directionality of the scattering reduces. As observed in the case of isotropic medium as the frequency increases the scattering magnitude increases.

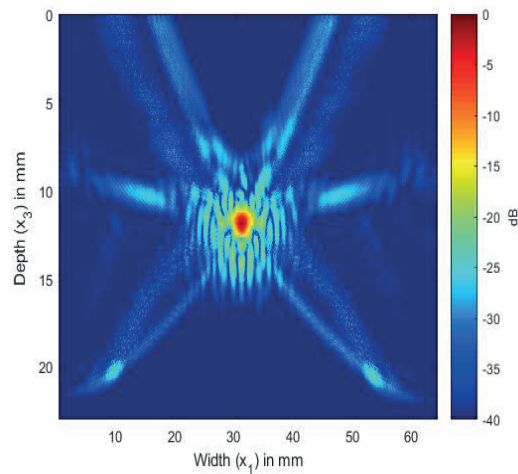
Figure 6.8 shows the total focusing method image generated from simulated full matrix capture signals for the laminate without a side drilled hole and from the hole embedded in an equivalent homogeneous anisotropic medium. Figure 6.8 (a) shows the TFM image of CFRP laminate without the defect. The full matrix capture signals have been simulated using the model developed in Chapter 5. This image is the noise image as it shows the structural reverberations and internal reflections from the layers in the laminate which contributes to the noise generated in the FMC signals. Figure 6.8 (b) shows the total focusing method image of the scattering from side drilled holed generated from FMC signals which have been simulated using Eq. (44).

In Figure 6.8 (a) the image of the CFRP laminate without the defect we observe the internal reflections and reverberations from the layer interfaces. Figure 6.8 (b) shows the scattering from the SDH embedded in a CFRP laminate. We see that the SDH is not exactly circular, is spread over with a diameter of 3 mm and there is also lower magnitude scattering around it. To compare the images generated with the simulated full matrix capture signals to the image generated using the experimentally obtained signals, I added the signals obtained for Figure 6.8 (a) and (b) to create Figure 6.9 (a). Figure 6.9 (a) shows the image generated from simulated FMC signals from the SDH and laminate and Figure 6.9 (b) shows

the image generated from experimentally obtained full matrix capture signals. It is observed that Figure 6.9 (a) is in good agreement with Figure 6.9 (b), with the noise seen in Figure 6.8 (b) contributing to the noise in the composite image. Figure 6.9 (b) shows more noise than Figure 6.9 (a) as the source of the noise could be from the manufacturing process, varying thickness of plies and epoxy after manufacture which is difficult to account for in a simulation.



(a)



(b)

Figure 6.8. (a) TFM image of simulated FMC signals in CFRP laminate without SDH using 2.25 MHz array (b) TFM image of simulated SDH FMC signals in equivalent homogeneous anisotropic laminate using 2.25 MHz array

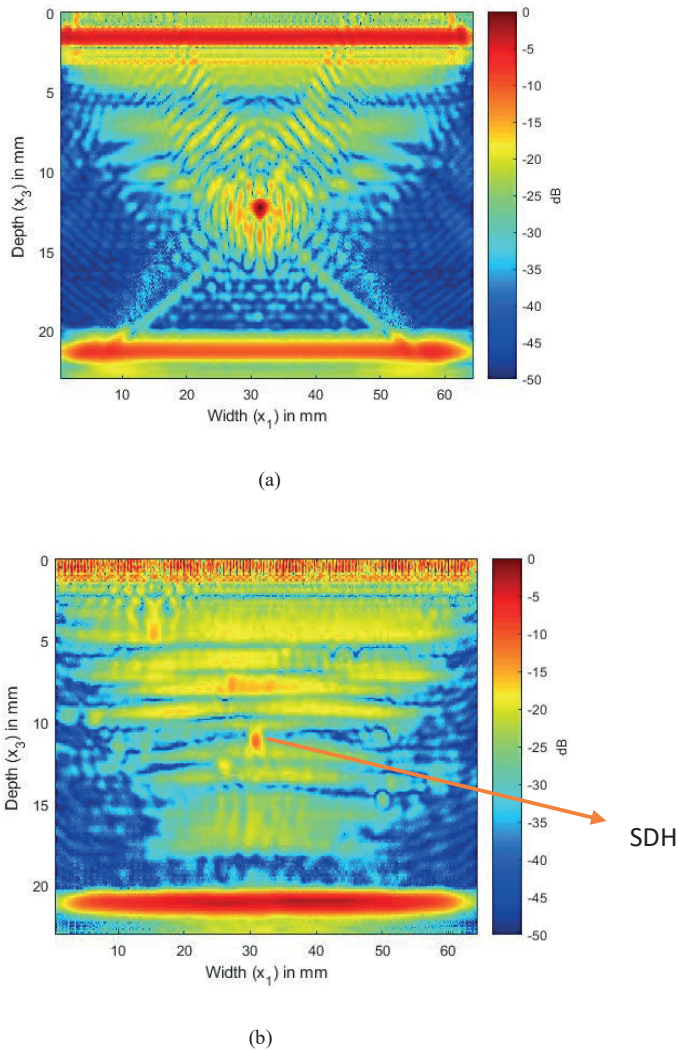
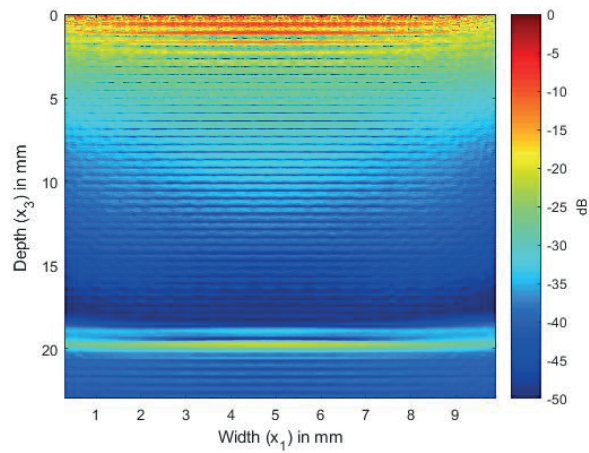


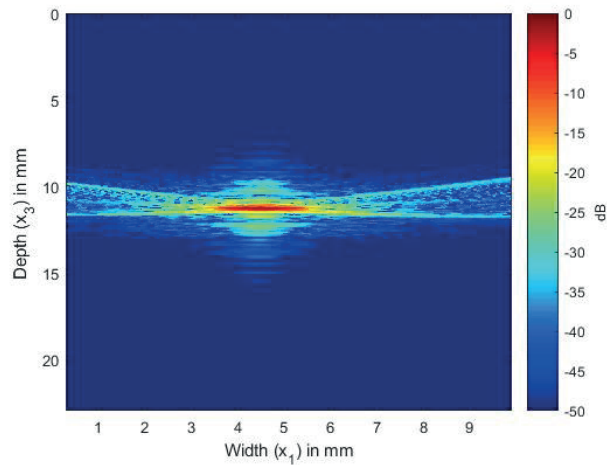
Figure 6.9. (a) Overlay image of simulated SDH signals with simulated composite laminate without SDH inspected by 2.25 MHz array (b) TFM image of experimentally obtained FMC signals from CFRP laminate inspected by 2.25 MHz array

In Figures 6.10 and 6.11, the simulation is carried out using Array 2 with a central frequency of 5 MHz. In figure 6.10 (a) we can see the internal reflections and reverberations of plies, which are more pronounced than those in Figure 6.8 (a). Figure 6.10 (b) shows the side drilled hole at a depth of 12 mm. As in the isotropic case the side drilled hole appears to be spread over a large area with noise at the edges of the side drilled hole. Figure 6.11 (a) shows the image generated

from simulated full matrix capture signals from the side drilled hole and laminate and Figure 6.11 (b) shows the image generated from experimentally obtained FMC signals. It is observed that Figure 6.11 (a) is in good agreement with Figure 6.11 (b), with the noise seen in Figure 6.11 (b) contributing to the noise in the composite image. I observe more noise and artifacts in Figure 6.11 (b) which could be due to manufacturing inconsistencies.

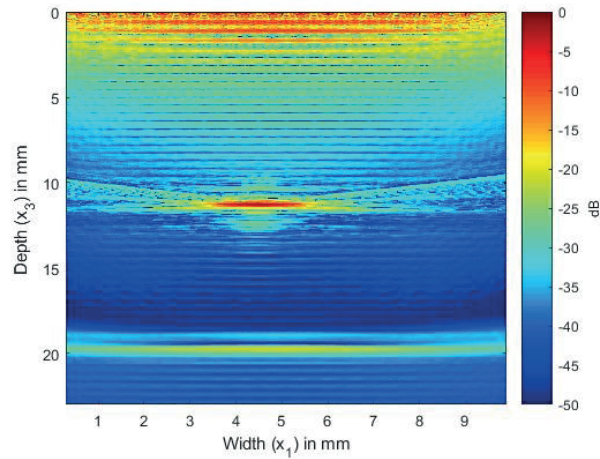


(a)

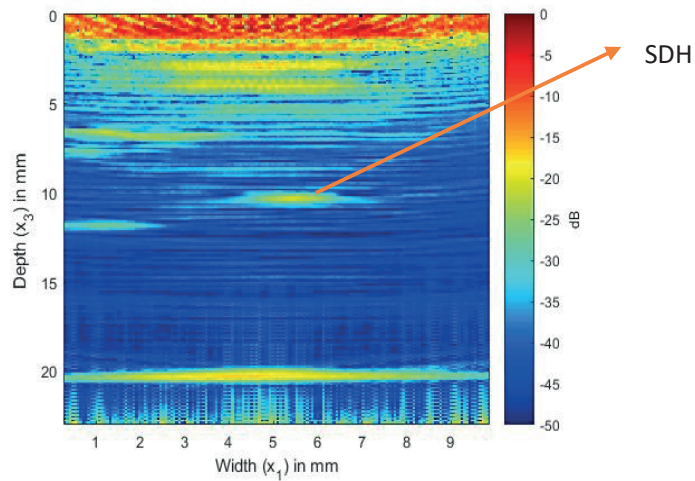


(b)

Figure 6.10. (a) TFM image of simulated FMC signals in CFRP laminate without SDH using 5 MHz array (b) TFM image of simulated SDH FMC signals in equivalent homogeneous anisotropic laminate using 5 MHz array



(a)



(b)

Figure 6.11. (a) Overlay image of simulated SDH signals with simulated composite laminate without SDH inspected by 5 MHz array (b) TFM image of experimentally obtained FMC signals from CFRP laminate inspected by 5 MHz array

Table 6.5 shows a comparison of the lengths of the side drilled hole along the x and y axis for the simulated and experimental results. The lengths show that the side drilled hole is almost circular when inspected by 2.25 MHz array whereas it is elliptical when inspected by the 5 MHz array.

Table 6.5 Comparison of SDH dimensions in CFRP

	Simulated		Experimental	
	Length in x	Length y	Length in x	Length in y
2.25 Mhz	1.3 mm	1.11 mm	1.4 mm	1.7 mm
5 MHz	1.9 mm	1 mm	2.2 mm	0.9 mm

To carry out a quantitative comparison between the experimental and the simulation results the table below shows the SNR of the simulation and experiment.

Table 6.6 SNR of SDH in CFRP

Central Frequency of Array	SNR of SDH in simulated image	SNR of SDH in experimental image
2.25 MHz	-42.9 dB	-25.6 dB
5 MHz	-35.48 dB	-21 dB

An error in the range of 14 dB to 18 dB is observed. The error is higher in the case of the CFRP due to various reasons such as the absence of the effect of layering below the hole and the backwall reflections on the amplitude of the SDH signal. As the hole is of a small diameter, the effects of the layers just below the side drilled hole and the layers in which the SDH is embedded on the received amplitude is higher than simulations. It is also seen that defects during manufacture also influence the signal from the SDH which cannot be included beforehand in the simulation.

6.5. Discussion

Figures 6.4 and 6.5 show the comparison between the simulated and the experimental TFM images of side drilled hole embedded in an aluminium block. It was observed that when the size of the side drilled hole is larger than the wavelength of the inspecting wave, the SDH appears to spread over a larger area

as is in the case of 5MHz array. This is due to the fact that the scattering at these higher frequencies is of higher magnitude and the decrease in scattering magnitude with the scattered angle is less as observed in Figure 6.3. A quantitative comparison of the SNR also leads to the conclusion that the simulation images for defects in isotropic media agree well with the experimental images.

Next Figures 6.9 and 6.11 present a comparison between the simulated and experimental images of SDH embedded in a laminate. Here the medium in which the SDH is embedded and the layers below it have been modelled as a semi-infinite anisotropic region using the equivalent homogeneous anisotropic properties given in Table 6.2. As in the case of an isotropic embedding medium, the SDH at 2.25 MHz shows good agreement between the simulated and experimental image. More noise is visible around the SDH. This noise is due to the anisotropic velocity in different directions and also due to the creeping wave [14]. As the pitch between the elements is 1mm and the array is a 64 element array, the angle of incidences are large, and the theoretical group velocities, as shown in Figure 6.12 along these angles are large leading to the noise accompanying the scattering signal. The group velocity is calculated using the expression given in Eq. 6.44 where u_p is the group velocity, c_p is the phase velocity, c_{ijkl} is the elastic constant, p is the polarization direction, n is the unit vector in the direction of propagation of the wave

$$u_{pi} = \frac{c_{ijkl} n_k p_l p_k}{\rho c_p} \quad (6.44)$$

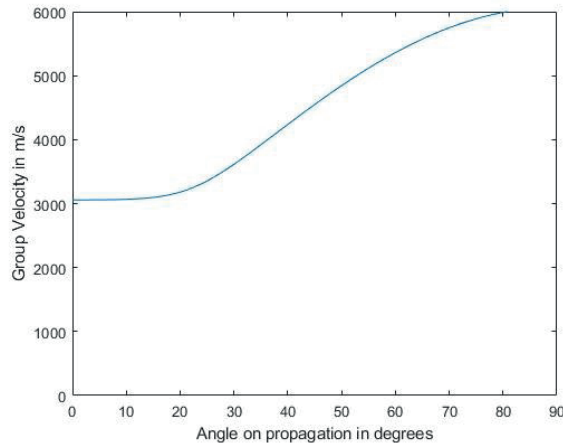


Figure 6.12. Group velocity of the longitudinal wave for different angles of propagation.

Figure 6.10 shows the scattering from the hole when inspected with Array 2 which has a central frequency of 5 MHz. Less noise is observed around the edges as compared to the TFM image using a 2.25 MHz array. This is due to the fact that, because of a smaller pitch and less number of elements in the array, the maximum angle of propagation is confined to be less than 40° and hence the variation of the group velocity is not very large.

In CFRP laminate the image of the hole is elliptical due to the various effects of the diffraction of the layers from above, the inspecting wavelength as compared to the size of the side drilled hole and the anisotropic velocity. The simulation provides a good tool to determine which frequencies need to be used to inspect a certain material, defect size, location, etc. I observed that the difference in the SNR values between the simulation and experimental images is larger for CFRP as compared to aluminium. One of the reasons for this is that the defect is assumed to be embedded in a homogeneous medium and the layers beneath it are not taken into account in the simulation. The layers below the defect will also contribute to the noise in the image reducing the SNR in the experimental TFM image.

6.6. Conclusions

This Chapter proposes a modelling technique based on the Gaussian beam and recursive stiffness matrix method to simulate the scattering from a SDH embedded in a CFRP laminate. The simulation requires the integration of different modules to simulate the scattering of an SDH. A novel method is implemented to calculate the transmission and reflection coefficients from layered media into a semi-infinite anisotropic medium by combining the transfer matrix and recursive stiffness matrix approaches.

The modelling technique takes into consideration the diffraction, anisotropic velocity, and inspection frequency effects into account while simulating the scattering from the SDH embedded in a layered medium. The simulation and the experimental results are in good agreement which is observed qualitatively using total focusing method to image the full matrix capture signals and also quantitatively by comparing the SNR values for both isotropic and anisotropic samples. To the knowledge of the author there are no analytical models which can be used both in immersion and contact setups based on Multi Gaussian beams and stiffness matrix method to simulate the scattering from side drilled holes. Hence this chapter provides a model which can be used both in immersion and contact setups, which is both computationally inexpensive and accurate.

6.7 References

- [1] S. I. Rokhlin, D. E. Chimenti, and P. B. Nagy, *Physical ultrasonics of composites*. Oxford University Press, 2011.
- [2] C. T. Sun and S. Li, “Three-Dimensional Effective Elastic Constants for Thick Laminates,” *J. Compos. Mater.*, 1988, doi: 10.1177/002199838802200703.
- [3] L. W. Schmerr, *Fundamentals of Ultrasonic Phased Arrays*, vol. 215, no. May 2003. Cham: Springer International Publishing, 2015.
- [4] G. W. Postma, “Wave Propagation in a Stratified medium,” *Geophysics*, 1955, doi: 10.1190/1.1438187.
- [5] O. Ishai, I. M. Daniel, “Engineering mechanics of composite materials,” *Materials & Design*. 2006.
- [6] D. Liu and X. Li, “An overall view of laminate theories based on displacement hypothesis,” *J. Compos. Mater.*, 1996, doi: 10.1177/002199839603001402.
- [7] G. E. Backus, “Long-wave elastic anisotropy produced by horizontal layering,” *J. Geophys. Res.*, 1962, doi: 10.1029/jz067i011p04427.
- [8] C. T. Sun and S. Li, “Three-Dimensional Effective Elastic Constants for Thick Laminates,” *J. Compos. Mater.*, vol. 22, no. 7, pp. 629–639, 1988, doi: 10.1177/002199838802200703.
- [9] L. W. Schmerr, “Modeling Ultrasonic Problems for the 2002 Benchmark Session,” *AIP Conf. Proc.*, vol. 657, no. April, pp. 1776–1783, 2003, doi: 10.1063/1.1570344.
- [10] A. L. Lopez-Sanchez, H. J. Kim, L. W. Schmerr, and A. Sedov, “Measurement models and scattering models for predicting the ultrasonic pulse-echo response from side-drilled holes,” *J. Nondestruct. Eval.*, vol. 24, no. 3, pp. 83–96, 2005, doi: 10.1007/s10921-005-7658-4.
- [11] R. Huang, “Ultrasonic modeling for complex geometries and materials,” *Iowa State Univ.*, 2006, [Online]. Available: <http://adsabs.harvard.edu/abs/2006PhDT.....54H>.
- [12] B. A. Auld, “General electromechanical reciprocity relations applied to the calculation of elastic wave scattering coefficients,” *Wave Motion*, vol. 1, no. 1, pp. 3–10, Jan. 1979, doi: 10.1016/0165-2125(79)90020-9.
- [13] C. Holmes, B. W. Drinkwater, and P. D. Wilcox, “Post-processing of the full matrix of ultrasonic transmit–receive array data for non-destructive evaluation,” *NDT E Int.*, vol. 38, no. 8, pp. 701–711, 2005, doi: 10.1016/j.ndteint.2005.04.002.
- [14] A. L. Lopez-Sanchez, H. J. Kim, L. W. Schmerr, and T. A. Gray, “Modeling the response of ultrasonic reference reflectors,” *Res. Nondestruct. Eval.*, vol. 17, no. 2, pp. 49–69, 2006, doi: 10.1080/09349840600689459.

7

Conclusions and future work

The use of anisotropic homogeneous and layered materials in aircraft structures has substantially increased over the past decade. With their high strength to weight ratio, these materials find usage in more complex aircrafts structures with complex geometries and configurations and the non-destructive testing of such structures becomes more important. The usage of phased arrays in different configurations is being increasingly used to test such structures. NDT has remained the bottleneck of such composite structure inspections due to the complexity of the their mechanical behaviour and failure mechanisms.

It is imperative that a thorough understanding of such structures with their effects on the received NDT signals is undertaken so as to be able to guide decisions regarding repair and replacement.

The main objective of this thesis was to develop models for ultrasonic phased array inspection in homogeneous or layered anisotropic composite materials which are computationally inexpensive and accurate.

To achieve this goal three research questions were formulated and each chapter deals with answering these questions The following sub sections give the conclusions of each chapter.

7.1 Linearly phased Multi Gaussian beam model for beam propagation for phased array into an anisotropic media.

In Chapter 4 a corrected paraxial beam model based on the superposition of Gaussian beams was developed . Chapter 4 showed the computational efficiency and the accuracy of the developed model. It was validated by a numerically developed beam model. The model developed enabled steering above the paraxial limit in anisotropic media while remaining accurate and computationally efficient. The developed model also showed the effects of anisotropy on the phased array beam propagating through the material, leading to a change in focal distance and the angle of beam steering. The developed model was able to predict the beam skew, divergence and beam compression /expansion when propagating through an anisotropic medium. The anisotropic medium chosen was austentic steel, due to its usage is aircraft structures. The results from the developed model can then be used for correcting/compensating beam steering in anisotropic media and compensating for the change in focus of the beam in such a medium.

7.2 A Gaussian beam based recursive stiffness matrix model to simulate the ultrasonic array signals from composite laminate

The beam model developed in Chapter 4 works well when dealing with homogeneous anisotropic media, but when encountering layered anisotropic media, the model becomes cumbersome and computationally expensive due to the numerous beams which need to be traced, which are a result of layer reverberations, reflection at layer interfaces, etc. Full matrix capture was considered for testing of layered composites materials. As interest lies with the received output signal at the transducers and not in each beam path taken in the layered material, a model was developed by combining the multi Gaussian beam approach to model the radiation from the phased array transducers and the stiffness matrix approach to model the plane wave response of the multi-layered composite material. Both the transducer model and the response of the matrix are combined using an angular spectrum approach.

The developed model was validated against observed experimental signals and was used to simulate the FMC signals generated when isotropic homogeneous and anisotropic layered CFRP are tested using different arrays with different number of elements, centre frequency, etc. The model is able to predict accurately the response of the layered media and how it affects the output signal. The developed model also takes into consideration the various transducer parameters such as the finite element size, pitch of the array and its effects on the received signal. An error of ± 2 dB was observed between experimental and simulated signals showing good agreement between the simulated and experimental results.

7.3 Modelling the scattering from a side drilled hole embedded in a layered anisotropic medium

After developing the model for multi layered media, the next step was to integrate the model with a scattering of an embedded defect in a media, to simulate the scattered FMC signals and to image the defect and its scattering response. An expression was derived to calculate the reflection and transmission coefficients to/from a laminate into an anisotropic media. This was done so as to facilitate the assumption that the defect is embedded in a homogeneous anisotropic medium. Equivalent homogeneous anisotropic properties for the embedding medium were calculated and the scattering of a SDH was calculated using the method of separation of variables. The scattering from SDH was then simulated and imaged using the total focusing method with the corrected anisotropic velocity.

Experimental and simulation results agreed with each other and it was observed that the scattering from a SDH was highly dependent on the frequency of the inspecting wave, the size of the SDH relative to the inspecting wavelength and the parameters of the transducer array. The SDH which was imaged was of a different size and shape than the real embedded defect due to the anisotropy of the material and both the simulated and experimental images agreed in this regard.

SNR analysis was carried out for the scattering from the SDH. In composite laminates the structural reflections and reverberations were considered as noise and the scattering from the SDH as the signal. The SNR comparison for SDH embedded in isotropic medium showed a small error owing mainly to the effects of the backwall reflection on the magnitude of the scattering amplitude not being taken into consideration. The SNR comparison for an embedded SDH in a CFRP laminate between the simulation and experimental showed a higher error value. This was mainly due to manufacturing deviations of the laminate which induced some defects that were visible in the TFM image, the layers in which the SDH is embedded, the layers below the SDH and the backwall reflection also influence the scattering magnitude. Keeping these sources of error in mind, the model was still able to provide good results on the shape, size, location of the scatterer.

Hence in this thesis I developed two multi Gaussian beam based models to simulate the beam steering in anisotropic media and to simulate the FMC signals when inspecting a multi-layered anisotropic media such as CFRP, with or without defects in it. The linearly phased multi Gaussian beam model can be used for different array, centre frequencies, homogeneous anisotropic materials to investigate and study the changes the ultrasonic beam undergoes when it propagates or is steered in such materials leading to corrections or compensations which can then be applied to the time delays or focusing in the real world testing scenario.

The Gaussian beam based recursive stiffness matrix model and its application to simulate the scattering from defects can be used to simulate the response of laminates of different materials, layer thicknesses, sizes, different array parameters, different inspection scenarios (immersion/contact) and different defects. This developed model provides an understanding of the scattering in different scenarios, the structural noise generated during inspection and can be used for better interpretation and understanding of real inspection TFM images.

7.4 Recommendations for Future Work

The models developed in this thesis are the first stepping stone in developing a completely versatile model. Some of the work which can be carried out in the future are:

1. With the use of sandwich materials in aircraft structures, modelling beam propagation in such a structure becomes complicated due to the thick core as compared to the thin skin laminate. To see the effect on the ultrasonic beam propagation through the structure and the output signals the Linearly phased multi Gaussian beam method can be used. This would require the propagation of the beam through CFRP laminates and the sandwich core. Combinatorics [1] can be used to calculate the beams in the CFRP skins and these beams can then be traced with ease through the thicker core. As compared to the ray method, the multi Gaussian beam method is suited for this as there is a need to track only one beam formed by the superimposition of a small number of beams.

2. The defect is assumed to be bounded by an upper layered medium and a lower semi-infinite anisotropic medium. A further step would be to replace the lower semi-infinite anisotropic medium with a layered medium, hence including the effects of the layers below the SDH, and the backwall on the magnitude of the scattering amplitude. The chosen defect for this thesis was a SDH as its scattering magnitude could be calculated analytically. The scattering from more complex defects such as delamination, etc can be carried out using numerical methods [2] and then integrated with the model as shown in this thesis. This would enable the modelling technique to be used to simulate the response from complex and different defects.

3. In this thesis the corrected total focusing method was used to post process the FMC signals and image the structure. This required the homogenization of the layered structure to calculate the group velocity of the wave propagating through the structure. Dijkstra's algorithm [3] has shown promise in applying the group velocity on a layer to layer basis but has been carried out for a small number of layers. Dijkstra's algorithm combined with TFM should be evaluated for a larger number of layers, which could lead to more accurate images being formed.

Another way forward is the application of frequency domain algorithms to post process the FMC data. These frequency domain algorithms such as the Wavenumber algorithm and Stolt's f-k [4], [5] migration algorithm have been shown to be computationally efficient and accurate while imaging isotropic single layer structures. These algorithms can further be modified to be used for

anisotropic layered structures by modifying the Green's function which forms the basis of the wavenumber algorithm.

7.5 References

- [1] P. F. Daley and F. Hron, "Ray-reflectivity method for SH-waves in stacks of thin and thick layers," *Geophys. J. R. Astron. Soc.*, vol. 69, no. 2, pp. 527–535, 1982, doi: 10.1111/j.1365-246X.1982.tb04963.x.
- [2] W. Ostachowicz and M. Krawczuk, "Modeling for Detection of Degraded Zones in Metallic and Composite Structures," in *Encyclopedia of Structural Health Monitoring*, Chichester, UK: John Wiley & Sons, Ltd, 2008.
- [3] C. Lanherne and P. Wilcox, "Ray tracing and FMC simulation in curved composite structures," *AIP Conf. Proc.*, vol. 2102, no. May, pp. 1–8, 2019, doi: 10.1063/1.5099853.
- [4] A. J. Hunter, B. W. Drinkwater, and P. D. Wilcox, "The wavenumber algorithm for full-matrix imaging using an ultrasonic array," *IEEE Trans. Ultrason. Ferroelectr. Freq. Control*, vol. 55, no. 11, pp. 2450–2462, 2008, doi: 10.1109/TUFFC.952.
- [5] L. Merabet, S. Robert, and C. Prada, "2-D and 3-D Reconstruction Algorithms in the Fourier Domain for Plane-Wave Imaging in Nondestructive Testing," *IEEE Trans. Ultrason. Ferroelectr. Freq. Control*, vol. 66, no. 4, pp. 772–788, 2019, doi: 10.1109/TUFFC.2019.2895995.

Appendix A

Calculation of phase velocity, polarization vectors and group velocity

For calculating the phase velocity we begin with the Christoffel equation as shown below

$$\left(c_{ijkl}n_jn_k - \rho c_p^2 \delta_{il}\right)d_l = 0 \quad (\text{A.1})$$

Trivial solution of the above equation would be when polarization is zero, which is not possible. Non trivial solution would be as shown below

$$\left|c_{ijkl}n_jn_k - \rho c_p^2 \delta_{il}\right| = 0 \quad (\text{A.2})$$

Where the magnitude of the terms in the braces is zero

The above equation is an eigenvalue equation whose solution gives the phase velocity of the wave in the material.

Terms are grouped as shown in Eq. (A.3)

$$G_{il} = c_{ijkl}n_jn_k \quad (\text{A.3})$$

Hence substituting Eq. (A.3) into Eq. (A.2)

$$\left|G_{il} - \rho c_p^2 \delta_{il}\right| = 0 \quad (\text{A.4})$$

Eq. (A.4) in matrix form is given below

$$\begin{vmatrix} G_{11} - \rho c_p^2 & G_{12} & G_{13} \\ G_{21} & G_{22} - \rho c_p^2 & G_{23} \\ G_{31} & G_{32} & G_{33} - \rho c_p^2 \end{vmatrix} = 0 \quad (\text{A.5})$$

Solving the above determinant gives three different phase velocities for three different waves. The three velocities provide the velocities for the quasi-longitudinal, quasi-shear horizontal and quasi shear vertical waves.

Finding the polarization of the waves.

The polarizations of the waves can be found out by considering Eq. (A.1)

$$(G_{11} - \rho c_p^2)d_1 + G_{12}d_2 + G_{13}d_3 = 0$$

$$G_{21}d_1 + (G_{22} - \rho c_p^2)d_2 + G_{23}d_3 = 0$$

$$G_{31}d_1 + G_{32}d_2 + (G_{33} - \rho c_p^2)d_3 = 0$$

Solve the above system of equations to find the polarization directions with the given constraint

$$d_1^2 + d_2^2 + d_3^2 = 1$$

Acknowledgments

A PhD is a journey and not a destination. It comes with its own ups and downs as well as important life lessons. People are an important part of this journey without who this journey can never be complete. They infuse the help, support, love and encouragement making this journey a very exciting and eventful one.

First and foremost I would like to thank Roger for believing in me and helping me through this PhD. You provided me with valuable advice and help whenever I required it. You provided me the tools and freedom to grow in this PhD and become an independent researcher. I could always count on your guidance and thank you for helping me get out of sticky situations.

I would like to thank Rinze for providing the opportunity to pursue a PhD in the group and for the valuable discussions during our meetings. I really appreciate the support provided by you through this process.

Next I would like to thank the one and only Gemma! I would not be exaggerating when I say that the PhD could not have been completed without your help. You made life so much easier and you were always ready to help and sort out things for me. I could always count on your support whenever needed.

I would also like to thank Dr. Damien Pain, Dr. Robert Grandin, Prof. P.B Nagy, Prof. Pat Daley, Prof. Ludek Klimes and Dr. Steven Delrue for replying to my countless emails regarding their expertise and patiently answering my questions. I would also like to thank Prof. Hyunjo Jeong for his help in understanding multi Gaussian beams.

I would also like to thank my committee members Prof. M. Snellen, Prof. W. Oscatchowicz, Prof. Lhémy, Prof. U. Staufer, Prof. C. Dransfeld and Dr. S. Shroff for taking out time to go through my thesis and provide valuable feedback.

Thank you to all the technicians in the lab Berthil, Fred, Kees, Misja, Victor and Gertjan for their help in the lab.

The first year of the PhD can be tough when you are new and far away from family. I was lucky to have Mayank when I first came here. Thank you for your advice, coffee chats, lunch chats, barging into my office and all the discussions ranging from politics to sports to cryptocurrency and philosophy.

I would also like to thank Andrei, Pedro, Fabricio, Lucas, Nikos, John Wayne, Ilias, Neils, Freek, John-Alan, Cornelis, Leila, Nakash, Agnes, Chantal, Tian, Papa Wang, Romina, Julian, Nick, Xi Li, Ozan, Zahid, Vincentus, Nan Tao, Nitesh, Nakash, Irene and Dimitris. Thank you for making my Phd journey fun and enriching it with your experiences and making it overall a very fun one (being part of an office even if it was not my office, spinning classes, lunch discussions etc)!

Special thanks to Bram for helping me with the translations and also helping me to pass my Dutch speaking exam!

When I started my PhD I would never have guessed that by the end of it I would have made lifelong friends. My journey could not have been the same without you all. Thank you Camila, Raul, Yanos, Marta, Megan, Sebastian, Maria, Maro, Nicolas and Chau for being there for me all along. A big thank you to Gen, Mari and Chelsey for all the fun time we shared together, superhero discussions, discussions basically on anything and the food adventures we have had. Special thanks to Eirini for everything (I don't have enough lines to elaborate!). I truly enjoyed all the coffees, beers, dinners, cakes , trips, concerts, bouldering, parties etc with all of you.

A big thank you to the Indian gang Darwin, Bhavana, Bhattu, Mayuri, Ram, Varun, Aritra, Sujaya and Nakul for all the Indian dinners, the Bollywood movie nights and so much more. I really did not miss India when I was with you all.

My friends back home and abroad, Shruthi, Apoo, Kavi, Kutty, Naveen, Siji, Ashfaq, Raghu, Rianne, Jerry, Michael, Sohan and Shilpa thank you for your constant support and encouragement even though we are miles away. I am very lucky to have you all in my life.

I would like to thank my dad, mom, my brother Anurag, my father- in-law, mother-in-law, my sis-in-law Manasa, Chachu, Chachi and Uma periamma for believing in me, constantly standing by me through all the trying times and for all their love and support.

To my wife and soulmate Laxmi, thank you for being my strength, for taking my mood swings and for your unconditional love. You have been my constant pillar of support all the time. This journey would not have been possible if you had not pushed me to pursue my dreams all those years ago even if it meant being apart for more than a year and for the personal sacrifices you made on the way. I owe this success to you.

And finally thank you to my son Vihaan whose cries kept me awake during the night and helped me finish the thesis!

List of Publications

Journal Papers

4. **Anand C**, Groves RM, Benedictus R. Modeling and Imaging of Ultrasonic Array Inspection of Side Drilled Holes in Layered Anisotropic Media. *Sensors*. 2021; 21(14):4640. <https://doi.org/10.3390/s21144640>
3. **Anand C**, Groves R, Benedictus R. A Gaussian Beam Based Recursive Stiffness Matrix Model to Simulate Ultrasonic Array Signals from Multi-Layered Media. *Sensors*. 2020; 20(16):4371. <https://doi.org/10.3390/s20164371>
2. **Anand C**, Delrue S, Jeong H, Shroff S, Groves RM, Benedictus R. Simulation of Ultrasonic Beam Propagation From Phased Arrays in Anisotropic Media Using Linearly Phased Multi-Gaussian Beams in *IEEE Transactions on Ultrasonics, Ferroelectrics, and Frequency Control*, vol. 67, no. 1, pp. 106-116, Jan. 2020, doi: 10.1109/TUFFC.2019.2936106.
1. Fortunato, J., **Anand, C.**, Braga, D.F.O. *et al.* Friction stir weld-bonding defect inspection using phased array ultrasonic testing. *Int J Adv Manuf Technol* **93**, 3125–3134 (2017). <https://doi.org/10.1007/s00170-017-0770-7>

Conference Papers

1. **Anand, C.**, Groves, R. M., Shroff, S., & Benedictus, R. (2018). Simulation of ultrasonic array inspection of composites with side drilled holes. In *ECCM 2018 - 18th European Conference on Composite Materials* (ECCM 2018 - 18th European Conference on Composite Materials). Applied Mechanics Laboratory.
2. **Anand, C.**, Shroff, S., Groves, R.M., Benedictus, R. (2017). Modelling of ultrasonic beam propagation from an array through transversely isotropic fibre reinforced composites using Multi Gaussian beams. In *The 9th International Symposium on NDT in Aerospace*, Xiamen

Curriculum Vitae

The author was born on 6th April 1988 in Mumbai, India. He finished his schooling in Bangalore, India and graduated with a degree in Bachelor's of Mechanical Engineering in 2009 from SDMCET, Dharwad. He then went on to pursue a Master's in Aerospace Engineering from Madras Institute of Technology, Anna University in Chennai graduating in 2011. He then worked in Tata Consultancy Services as a Software Engineer from 2011 till 2015. He moved to Delft in 2015 to pursue his PhD at the faculty of Aerospace Engineering under the supervision of Prof. Rinze Benedictus and Dr. Roger Groves.

Since February 2021 he has been working as a Functional Engineer at ASML